NUMERICAL SIMULATIONS OF LOBED MIXER FLOW FIELDS

by

Jan K. Krasnodebski

B.A.Sc. Mechanical Engineering
University of Waterloo, Ontario, Canada, 1993

Submitted to the Department of Mechanical Engineering
in Partial Fulfillment of the Requirements for the
Degree of

MASTER OF SCIENCE IN MECHANICAL ENGINEERING

at the

MASSACHUSETTS INSTITUTE OF TECHNOLOGY

September 1995

© Massachusetts Institute of Technology, 1995. All rights reserved.

Signature of Author _____
Department of Mechanical Engineering
August 11, 1995

Certified by _____
Professor Ian A. Waitz
Professor of Aeronautics and Astronautics
Thesis Supervisor

Accepted by _____
Professor Ain A. Sonin
Professor of Mechanical Engineering
Chairman, Departmental Graduate Committee
Reader

Numerical Simulations of Lobed Mixer Flow Fields

by

Jan K. Krasnodebski

Abstract

The applicability of a three-dimensional, steady, compressible, unstructured-mesh, viscous, Navier-Stokes solver and a two-dimensional, unsteady, slender-body approximation was studied for the investigation of lobed mixer flow fields. The viscous flow solver was evaluated for its ability to calculate the shed streamwise circulation, its subsequent downstream evolution and the thrust. The effects of the type of grid generation, boundary layer grid density, turbulence model and smoothing scheme were examined. Structured-based meshes for lobed mixer geometries had severely skewed elements that resulted in vorticity that was unsupported by physical laws. This was overcome by using fully unstructured grids. Approximately 6 boundary layer elements were required to capture the boundary layer over the lobes for attached flows: if separation occurred, more elements were necessary. Replacing the standard k-ε turbulence model with the turbulent diffusivity of a shear-layer had no impact on the parameters of interest. In general, the viscous Navier-Stokes solver was best suited for examining the flow over the lobes. Downstream of the trailing edge, the circulation could not be evaluated with confidence. However, from a sensitivity analysis, it was found that the scalar mixedness could still be evaluated to within 20%.

Having established the validity of the Navier-Stokes solver, it was used to study the viscous effects in lobed mixers. Lobes with penetration angles from 22° to 45° were examined. As the lobe penetration angle was increased, the trailing edge circulation deviated from a simple one-dimensional model because of increased boundary layer blockage and separation. Extending this model using an effective penetration angle and height gave predictions of the shed streamwise circulation that corresponded to the computed ones to within 5%. There was no benefit, in terms of the trailing streamwise circulation, of increasing the penetration angle above 30° because of increased boundary layer blockage and separation. The losses associated with the lobed mixer increased with the penetration angle and were dominated by mixing losses.

The scalar mixedness, interface length and streamwise vorticity were compared between the three-dimensional solver and slender-body approximation to determine the latter's range of applicability. It was found that the slender-body approximation was valid outside the range given by dimensional analysis of the governing Navier-Stokes equations. Slender-body theory held for flows with non-dimensional shed streamwise circulations of up to ≈ 1 and $\Delta U / \bar{U} \leq 0.3$. The approximation was less valid for a stream-to-stream density ratio of 0.5.

2

Acknowledgments

I foremost wish to thank Professor Ian A. Waitz for the opportunity to work on this project and for providing guidance and advice throughout it.

I also thank Professor E. M. Greitzer for his tremendous insight and Dr. C. Tan for his assistance in understanding the world of CFD.

This work would not be possible if it was not for Bill Dawes' advice and Professor Jaime Peraire and his effort in providing the unstructured grid generator. Thanks as well to Professor Ain Sonin.

My special gratitude to Steve Ellis for keeping the GTL computers running.

Thanks to Holly Rathbun for emergency candy and Robin Courchesne for showing me how not to break the office equipment. A great thank-you to Leslie Regan for directing me through MIT rules & regulations.

I extend a warm thanks to all my friends at Ashdown who have helped make my stay an enjoyable one. Joe Bambenek - a true friend and a man of the highest stature & Nicole; Andrew, for endless hockey discussions; Doug, for not falling off my balcony; Tom; Chris; Sudharshan; Benjie "I dare you to .."; Mario & Rose - true friends;
Christina, for the good times - the "boomerang" - and putting up with me - I will remember you as a very special friend.
A warm thanks also to all the others I do not have room to name.

I also thank Mike T, for his invaluable friendship and Father Campbell, for humoring me.

The thesis gang - Ammar, for his endless generosity and depth; Hong, for the dinners, vase and compassion; Christophe Grosshenry, for the negotiations and Tom London.

Thanks to Assimina, and her 100 emails in the month of July, which allowed me to stay in lab over 16 hours a day when writing my thesis. I miss you already ! (really)

Also thanks to Belva, Ken, Ted, Ish, Emmanuel, Fouzi, John, Harald, Amrit, Greg, Becky, George, Andy, and Stephen for the code help.
To Patia, for the warm and gentle moments. Please take care of yourself.

The highest honor to my office-mates, for putting up with my numerous outbreaks.
John "BBC" Brookfield, a friend for life (sorry, you are stuck with me - but hey, the stories!); Martin "FFury", a great guy and a terrific person (thank-you, Martin, for writing your own acknowledgement), Tom Wong, whose phobia is behind him, for the Lonestar gift. A special thanks to all for the probing and deep discussions, keen observations and for picking up the eraser. It just would not be the same without the Quote of the day/month,df-meter, Macho Man, awesome flukes. And we made it without anyone breaking dishes in the office - at least that we know of.

Thanks to my sister for bringing me goodies from Canada.

Most importantly, I thank my mother, Maria Krasnodebski, whose infinite support and love have no bounds. Some say that among the everyday people are the Saints. She is one of them.
To her I dedicate my thesis.

Contents

List of Figures

List of Tables

Nomenclature

C_D	dissipation coefficient
C_{Pt}	total pressure loss coefficient
$[C_{Pt}]_{bl}$	boundary layer loss coefficient
$[C_{Pt}]_m$	fully mixed loss coefficient
$[C_{Pt}]_s$	swirl mixing loss coefficient
$[C_{Pt}]_T$	total loss coefficient (boundary layer + mixing)
C_T	thrust coefficient
h	lobe half-height
h_{eff}	effective lobe half-height
k	turbulent kinetic energy
L	two-dimensional interfacial length between two fluid streams
$\dot{m}$	mass-flow rate through axial plane
M_{sca}	scalar mixedness, area-averaged
$\overline{M}^m{}_{sca}$	scalar mixedness, mass-averaged
M_{sw}	streamwise Mach number
P	static pressure
$\overline{P}^m$	mass-averaged static pressure
P_T	total pressure
$\overline{P}^m_T$	mass-averaged total pressure
$\vec{q}$	velocity vector, (u, v, w)
r	velocity ratio, U_1/U_2
s	density ratio, ρ_1/ρ_2
t^*	non-dimensional time, $\dfrac{\Gamma}{\overline{U}\lambda} \cdot \dfrac{x}{\lambda}$, downstream of lobe trailing edge

Re_x	Reynolds number, Ux/ν
Re_Γ	Reynolds number, based on circulation, Γ/ν_T
u	streamwise velocity
$\overline{u}^m$	mass-averaged streamwise velocity
U_1	slow stream velocity at inflow plane
U_2	fast stream velocity at inflow plane
v	spanwise velocity
w	transverse velocity
x	streamwise distance
x^*	non-dimensional streamwise distance, x/λ
α	lobe penetration angle
α_{eff}	effective lobe penetration angle
δ_d	boundary layer displacement thickness
δ_{vor}	planar shear layer vorticity thickness
ε	turbulent dissipation rate
ϕ	passive scalar value
Γ_{sw}	streamwise circulation
Γ_{sw}^*	non-dimensional streamwise circulation, $\Gamma_{sw}/(\overline{u}^m\lambda)$
λ	lobe wavelength
ν	laminar kinematic viscosity
ν_T	turbulent kinematic viscosity
ρ	density
θ	momentum thickness

Chapter 1

Introduction

1.1 Background

Lobed mixers are passive devices that are used to augment mixing between co-flowing streams of fluid. They provide relatively low-loss and rapid mixing, thereby making them attractive for a variety of applications. They are employed in jet engines to mix the core and bypass flows in order to increase the thrust [15]. They are also being considered for noise reduction in mixer ejectors on the proposed HSCT (High Speed Civil Transport) [16] and for enhanced mixing of fuel and air in combustors. Although there have been a number of investigations involving lobed mixers, their flow physics is not fully understood and there are a number of issues that must be explored further to increase their effectiveness in various devices.

Figure 1-1 shows an advanced lobed mixer (ADM) [29] typical of current technology. The trailing edge has alternating lobes that increase the interface area between the streams of fluid. As the fluid passes over a lobe it follows the transverse penetration, resulting in alternating transverse velocities at the trailing edge between lobes. This creates a swirling flow downstream of the trailing edge with streamwise circulations on the order of the lobe height. Both the increased trailing edge length and these shed vortices enhance the mixing compared to a flat splitter plate. Manning found that the contribution of these two mechanisms was approximately equal [17]. As the trailing edge length is fixed by the geometry, it is the streamwise vortex behavior which is of primary interest. The vortex stretches the interface between the two fluid streams and therefore augments the mixing rate

through the increased interfacial area and property gradients. Two issues of interest regarding the streamwise vorticity are its creation over the lobes and its subsequent evolution past the trailing edge of the mixer.

Numerical computations are an accessible tool for investigating lobed mixer flow fields. There has been considerable work in this area. Povinelli *et al.* [26] concluded the secondary circulations were primarily inviscid in nature and for Mach numbers less than two, Elliot showed that the secondary circulations were essentially incompressible as well [10]. Koutmos *et al.* have employed Navier-Stokes solvers for studying the flow over the lobes and the mixing region past the trailing edge [12, 13]. O'Sullivan studied the viscous effects in the lobes and various loss mechanisms [20] and Qiu [27] used a two-dimensional unsteady slender-body approximation to the three-dimensional flow to study various effects on the downstream mixing rate. However, these investigations have generally centered on specific fluid dynamic issues and have not clarified the suitability and general difficulties of computationally modeling lobed mixer flow fields.

1.2 Research Objectives

Computational fluid dynamic codes have been used to investigate various aspects of lobed mixer flows. It has been shown that current Navier-Stokes solvers model the flow well over the lobes [5]. Downstream of the trailing edge the suitability of such schemes is less clear. The evolution of the vorticity field, the primary mixing augmentation mechanism of interest, is difficult to simulate accurately in this region [19].

The primary aim of this investigation was to determine the suitability of two different computational fluid dynamic codes for investigating lobed mixer flows. One was NEWT, a fully three-dimensional, unstructured-mesh, compressible, Navier-Stokes solver. The second was a slender-body approximation to the three-dimensional flow. In particular,

15

1) The applicability of NEWT was determined.

2) In addressing the first objective the following aspects of lobed mixer flow fields were examined:

   (i) The uncertainty in the calculation of the evolution of streamwise vorticity downstream of the trailing edge was estimated. In doing so, the effects of various variables, such as the type of grid generation, resolution, numerical smoothing and the turbulence model were examined.

   (ii) The quantitative effect of the boundary layer displacement thickness on the streamwise circulation shed from the lobed mixer was investigated.

   (iii) The contribution of various loss mechanisms to the total loss associated with lobed mixers was examined.

3) The results of the two-dimensional slender-body approximation were compared to the three-dimensional code to determine the former's range of applicability.

4) The most appropriate use of each of the codes for investigating lobed mixer flow fields was determined.

1.3 Research Approach

Two codes were examined. NEWT, a three-dimensional, steady, compressible, viscous Navier-Stokes solver was combined with both structured-based and unstructured grids. The second code examined was a two-dimensional slender-body unsteady approximation that employed a spectral solver. The calculations were for subsonic inlet and outlet flow except for a test case for combined supersonic/subsonic inlet conditions.

To validate and determine the applicability of NEWT to capture shear-layer mixing, a flat plate shear layer was compared to analytical and experimental data. Two smoothing schemes and both a k-ε and a simple shear layer growth turbulence model were tested. Three boundary layer grid densities were examined.

In examining the flow field with NEWT, ADM lobed mixers with penetration angles ranging from 22° to 45° were used. A convoluted plate geometry (Fig. 1-2) with α=22° was also tested. Two inlet boundary layer displacement thicknesses and velocity ratios between 0.5 and 1.0 were examined.

The comparisons of the two-dimensional slender-body approximation with the three-dimensional code were performed for a lobed mixer with a height to wavelength ratio (h/λ) of 1. Three velocity ratios, ranging from 0.6 to 1.0, and density ratios of 0.5 and 1.0 were examined. The initial conditions for the slender-body code were interpolated from the trailing edge of the full three-dimensional solution. The streamwise circulation decay rates were matched between the two codes by varying the turbulent viscosity in the two-dimensional spectral solver.

1.4 Thesis Overview

The thesis is organized as follows. Chapter 2 describes the three-dimensional solver, the grid generators for it and post-processing of the solutions. Chapter 3 investigates the applicability of using NEWT for lobed mixer flows and Chapter 4 presents the results of the three-dimensional investigations. The slender-body approximation is presented in Chapter 5 and compared to the three-dimensional solver. Chapter 6 presents the recommendations and conclusions.
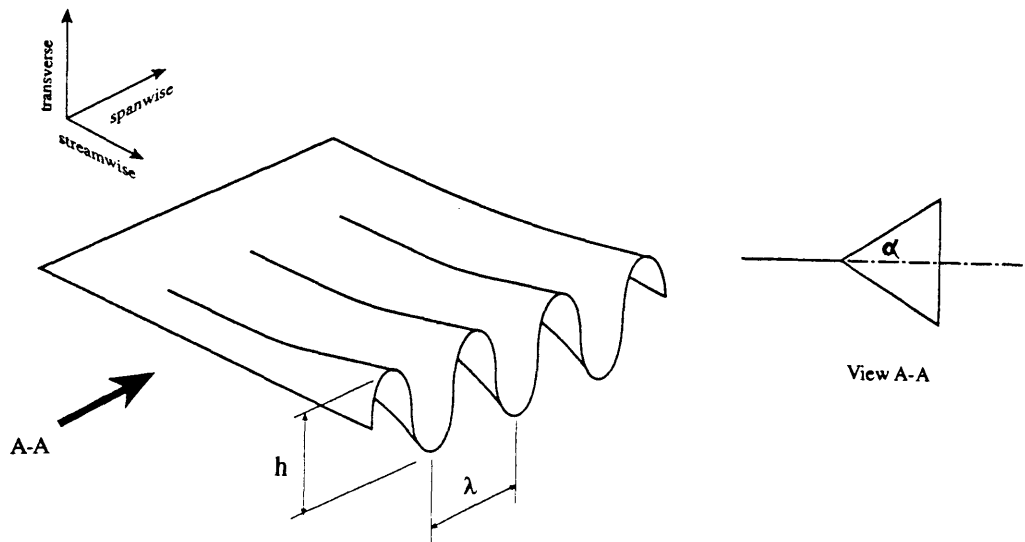
Figure 1-1   Lobed mixer geometry   [20]

convoluted extension
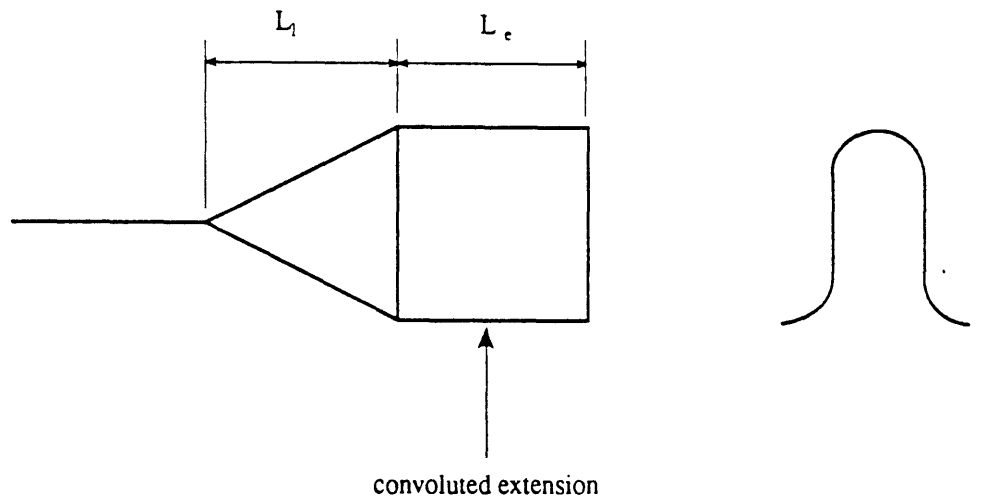
Figure 1-2   Convoluted plate (CP) geometry   [20]

Chapter 2

NEWT:
The Three Dimensional Navier-Stokes Solver

NEWT is a three-dimensional, steady, viscous, compressible, unstructured-mesh, Navier-Stokes solver with turbulence modeled using the k-ε transport equations. It has been used extensively for turbomachinery and internal flows [4, 5]. The advantages of employing NEWT include solving the full Reynolds-averaged Navier-Stokes equations. However, extensive computer resources are required to run this code.

Modeling a full lobed mixer flow involves two regimes. The flow over the lobe is bounded by the lobe walls, but past the trailing edge the flow is only constrained by the duct in the far field. These two regions have conflicting requirements with respect to the grid and solver.

Obtaining a solution involved the following three steps: (i) generating a grid (ii) solving the Navier-Stokes equations (iii) post-processing the results. The chapter's structure follows these topics.

2.1 Grid Generation

The first step in performing a Navier-Stokes calculation is to create a grid that both represents the geometry of the mixer and the important features of the flow field. A half wavelength with symmetry conditions was used to model an array of lobed mixers. Lobed

mixers are a particularly difficult geometry to generate a grid for because of the rapid transition from a flat plate to the vertical wall of the mixer. Near the wall of the lobe a dense grid is required to capture the high Reynolds number boundary layer. For typical lobed mixer flows, the axial gradients are smaller than those in the cross-flow plane, so highly stretched elements are used to minimize computational resource requirements. However, downstream of the trailing edge the closely packed boundary layer elements result in numerical and discretization errors. In this region the grid refinement should follow the swirling flow, which is not known *a priori*. As such, to improve the grid accordingly, a solution-adaptive mesh refinement scheme should be implemented.

Two grid generation procedures were employed. The first was based on a structured grid which was partitioned into unstructured tetrahedra and then refined. The second was a completely unstructured mesh.

2.1.1 Structured-Based Grid Generation

Structured grid generation is relatively quick and simple. The grid generator created a structured grid and then unstructured it when creating tetrahedra. As such, the grids were unstructured in the end, but maintained their structured nature. Despite the aforementioned advantages, the method was not satisfactory for the geometries considered. As shown in Fig. 2-1, this procedure resulted in severe mesh skew of the boundary layer elements and those in opposite corners of the grid. This was a result of the rapid transition from a flat plate to the vertical wall of the lobe combined with the restrictions of a structured grid. This skew lead to fictitious cross-stream velocities.

2.1.2 Fully Unstructured Grid Generation

To overcome the problems associated with the lobe geometry and structured-based grids, a fully unstructured procedure was used. Currently, there is no available unstructured three-

20

dimensional viscous grid generator that is capable of automatically generating a grid for an arbitrary geometry [25]. In order to obtain the required range of element size and aspect ratio, two separate grids were created and then matched at their boundary. The first grid was created for the inviscid region of the flow, where relatively large isotropic elements were most appropriate. The second grid was generated for the boundary layer region in which the elements were required to have high aspect ratios and very close packing near the wall. In each region the element aspect ratio and size could vary by approximately a factor of four. As such, the boundary layer elements could be over an order of magnitude smaller than those in the freestream. This allowed the viscous effects to be captured while minimizing the required computational resources.

The procedure that was employed was based on Peraire's advancing front technique, which allowed the creation of elements with variable size and aspect ratio [24]. It involved generating the points and elements simultaneously and differs from most schemes in this manner. The boundary curves were subdivided according to user-input specifications for size and stretching. Nodes were then placed interior to the boundaries and joined to form lines that were then the sides of triangles. The interior lines formed a front which contained all the sides that were available to form new triangles. Each side was chosen in turn and a new triangle was formed by either adding a new node or connecting to an existing one. The front advanced until the surface was covered with a triangular mesh. Figure 2-2 shows this procedure for a circular region. Figs. 2-3 and 2-4 show the final triangular meshes produced by this method over a lobe and convoluted plate. Once all the surfaces were meshed, the process was extended into three dimensions to form the tetrahedral grid. Triangles formed the front, to which nodes were added to form tetrahedra until the front area became zero.

The unstructured grids had two primary deficiencies. First, the aspect ratio changed by approximately an order of magnitude at the boundary between the elements in the inviscid and boundary layer regions. This resulted in numerical rounding errors. For NEWT the aspect ratio of adjacent elements should not vary by more than a factor of 1.5 [7] because of the numerical methods used in the code (discussed in Section 2.2). Also, the gridding for the region downstream of the trailing edge was poor. In this region, the tight boundary layer region from over the lobes was linearly expanded to the outflow (Fig. 2-5). The refinement in the grid did not follow the swirling motion of the fluid. The boundary layer from over the lobes should also expand faster than the current grids. In general, the downstream elements that originated from the boundary layer had large aspect ratios and were of marginal quality as a result.

Although it is possible to refine the grids adaptively according to the solution, the refinement procedure integrated into NEWT was not compatible with the fully-unstructured grids. Due to time constraints it was not modified appropriately. However, adaptive refinement would be very useful for capturing the swirling flow past the trailing edge.

The results of grid studies are presented in Section 3.2. The streamwise vorticity at the trailing edge and the downstream evolution were compared for the two types of grids and three different densities.

2.2 Flow Solver

NEWT is a three-dimensional, steady, compressible, viscous, Navier-Stokes solver. The full three-dimensional Reynolds-averaged Navier-Stokes equations were solved with the seven equations being discretized in finite volume form over the grid tetrahedra. The variables were piece-wise linear, so their derivatives (for the stress terms) were constant over the cell faces and the fluxes were evaluated to second order. Gauss' divergence

theorem was used to calculate the derivatives, in order to integrate the terms instead of numerically differentiating them. This minimized the numerical error. A fourth order Runge-Kutta time marching routine was used to balance the fluxes across the cells, so the code was not time accurate.

The k-ε transport equations were used to model turbulence and the constants were given the standard values for attached boundary-layer flows. This was appropriate for the high turbulent Reynolds number flows outside of the log-law layer. To model sublayer damping and molecular diffusion, which were important near walls, low Reynolds number damping terms were employed. The laminar sublayer and log law were used to calculate the shear stress near viscous surfaces. This is a typical implementation of the turbulent energy equations and has been used successfully to model turbulence in a variety of flows [35].

Two smoothing schemes based on the second and fourth derivatives of the flow variables were included in the solver. They differed in the manner in which the derivatives were evaluated. One, a true Laplacian scheme, used Laplace's equation to solve for the derivatives. The other used values at the midpoint of the cell edges. Smoothing was applied to all the variables before solving for the Navier-Stokes terms. Both second and fourth derivative terms were used for smoothing, with the latter being utilized to capture shocks. The smoothing was scaled in accordance with the non-uniform unstructured mesh (*i.e.* over the cell volumes). The second derivative term was also scaled by the local pressure gradient, and the derivatives were evaluated to second-order accuracy. As such, for flows with shocks and high pressure gradients, the solver was particularly sensitive to poor grids. This is noted in Section 3.3, where it was found that NEWT performed poorly when mixed supersonic and subsonic inflow conditions were applied with the lobed mixer geometry, but not the flat plate.

Boundary conditions were applied for the inflow, outflow and at solid surfaces. At the inflow the total pressure and total temperature were specified. For subsonic inlets, the gradient of the static pressure was set to zero at the inlet and the back (outlet static) pressure was fixed. The actual inlet static pressure and velocity were iterated upon by the solver. For supersonic inlets, the inlet pressure was fixed and the back pressure was iterated upon. The values of the variables for nodes on the inflow and outflow planes were linearly extrapolated from the interior nodes of the surface elements. At solid surfaces the normal components of the mass, momentum and energy flux were set to zero. For viscous surfaces, the log-law or laminar sublayer equations, as appropriate, were used to calculate the shear stress.

In order to visualize and quantify the mixing, a passive scalar was added to the solver. One inlet stream was assigned a scalar value ϕ of +1 while the other was set to -1. The passive scalar was computed using a diffusion equation with convection, which is of the same form as the momentum equation. The Schmidt number was taken to be 0.5, which is representative of turbulent planar shear layers [28].

A measure of the amount of mixing is the scalar mixedness. The area-averaged scalar mixedness was defined as,

$$M_{sca} = \frac{1}{A} \int_{flowarea} (1 - |\phi|) dA. \tag{2-1}$$

which varied from 0 to 1. The mass-averaged value was defined as,

$$\overline{M}^m{}_{sca} = \frac{1}{\dot{m}} \int_{flowarea} (1 - |\phi|) d\dot{m}. \tag{2-2}$$

and has been normalized to give a fully-mixed value of one.

The zero contour of the passive scalar was taken to be the interface between the two streams of fluid[†].

2.3 Post-Processing

The variables which the solver calculated included the following: the three velocity components, density, static pressure, turbulent kinetic energy, turbulent dissipation rate and the passive scalar. Other quantities had to be post-processed from this data. However, with a fully unstructured grid and modeling only half a wavelength (thus potentially allowing for boundary condition influence) it was not always straightforward to obtain the required quantities.

The first type of post-processing involved node-based values, such as the total pressure, temperature and entropy. These were straightforward to evaluate, as they were calculated using a thermodynamic (isentropic) relation. The second type involved an axial flow plane onto which the node values had to be interpolated. Calculations that involved axial-based quantities (such as mass-averaging) were evaluated relatively easily and accurately. However, cross-plane calculations were not always possible. The length of the interface between the two mixing streams could not be calculated automatically and had to be measured from passive scalar plots. The difficulty lay in that the unstructured grid was not regular and had highly stretched elements; subsequently, the zero scalar contour followed the irregularities in the grid. The circulation about a path could be calculated well as the path was specified and did not depend on the grid. However, the vorticity diffused out of the computational domain in the downstream region, potentially making the calculation less accurate. The boundaries were specified as inviscid walls and thus had conditions imposed on them so the flow variables were not all calculated. Therefore, the exact nature of the

---

† This is the exact interface area per unit length in the streamwise direction in the limit of $\Gamma \to 0$.

interaction of adjacent vortices may not have been captured accurately. As such, further downstream of the trailing edge, the streamwise circulation calculation became less reliable, as discussed in Section 3.2. A comparison with a calculation using a full wavelength would ascertain the accuracy of the current computations. This, however, was not completed because of time constraints.

2.4 Summary

The Navier-Stokes solver NEWT required the following three steps to produce a solution: generating a grid, solving the Navier-Stokes equations and post-processing the results.

Both a structured-based and fully unstructured grid generator were employed. The structured-based grids suffered from very large dihedral angles in the boundary layer elements. This lead to numerical errors in the cross-flow velocities. The fully unstructured grids were generated using the advancing front technique. It allowed an order of magnitude variation in the size and stretching of the elements by matching two separate grids for the boundary layer and inviscid regions. The grids were significantly improved over the structured-based ones, but had two main deficiencies: the transition in element size between the boundary layer and inviscid regions was approximately ten times the recommended value; the boundary layer elements from over the lobes were poorly suited for the downstream flow.

The solver used the standard implementation of the k-ε equations to model turbulence. Two smoothing schemes were available in NEWT: they differed in the method they evaluated the required derivatives. Both schemes were grid-sensitive.

Post-processing was easily accomplished on the nodal level. However, calculating cross-flow variables over axial planes was more difficult. It could not be done for the interface

26

length. However, the circulation about a path was calculated accurately as long as the computational boundaries were excluded.
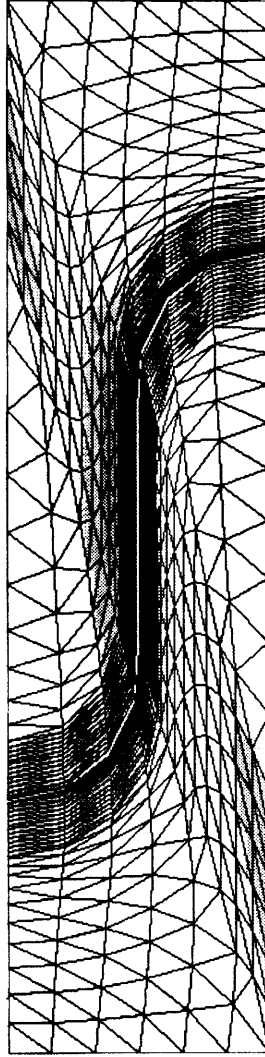
Figure 2-1   **Axial-flow plane of structured-based grid**
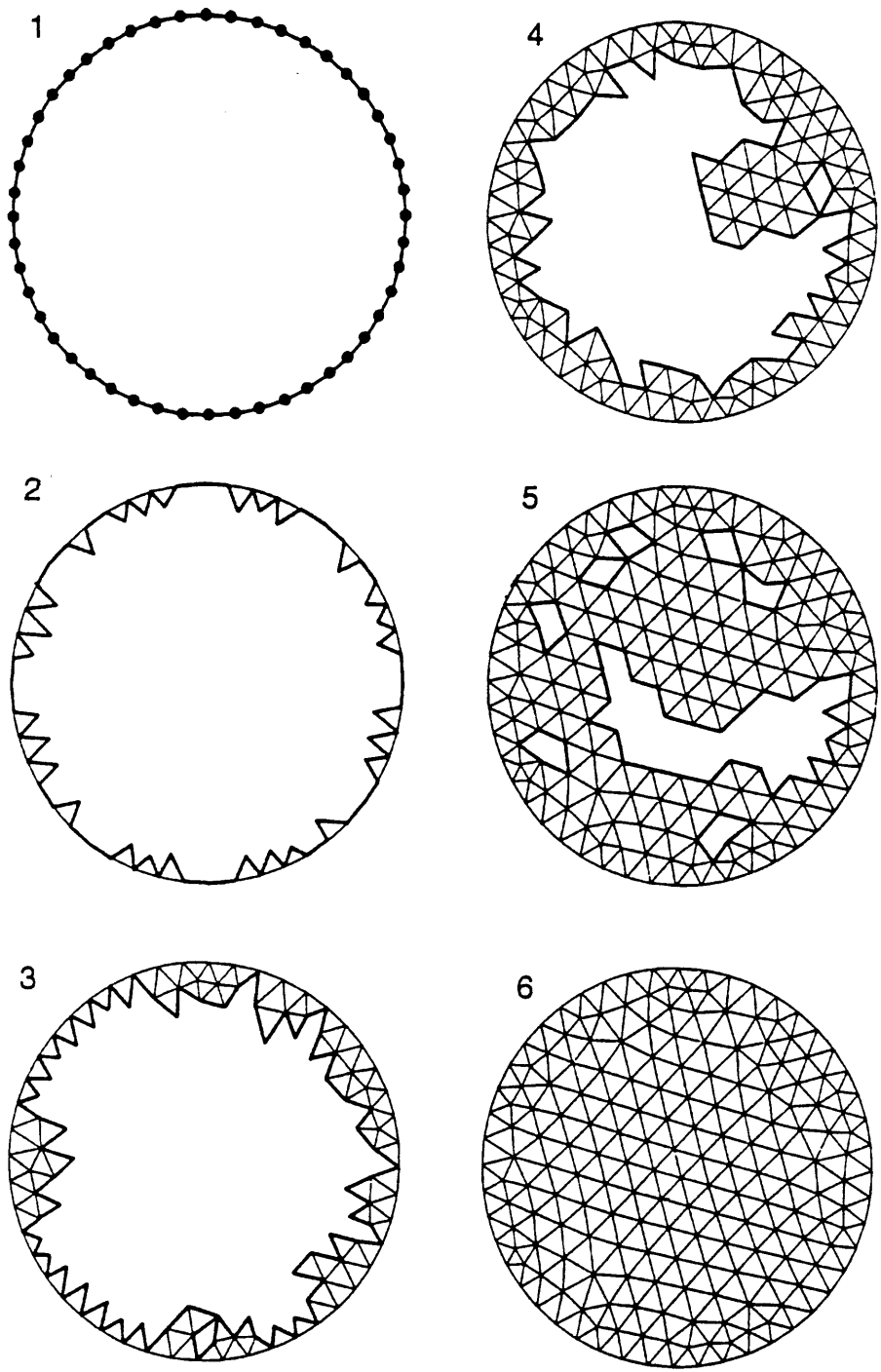
Figure 2-2   **Advancing front technique of mesh generation**   **[24]**
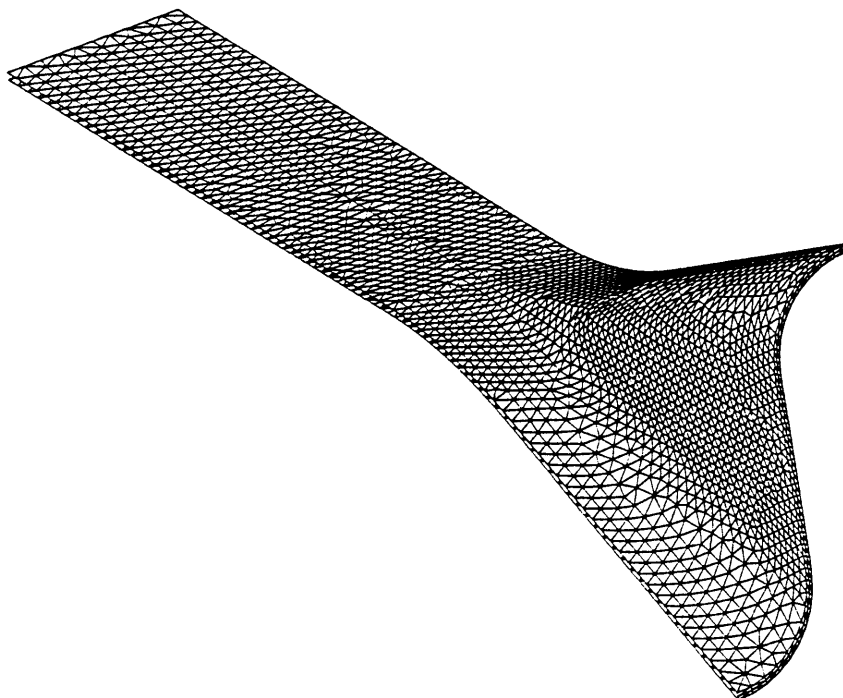
Figure 2-3   Triangular mesh for a lobed mixer
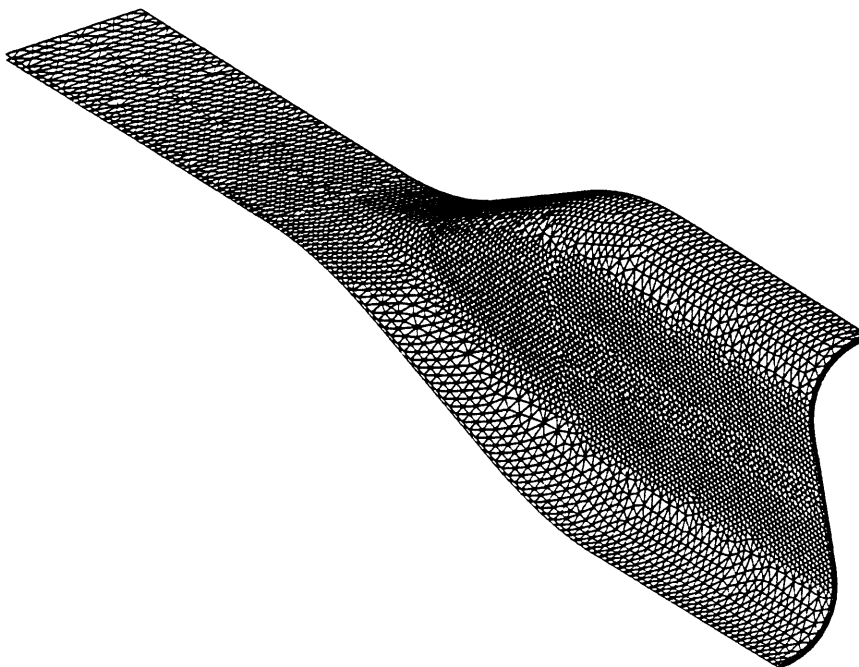
Figure 2-4   Triangular mesh for a convoluted plate
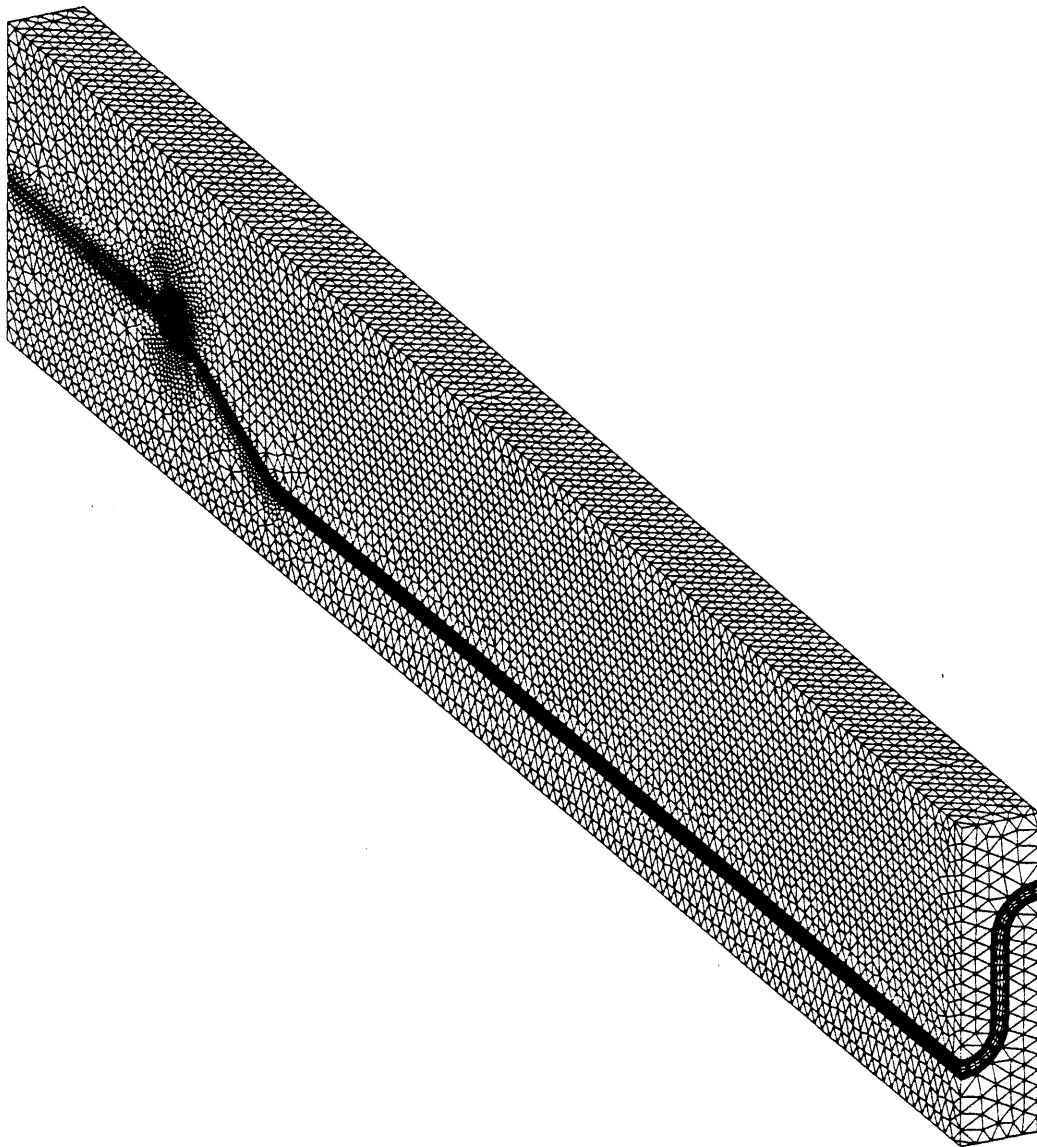
Figure 2-5   Fully unstructured lobed mixer flow domain

Chapter 3

Validation and Limits of NEWT for Lobed Mixer Calculations

In the previous chapter, NEWT and the considerations in obtaining a solution were described. A number of shortcomings and deficiencies were highlighted in the grids, solver and post-processing. These were addressed and investigated to assess the ability of NEWT to model lobed mixer flows. This chapter quantifies the accuracy of the solver's results. The code was first tested for planar shear layer flows and then assessed for various issues pertaining to lobed mixer calculations.

3.1 Flat Plate Shear Layer Comparison

NEWT has been extensively tested and validated for internal flows, particularly those in turbomachinery [4, 5]. The flow over the lobes can be considered to be of this type, but downstream of the trailing edge it is dominated by shear layers. As such, the code was tested for a free shear layer flow. A flat plate was employed because there is considerable experimental and analytical data for comparison. The flat plate is also a severe test for capturing the mixing in a lobed mixer flow field as mixing past a flat plate is solely due to turbulent diffusion. In comparison, lobed mixers have strong secondary flows of an inviscid nature which are responsible for a significant portion of the mixing [17]. As such, deficiencies in modeling the shear layer may be mitigated in lobed mixer flows.

A structured-based grid with initially 5 elements across the expected boundary layer region was employed. The grid was adaptively enriched based on the cellwise variation in the

Mach number from 100,000 cells to over 300,000. (Since the geometry involved was a flat plate, structured grid generation was appropriate). The flow on either side of the viscous plate was at Mach 0.5 and 0.3, giving a velocity ratio of 0.6. The static temperatures and pressures were equal for the two streams at 300 K and 100 kPa.

The velocity profiles and shear layer growth rate from the numerical solution were compared to experimental data. Through these comparisons it was concluded that NEWT is capable of accurately capturing the physics of shear layers.

3.1.1 Velocity Profiles

The similarity solution to the Reynolds' time-averaged turbulent equation, using Prandtl's second hypothesis, gives an error-function velocity profile for the shear layer. These profiles match experimental data closely [35]. The velocity profiles from NEWT were compared to experimental data of Spencer and Jones [30]. As seen in Fig. 3-1, there was a small degree of undershoot in the computational profile taken at approximately 1000 momentum thicknesses downstream of the trailing edge. This was from the plate's wake, which persisted longer than is experimentally observed [1]. This was probably the result of insufficient grid density; however, because of the high aspect ratio of the elements ($\approx$15), refining the grid further was inadvisable. The small velocity defect was the only significant difference in the profiles and was less than 5% of the average velocity. Otherwise, the two profiles agreed. The computed flow was also two-dimensional, and had the observable characteristics of a planar shear layer.

3.1.2 Shear Layer Growth Rate

The thickness of an incompressible turbulent planar shear layer grows linearly with the axial distance [35]. The solution to the Reynolds' time-averaged turbulent equation, using Prandtl's second hypothesis, also gives,

33

$$\delta(x) = b\frac{(1-r)}{1+r}x, \tag{3-1}$$

where b is an empirical constant in the range of approximately 0.1-0.2 (see below). Again, this analytical solution matched the experimentally-observed behavior. The growth rate, $d\delta/dx$, was then $b(1-r)/(1+r)$. Defining the shear layer thickness as the difference in the freestream velocities divided by the maximum velocity gradient, $i.e.$,

$$\delta(x) = \frac{U_2 - U_1}{\left(\frac{dU}{dy}\right)_{max}}, \tag{3-2}$$

the empirical constant was then given by,

$$b = \frac{d\delta}{dx}\bigg/\left(\frac{1-r}{1+r}\right). \tag{3-3}$$

Dimotakis gave a range for b of 0.125 - 0.225 for different flow conditions [8]. For a stream-to-stream velocity ratio of 0.57, McCormick measured b as 0.132 [18]. The value from the computed shear layer was 0.12. As such, the code captured the growth rate with sufficient accuracy.

3.2 Lobed Mixer Flow Comparisons

The flat plate comparison established that NEWT was capable of capturing the physics of a shear layer flow. However, there are additional issues in modeling lobed mixers: they have a complex geometry and shed streamwise circulation that evolves downstream of the mixer. This section examines the issues and difficulties associated with the numerical simulation of these features.

Generating a grid was the most difficult and problematic step in performing the viscous Navier-Stokes calculation. NEWT was grid sensitive because it evaluated derivatives only

to the second order and the smoothing was scaled by the cell volumes. The developer of the code recommended that adjacent elements vary no more than 50% in size [7]; however, the grids had variations on the order of 500%. Also, the boundary layer required highly stretched elements that lead to numerical errors in the cross-stream velocities downstream of the trailing edge. Due to the inexact nature of turbulence modeling, the sensitivity of the solution to the turbulence model was examined. Additionally, the turbulence model in NEWT was replaced with the simple planar shear layer model used in the slender-body code for the three-dimensional comparisons. The effect of this change was examined.

The computational matrix for the comparisons is given in Table 3-1. The first two entries were convoluted plates and the remainder were ADMs. Unless otherwise stated, the k-ε turbulent model and approximately 6 elements across the boundary layer region of the grid were employed in the calculations.

The baseline case for comparisons was the ADM with α=22° and a velocity ratio of 0.6. The characteristics of the flow associated with this geometry were representative of the general features of lobed mixer flows.

Before performing quantitative comparisons, the ability of the code to capture experimentally observed qualitative features of lobed mixer flows [17, 18, 27] was assessed. The role of streamwise circulation in augmenting the bulk mixing rate of the streams is seen in Figs. 3-2 and 3-3. These figures show the streamwise Mach number field (denoted M_{sw}) at four downstream axial stations, x*= 0, 1, 3 and 6. Fig. 3-2 corresponds to CP2 and Fig. 3-3 to an ADM (case A2), both with a penetration angle of 22°. For the convoluted plate there was little increase in the length of the interface between the streams, and the streams remained largely unmixed. For the ADM, by x*=1 the

35

Table 3-1
Computational matrix for the validation of NEWT for lobed mixer flows

CASE	Penetration Angle (α)	Velocity Ratio (r)	Grid Type	Smoother	Other
CP1	(22°)	0.53	structured	edge-based	
CP2	(22°)	0.46	unstructured	edge-based	
A1	22°	0.60	structured	edge-based	
A2	22°	0.51	unstructured	edge-based	
A3	22°	1.0	structured	edge-based	
A4	22°	1.0	unstructured	edge-based	
A5	22°	0.61	unstructured	Laplacian	
A6	22°	0.51	unstructured	Laplacian	2 bl elements
A7	22°	0.42	unstructured	Laplacian	11 bl elements
A8	22°	0.62	unstructured	Laplacian	shear-layer turbulence model
B1	30°	0.61	structured	edge-based	
B2	30°	0.52	unstructured	edge-based	7 bl elements
B3	30°	0.48	unstructured	edge-based	11 bl elements
C1	35°	0.60	structured	edge-based	
C2	35°	0.50	unstructured	edge-based	
D1	45°	0.62	structured	edge-based	
D2	45°	0.62	unstructured	edge-based	

36

interface had evolved into the characteristic "mushroom" configuration observed experimentally by Manning [17] and McCormick [18]. Comparing Fig. 3-2 to Fig. 3-3 shows the winding-up of the interface by the streamwise circulation. This increased the interface area and the magnitude of gradients across it, both of which augmented the mixing rate. From these plots, it is seen that NEWT captured the general features of lobed mixer flows, including the cross-flow convective transport.

3.2.1 Metrics for Comparisons

The primary purpose of lobed mixers is to provide rapid low-loss mixing. Their performance is quantified by the augmented mixing rates from the streamwise circulation and the cost in terms of the fluid dynamic losses. As such, the metrics for the comparisons were chosen as the shed streamwise circulation and its downstream decay to quantify the mixing augmentation, and the thrust coefficient for the losses.

(i) *The shed trailing edge streamwise circulation*

The streamwise circulation, normalized by the mass-averaged velocity and lobe wavelength, is given by,

$$\Gamma_{sw}^{*} \equiv \frac{1}{\bar{u}^{m}\lambda}\oint_{C}\bar{q}\cdot dl, \tag{3-4}$$

where the contour path was about the computational domain just excluding the boundaries (Fig. 3-4) and $\bar{q}$ was the velocity vector.

The amount of circulation which the lobed mixer introduces quantifies the mixer's performance in terms of the mixing augmentation; however, it does not describe the amount of mixing or its rate. It will be shown in Section 4.2.1 that the computed shed circulation is a function only of the lobe geometry and the boundary layer

displacement thickness in the lobe. Therefore, for a fixed geometry the shed
circulation was only a function of the boundary layer thickness.

(ii) *The streamwise circulation decay*

A metric is required for the downstream mixing augmentation. Both the area-
averaged scalar mixedness and interface length are such measures. However, the
former was not available for all the runs[†] and the interface length became difficult to
evaluate beyond approximately 3 wavelengths past the trailing edge because of
insufficient resolution. Therefore, another metric was required for the downstream
mixing augmentation.

Since the effects of the streamwise circulation were responsible for augmenting the
mixing, the mixing rate for a fixed velocity ratio should be related to the decay rate of
the circulation. In the slender-body comparisons of Chapter 5, it will be shown that
for the same initial conditions, matching the streamwise circulation decay in the
downstream region also matched the area-averaged scalar mixednesses and interface
lengths. As such, given the same geometry and inlet conditions, differences in the
circulation decay rate were representative of differences in the mixing rate. To verify
this relationship, the sensitivity of the area-averaged scalar mixedness and the
interface length to the circulation decay were examined.

(iii) *Thrust coefficient*

The cost of employing a lobed mixer in terms of total pressure losses was quantified
with a thrust coefficient, which indicated the fraction of the fluid's initial momentum
that was lost in the mixing process. This coefficient was defined as,

---

[†] The simulation for the structured-based grids and the edge-based smoothing were performed using a solver that
did not have the passive scalar. These runs were not repeated with one that included a passive scalar because of
time constraints.

$$C_T = \frac{F_{mix}}{F_{inflow}}, \tag{3-5}$$

where F_{inflow} and F_{mix} were defined as follows:

$$F_{inflow} = \int_{flow\ area} (\rho u^2)_{inflow} dA, \tag{3-6}$$

$$F_{mix} = \int_{flow\ area} [(P + \rho u^2)_{te} - P_{inflow}] dA, \tag{3-7}$$

where the subscript, te, denoted the lobe trailing edge plane.

A value of unity indicated loss-free mixing, with lower values indicating higher losses. The coefficient is also of interest in designing nozzles and mixer-ejectors [33]. As such, the sensitivity of this parameter to the grid, smoothing scheme and turbulence model was examined.

3.2.2 Sensitivity of the Scalar Mixedness and Interface Length to the Streamwise Circulation Decay/Turbulent Diffusivity

Turbulent diffusion is responsible for the decay of the streamwise circulation in the downstream region. Adjacent vortices of opposite sign are shed from the trailing edge of the mixer; as they convect downstream, they diffuse and cancel one another. Therefore, to assess the relationship between the circulation decay rate and the mixing parameters, the effect of the turbulent diffusivity was examined with the slender-body code. This code was chosen over the three-dimensional code because it required fewer computational resources and provided better resolution and control of the decay. The case for the investigation had a velocity and density ratio of 1, with a non-dimensional streamwise circulation, Γ^*, of 0.94 (i.e., case S1 in Section 5.3). For these flow conditions, the planar shear layer turbulence model (Eq. 3-11) reduced to a constant diffusivity, which was specified by a

Reynolds number based on the trailing edge streamwise circulation ($Re_\Gamma = \Gamma/\nu_T$). In this manner, the turbulent diffusivity was specified and did not vary in the downstream region. Six Reynolds numbers, Re_Γ=100, 200, 400, 600, 800 and 1000, were investigated, corresponding to the rates of circulation decay in Fig. 3-5. The rate of decay increased with decreasing Reynolds numbers.

The interface lengths are shown in Fig. 3-6. The first cusp corresponds to the point where adjacent mushroom structures joined (*i.e.*, diffused beyond the symmetry boundaries) thereby decreasing the interface length (Fig. 3-7). The second cusp occurred when the tip of the "mushroom" joined with the base (Fig. 3-8). The following drop in the interface length was a result of the flow mixing out locally and becoming essentially a planar shear layer (Fig. 3-9). For the very diffuse case of Re_Γ=100, the characteristic mushroom configuration did not form.

The area-averaged scalar mixedness is compared in Fig. 3-10 for the six turbulent diffusivities/rates of circulation decay. As the Reynolds number was decreased from Re_Γ=1000 to 200, the mixing increased because of increased turbulent diffusion. For the very diffuse case, Re_Γ=100, the mixing rate was initially the fastest, but leveled off when the circulation dropped to 5% of its initial value.

In general, the change in the initial mixing rate, $\Delta(dM_{sca}/dt^*)$, was half of the change in the initial circulation decay, $\Delta(d\Gamma^*/dt^*)$. The change in the growth of the interfacial length, $\Delta(dL/dt^*)$, was within $\approx$20% of the change in the initial circulation decay, $\Delta(d\Gamma^*/dt^*)$. Downstream, the change in their respective magnitudes were comparable although the interface length did not exhibit the same behavior as the circulation. In contrast, for each case the area-averaged scalar mixedness was within 20% for t*>6, even though the circulation differed by approximately an order of magnitude. As such, the

downstream area-averaged mixednesses could be estimated reasonably well even if the circulation decay was not captured accurately.

3.2.3 Effect of Grid Generation Method

Grids for the lobed mixer were created using two different generation methods. Simulations using both types of grids were examined and compared for the parameters of interest. The first and simplest mesh was a structured-based grid. In the axial direction, the only difficulty was the general problem of unstructuring a rectangular block with tetrahedra (discussed below). More problematic was the fact that the cross-flow planes exhibited spurious vorticity, which was defined as vorticity whose existence was not supported by Kelvin's theorem. At the trailing edge of the lobe, only vorticity in the boundary layer is supported by physical laws. Since the computational boundaries were specified inviscid, any vorticity diffusing from them was from numerical error. Three types of spurious vorticity were observed in all the structured-based grids, as defined by their location:

(i) Corner

Fig. 3-11 exhibits vorticity in opposite corners of the grid near the inviscid wall boundaries for case A1. It was a result of the band of skewed elements across the diagonal, shown in Fig. 3-12 and persisted wherever the grid was similarly skewed. The circulation from this vorticity was approximately 5-10% of the total shed streamwise circulation. Since it was close to the symmetry boundaries, though, it did not affect the flow field significantly.

(ii) Background Vorticity

This vorticity was due to the general shape of the elements, which were asymmetric because of their structured origins (discussed below). Although not

41

visible on the plots because of the scale and its magnitude, there was continuous background vorticity of both positive and negative sign. The associated circulation was up to 10% of the total shed circulation. It did not affect the flow field appreciably because of its low-level distributed nature.

(iii) Downstream Wall Growths

Fig. 3-13 shows the vorticity distribution for a cross-flow plane at 5.5 wavelengths downstream of the trailing edge for case A1. There were regions of significant vorticity at the upper and lower wall boundaries which were comparable to the vortex core. Their magnitude is shown in the plot of the downstream circulation evolution (Fig. 3-14), where this spurious vorticity accounted for approximately 30% of the total circulation from 9 wavelengths past the trailing edge. However, it occurred where most of the mixing had taken place and was located in the locally mixed-out areas near the walls. This spurious vorticity would affect the mixing more significantly if it occurred at an interface.

The fundamental problem with the structured-based grids was the large dihedral angles (skewness) of the elements. This lead to an ill-conditioned matrix for the equations being solved by NEWT. This propagated numerical errors in the cross-stream velocities and therefore resulted in spurious vorticity. Another general problem was the asymmetry of the mesh from the alignment of the elements, which was a result of unstructuring a rectangular grid with tetrahedra. Fig. 3-15 shows a typical control volume, in the cross-flow view, that was employed to calculate the flow at a given node. It was stretched along one of its axes, which lead to cross-flow numerical errors.

All of the aforementioned sources of spurious vorticity did not in themselves seriously put into question the validity of the code. Their magnitudes were potentially significant, but they were isolated. However, a more serious possible source of error was from the boundary layer. Unlike the other regions, streamwise vorticity was expected here, so the spurious vorticity from the highly skewed mesh could not be isolated and quantified. In addition, because of its placement at the interface between the streams, this vorticity directly affected the mixing. Therefore, the circulation could not be evaluated with confidence from the structured-based grids.

The fully unstructured grid (Fig. 3-16; case A2) did not exhibit the three types of spurious vorticity found in the structured based meshes. Also, the vorticity at the trailing edge was almost entirely confined to the boundary layer. However, Fig. 3-17 shows that in the downstream region the stretched boundary layer elements had spurious vorticity associated with them, as seen by the imprint of the grid on the vorticity distribution. As such, it was expected that the streamwise circulation could be evaluated with confidence at the trailing edge, but not in the downstream region.

To obtain an estimate of the accuracy of predicting the circulation at the trailing edge and its downstream decay, the results from the two grids were compared to each other and to one experimental case by McCormick [18]. Figs. 3-18 to 3-22 compare the two circulation histories for lobed mixers with $\alpha = 22°$, $30°$, $35°$ and $45°$, with velocity ratios of 0.5, 0.6, 1.0 (cases A1-A2; A3-A4; B1-B2; C1-C2; D1-D2). Fig. 3-23 is for a convoluted plate geometry (cases CP1-CP2). The path for evaluating the circulation (which included the top and bottom computational bounds and 90% of the domain's width) excluded the visible spurious corner vorticity in the structured-based grids. Over the lobes the circulation matched exactly for the first half of the lobe, with differences only occurring towards the

43

trailing edge. The variation in the shed circulations increased with the penetration angle. For α=22°, the shed circulations were within 3%; for 30°, they differed by 10%, for 35°, 24% and for 45°, 40% . This increasing disagreement was concurrent with increasing viscous effects in the lobes. The boundary layer in the lobe was thin ($\approx$1% of the lobe height) for α=22° and increased with the penetration angle, with separation first occurring at 35° and being extensive at 45° (see Section 4.2.1). It was thus evident that a proper grid was required to capture the boundary layer, and thus the shed circulation.

The streamwise circulation evolutions differed significantly in the downstream regions. For α=22° and 45° (cases A1-A2; D1-D2), for which the far downstream development was calculated, the circulation for the two grids differed by approximately a factor of two. Past the trailing edge, the streamwise circulation could only increase from the transverse vorticity associated with the velocity difference of the two streams being tipped into the streamwise direction. This occurs only once just past the trailing edge. As such, the increases in the circulation 4 wavelengths downstream of the trailing edge (Fig. 3-19) were from numerical error, which was substantial ($\approx$20% or more of the total circulation). Also, for the structured-based case of r=1.0, α=22° (case A3), the increase in the downstream circulation was erroneous as there was no net transverse vorticity. For the convoluted plate runs (Fig. 3-23), little or no shed streamwise vorticity was expected. The value of the circulation at the trailing edge persisted for both grids at the same level in the downstream region with negligible decay. This suggested that this circulation was spurious and associated with the grid. In general, the structured-based grids exhibited more spurious vorticity.

Fig. 3-24 compares McCormick's experimentally-measured circulation decay rate to the computed ones. Note that the experimental measurements were not started until approximately three wavelengths downstream of the trailing edge and the flow conditions

44

were not exactly matched (McCormick, r=0.57, h/λ=1.5; computational, r=0.6, h/λ=1).

At the first data point, the experimental and computed circulation were within 10% of each

other. However, the subsequent decay rate for the experimental data was twice that of the

computations. It is evident that the three-dimensional Navier-Stokes solver was grid-

sensitive with respect to the downstream circulation evolution. While the values up to the

trailing edge and immediately downstream could be determined with confidence, far

downstream they could not. It is critical to have an optimal grid if the vorticity is to be

predicted accurately.

Fig. 3-25 compares the circulation decays for velocity ratios of r=1.0 and r=0.5, 0.6 for

the two different grids. In both cases, the experimentally observed trend of increasing

decay with decreasing velocity ratio [18] was observed. Notwithstanding the initial

increase past the trailing edge, the streamwise circulation for r=0.5, 0.6 decayed at twice

the rate as for matched velocity ratios. This was a result of the velocity ratio between the

two streams, which increased the turbulent diffusivity.

The sensitivity of the thrust coefficients to the grid is shown in the table below.

Table 3-2
Sensitivity of the thrust coefficient to the method of grid generation

CASE	Structured-based Grid	Unstructured Grid	Percent Difference
convoluted plate	0.9357	0.8877	-5 %
α=22°, r=0.6,0.5	0.9150	0.8865	-3 %
α=30°	0.8673	0.8822	+2 %
α=35°	0.8147	0.8394	+3 %
α=45°	0.7595	0.8177	+8 %

Although the differences were not large, the thrust coefficient is quoted in industry to within 0.5% [33]. As such, the present computations exhibited more than the acceptable variation.

3.2.4 Effect of Smoothing Scheme

A true Laplacian and edge-based smoothing schemes were tested (cases A2, A5) with the recommended coefficients [3]. The Laplacian scheme only employed the second derivative terms while the edge-based scheme used both the second and fourth derivatives. Their shed circulations varied by less than 10%, but the downstream circulation was approximately 25% less for the true Laplacian smoothing (Fig. 3-26; cases A2, A5). The edge-based scheme's circulation increased for 3 wavelengths downstream of the mixer's trailing edge. This was due to numerical error, as discussed in Section 3.2.2. Since the true Laplacian smoother did not exhibit this error, it should be used in general.

The magnitude of the smoothing scheme's effect illustrated that the circulation decay could not be predicted accurately using the three-dimensional Navier-Stokes solver. Note that the smoothing also affected the solution to which the solver converged to. In the true Laplacian solution, the slower stream was approximately 20% faster than in the edge-based one, giving a velocity ratio of 0.6 instead of 0.5. (The difference in velocity ratios was insufficient to impact the decay rate comparison). However, the smoothing can be utilized to obtain an experimentally measured decay rate by varying the constants, thereby changing the effective turbulent viscosity.

The thrust coefficient was 0.8865 for the edge-based smoother and 0.915 for the true Laplacian - a 3 % difference. Again, this was larger than the industry-accepted variation of 0.5%.

46

3.2.5 Effect of Turbulence Model

Two turbulence models were tested for the baseline case of $\alpha=22°$, r=0.6 (cases A5, A8). The first was the standard implementation of the k-ε model. The second was the Abramovich-Sabin relation used in the slender-body code. It was based on Prandtl's second hypothesis, and took the form,

$$\frac{\delta}{x} = k\frac{(1-r)}{(1+r)},$$ (3-8)

$$v_T = C\left(\frac{\delta}{x}\right)^2 \cdot \overline{U} \cdot x.$$ (3-9)

It was modified for density variations by Dimotakis [9], to give,

$$\frac{\delta}{x} = \varepsilon\,\frac{(1-r)}{\left(1+r\cdot s^{0.5}\right)}\cdot\left[1+s^{0.5} - \frac{(1-s^{0.5})}{1+2.9(1+r)/(1-r)}\right],$$ (3-10)

where s is the density ratio and ε is an empirical constant, set to 0.0875.

To account for laminar viscosity and for stability when x→0, a constant was added in the form of a Reynolds number based on the trailing edge circulation, $Re_\Gamma = \Gamma/v$. The diffusivity was then,

$$v_T = \frac{1}{2\pi}\cdot\left(\frac{\delta}{x}\right)^2 \cdot \overline{U} \cdot x + \frac{\Gamma}{Re_\Gamma}.$$ (3-11)

This model was only valid, and thus applied, in the downstream shear-layer region. Over the lobes the k-ε model was used. Since the k-ε model has been optimized and shown to model internal flows accurately [4, 5], only the downstream region was of interest for the comparisons.

Figure 3-27 shows that the circulation at the trailing edge and subsequent evolutions matched for the two models. Also, the thrust coefficients differed by less than 0.5% (k-ε, 0.915; shear layer, 0.918). It was evident that the turbulence model did not affect the primary variables of interest.

The simplified turbulence model was developed for free shear layers with no pressure gradients. Since it matched the results of the k-ε model, this suggests that the pressure gradients in the lobed mixer flow field did not affect the turbulent diffusivity. The general deficiencies of the k-ε model and its use for unbounded free shear layer flows were not a concern given the negligible effect of changing models.

3.2.6 Effect of Boundary Layer Grid Density

To investigate the effect of the boundary layer grid density and determine the optimal number of elements, the baseline case of $\alpha=22°$, r=0.6 was run for 2, 6 and 11 boundary layer elements (cases A5, A6, A7). Fig. 3-28 shows the circulation evolution for these three cases. The 2 and 11 element meshes had short downstream regions. Over the lobe, the wall functions in the solver were able to compensate for the sparse 2 element boundary layer. However, past the trailing edge, it was evident that 2 elements were insufficient to model the boundary layer and thus predict the circulation. The shed trailing edge circulation for 6 and 11 elements were essentially the same. The slightly increased circulation for 11 elements past the trailing edge was probably spurious, as the greater number of elements also resulted in more stretching and larger changes in the aspect ratio. As such, six boundary layer elements was appropriate for attached lobed mixer flows.

The thrust coefficients for the three cases were 0.849, 0.915 and 0.955 (2, 6 and 11 boundary layer elements respectively). As noted in the discussion of the circulation, two boundary layer elements were insufficient to resolve the flow, so its thrust coefficient was

not expected to match the others. However, the 4% difference between the 6 and 11 element cases was still greater than the acceptable variation.

The largest penetration angle for which the flow was attached over the lobes was $\alpha = 30°$. Viscous effects were more pronounced, with the boundary layer being larger than for $\alpha = 22°$ (see Section 4.2.1 for a more detailed discussion). The displacement thicknesses normalized by the wavelength, δ_d/λ, at the trailing edge for the low and high velocity streams were respectively 0.081 and 0.0535 for 7 elements and 0.0845 and 0.0464 for 11 elements, differences of 4%. As such, 7 elements provided acceptable boundary layer resolution for attached flows.

The largest penetration angle that was tested was $\alpha = 45°$, for which separation was extensive. The displacement thicknesses normalized by the wavelength, δ_d/λ, at the trailing edge for the low and high velocity streams were respectively 0.23 and 0.085 for 7 elements and 0.10 and 0.11 for 11 elements, differences of 100% and 15%. Figs. 3-29 a,b and 3-30 a,b show the high and low velocity Mach levels on the lobed mixer surface for 7 and 11 elements. The high velocity sides (Fig. 3-29 a,b) corresponded well. The low velocity side for 11 elements showed more extensive separation than for 7 elements. Therefore, with separated flows, at least 11 elements are required to properly resolve the boundary layer.

3.3 Mixed Subsonic/Supersonic Inlet Conditions

NEWT was developed for either fully subsonic or fully supersonic inflow and outflow; however, a topic of interest is the mixing of supersonic and subsonic streams. It was straightforward to specify the appropriate inflow supersonic and subsonic boundary conditions on either side of the inlet splitter plate. However, the outflow had both subsonic and supersonic streams mixed together. As a first approximation, the outlet static pressure

was fixed (subsonic boundary conditions) to model the exit as a plenum or atmosphere. To obtain a physical solution, this exit pressure had to be specified within approximately 1% of the equivalent atmospheric exhausting pressure [6]. It was found that for these conditions, the solver was very grid sensitive particularly with respect to the smoothing. If adjacent elements changed aspect ratios by more than a factor of 2, there was significant influence in the supersonic stream upstream of the flat plate trailing edge in the form of pressure waves. Their amplitude was on the order of 2-3 inlet dynamic head. The only upstream influence in a supersonic stream could be from the smoothing[†], and since the schemes were grid-sensitive, the smoothing was concluded to be the cause of the erroneous pressure waves.

With the proper outlet pressure, a solution for a flat mixing plate with inlet streams at Mach 0.26 and 1.2 was obtained. The grid was structured and adjacent elements varied by less than 50% in size. Figs. 3-31 to 3-33 show cross-sections of the static pressure, Mach number and entropy. The entropy field was instructive as it highlighted non-physical aspects of the solution: the other variables had complicated features in compound sub/supersonic flow, and problems were not always evident. At the outlet boundary of this solution, there was a decrease in the entropy (Fig. 3-33) and a jump in the pressure (Fig. 3-31) to meet the specified boundary condition. These defects could be eliminated by iterating on the exit back pressure, but were not because of time constraints and the limited utility of the solution.

A solution for a lobed mixer geometry with the same flow conditions failed to converge. There was significant upstream influence in the supersonic stream, including the aforementioned pressure waves, implying problems with the grid and/or smoothing. To

---

[†] Upstream influence can also occur via a subsonic boundary layer. However, these effects were observed when the surfaces were specified as inviscid.

obtain a converged solution, the true Laplacian smoothing scheme may be tested.

Alternatively, the method of characteristics may be applied at the outflow boundary.

3.4 Summary

The shed trailing edge circulation could be evaluated with confidence using the viscous

Navier-Stokes solver for cases with thin boundary layers. For attached lobed mixer flows,

6 boundary layer elements was optimal. For separated flows, more elements are required.

The circulation decay downstream of the trailing edge could not be predicted accurately.

However, from a sensitivity analysis it was found that the far downstream (t*>6) the area-

averaged scalar mixedness could be estimated to within 20% even with an uncertainty of an

order of magnitude in the circulation decay.

If more accurate mixing rates are required, then the smoothing constants can be adjusted to

match the decay rate of the code to experimentally measured values. True Laplacian

smoothing should be used in general. To capture the downstream vorticity, resources

should be directed to generating the best possible grid. The table below outlines the

approximate uncertainty in the downstream circulation for the various factors that were

considered.

Table 3-3
Sources of uncertainty in the downstream circulation decay

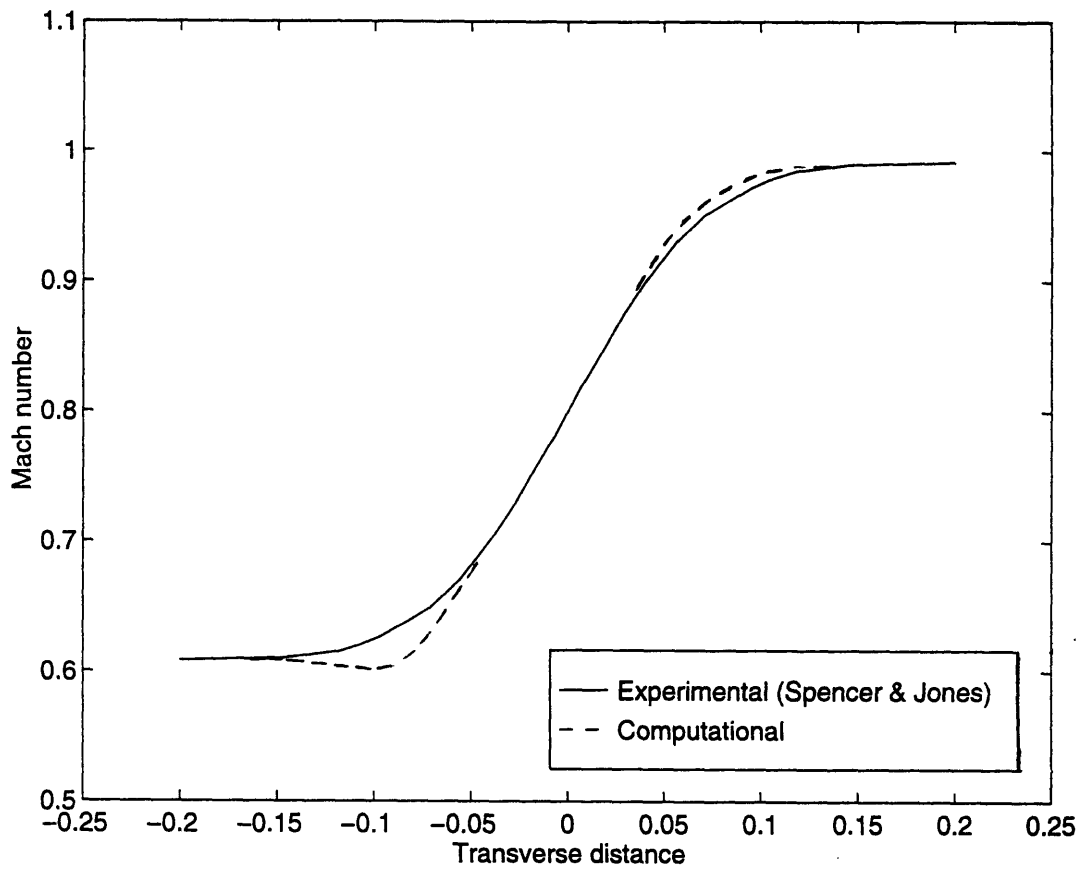| Factor	Potential Uncertainty in Circulation Decay
Grid	100 %
Smoothing	15 %
Boundary layer resolution	5 %
Turbulent model	negligible
TOTAL (comparison to experiment)	≈100%

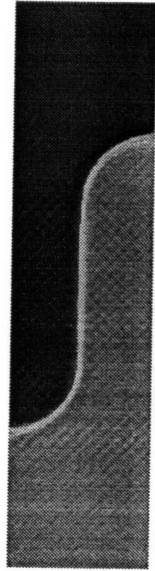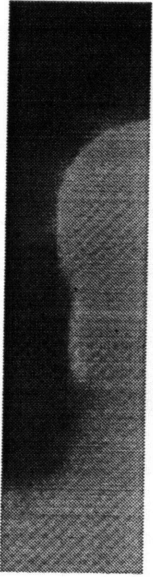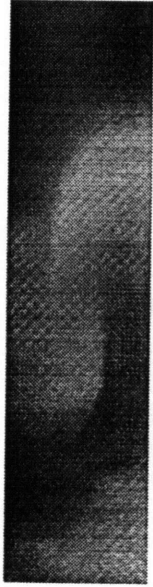**Figure 3-1**   **Flat plate velocity profile - Comparison of computed and experimental (Spencer and Jones) [30]**

x* = 0

x* = 1.0

x* = 3.0

x* = 6.0

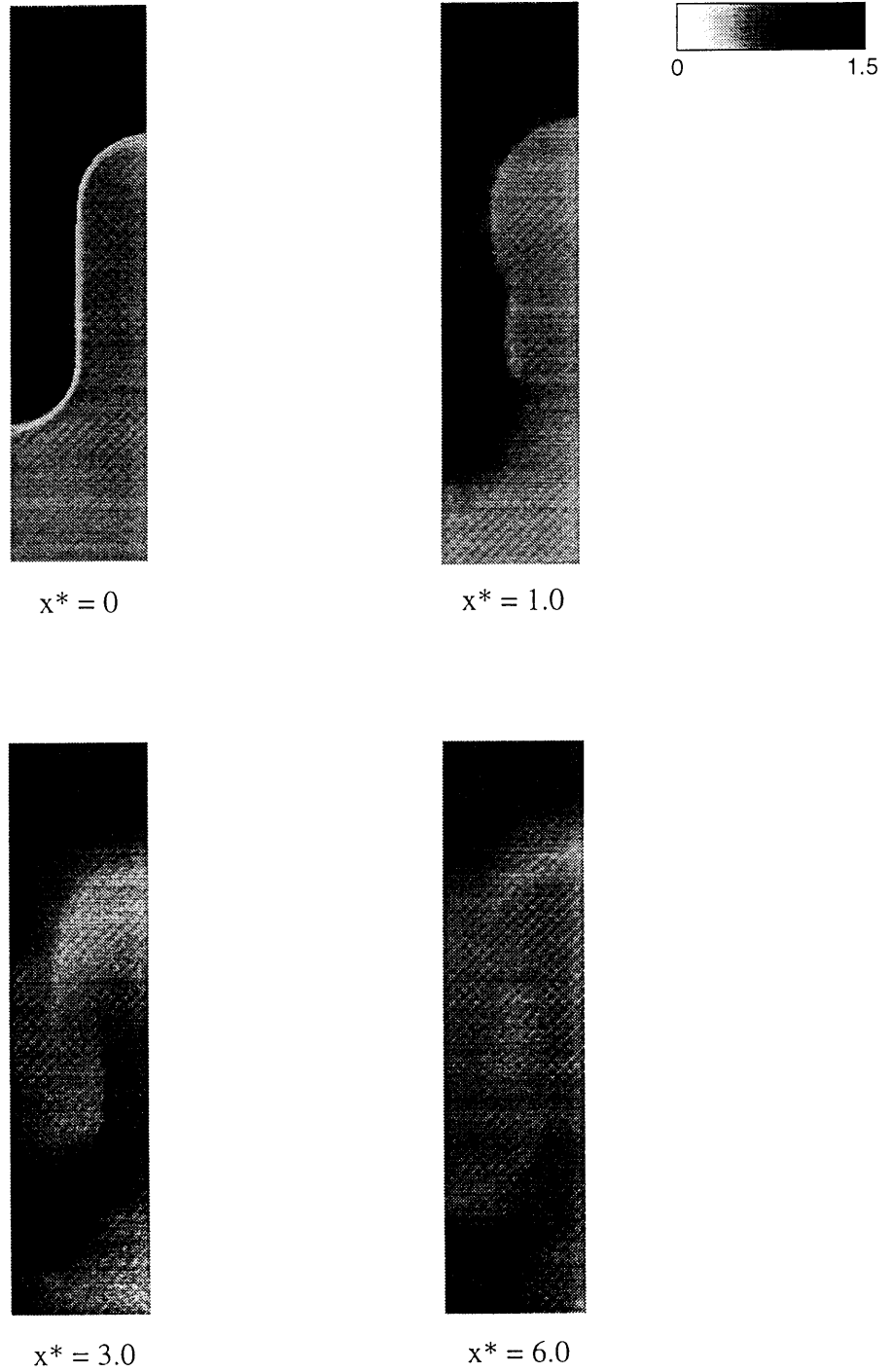Figure 3-3 M_{sw} at x˙ = 1, 3, 6 and 12 for ADM ($\alpha=22°$, r=0.6)

54

x* = 0   x* = 1.0

x* = 3.0   x* = 6.0

Figure 3-3 M_{sw} at x' = 1, 3, 6 and 12 for ADM (α=22°, r=0.6)

- - - - - - - - - contour, C, used to calculate circulation

———————— boundary of the computational domain
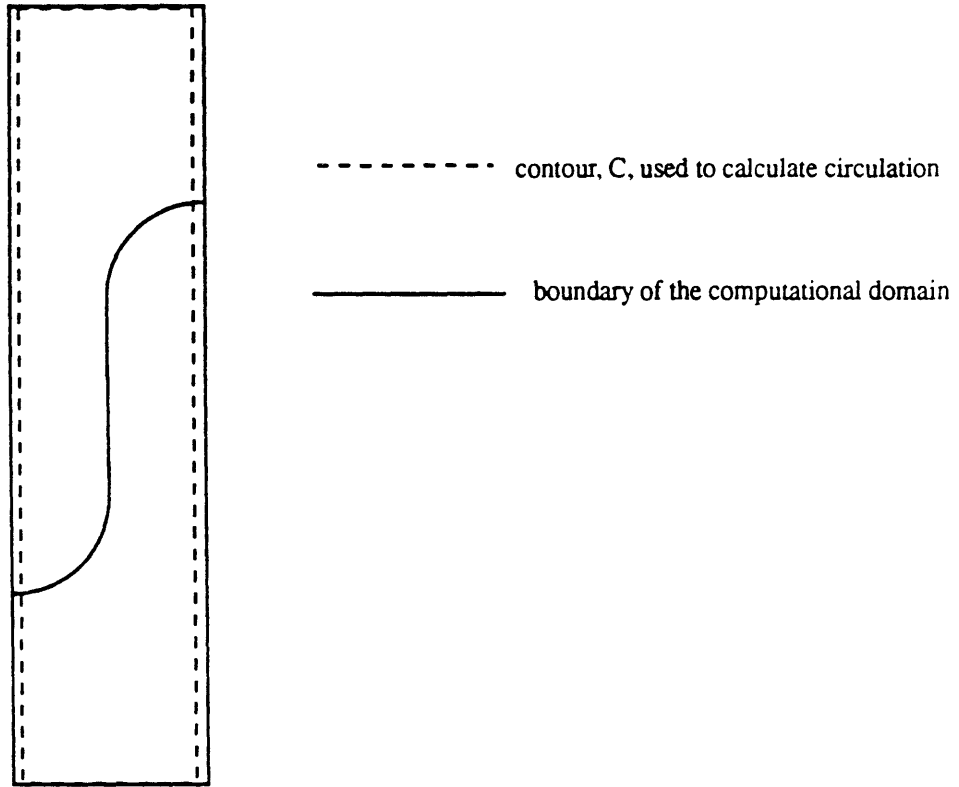
Figure 3-4   **Path for evaluation of Γ_{sw}^{*} [20]**
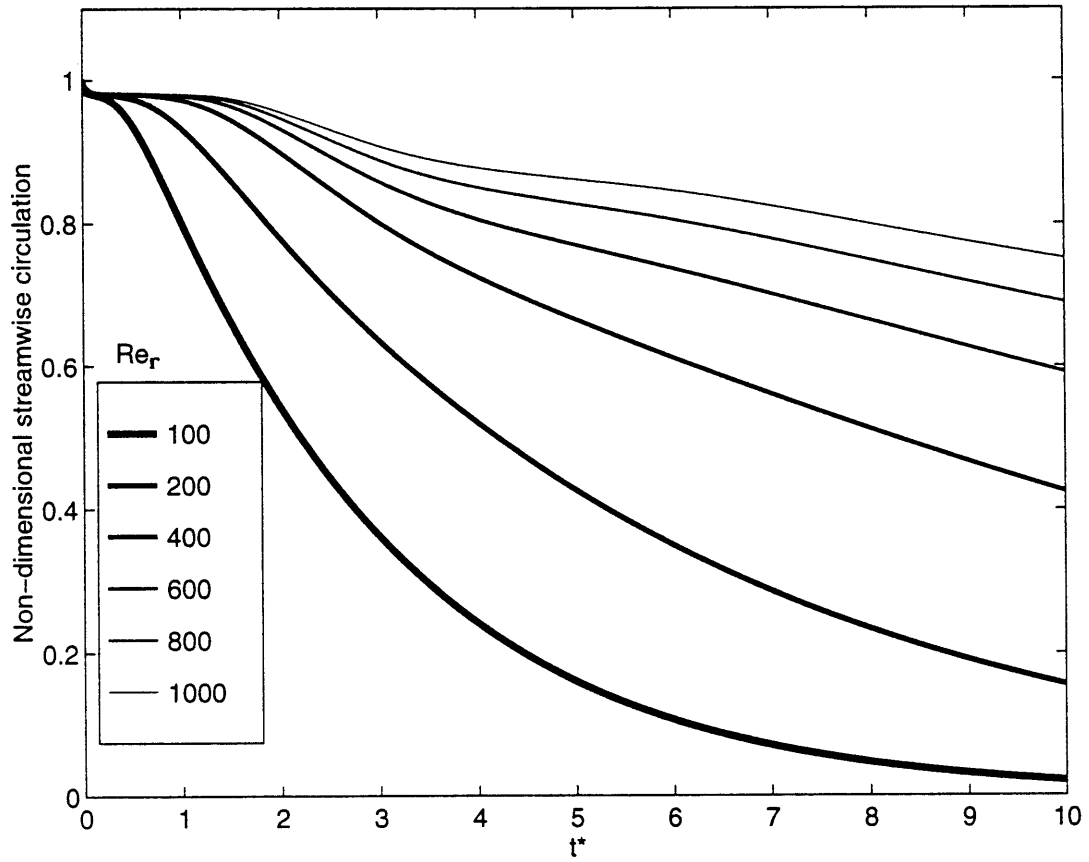
Figure 3-5   Effect of Re_Γ on the slender-body downstream
streamwise circulation decay   (r=1.0)
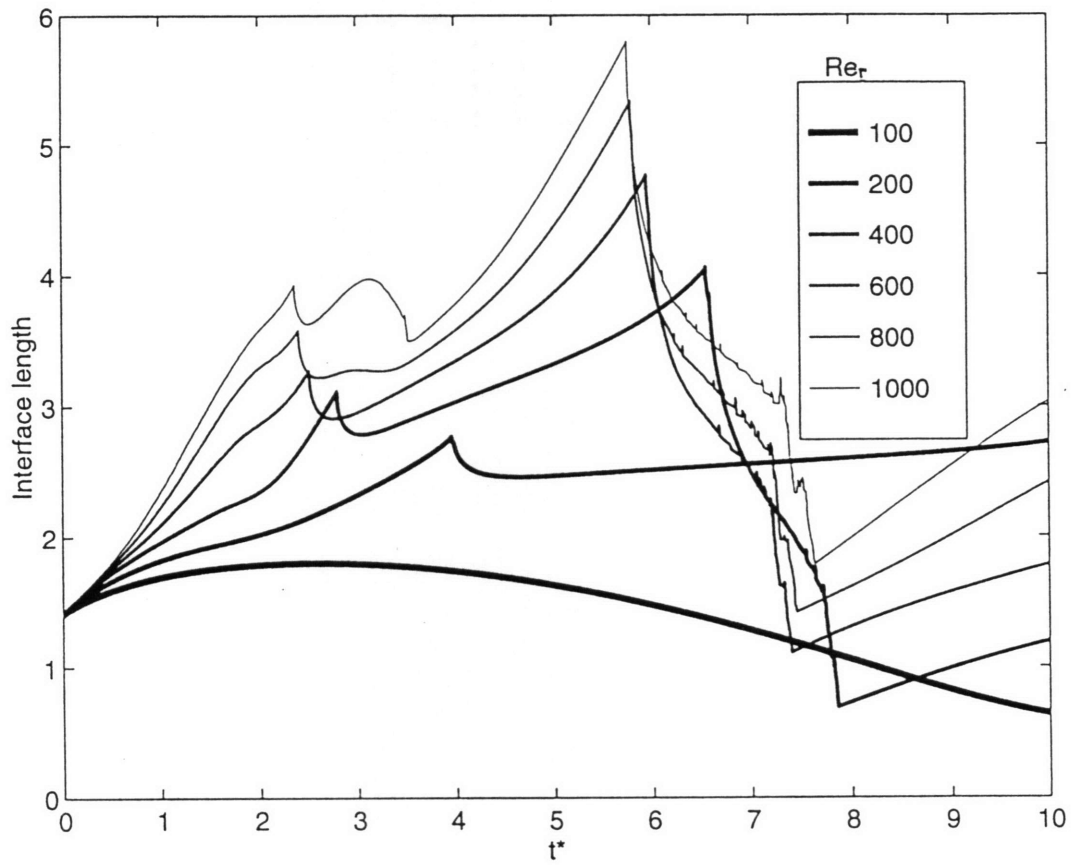
Figure 3-6   **Effect of Re$_\Gamma$ on the interface length   (r=1.0)**

Passive scalar

-1 $\blacksquare$ +1

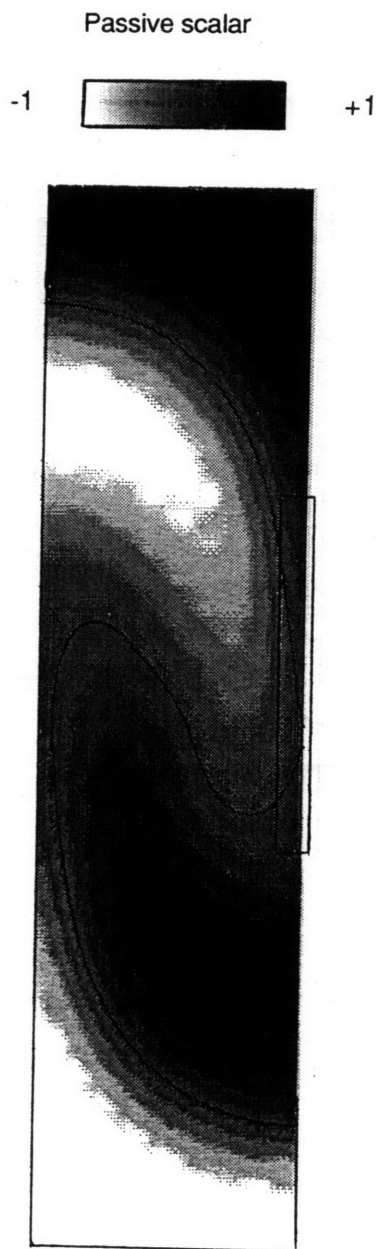**Figure 3-7**

Passive scalar plot showing diffusion of "mushroom" structure beyond the symmetry boundary (r=0.7, α=22°)
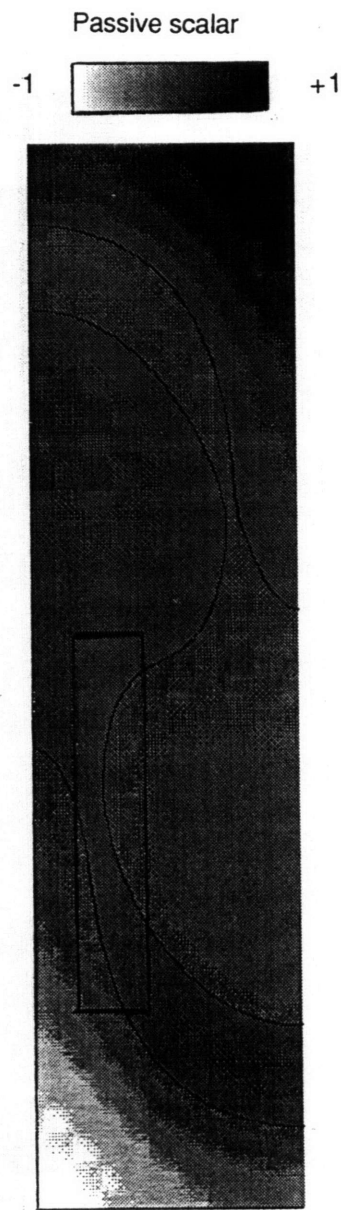
Passive scalar

-1   +1

Figure 3-8

Passive scalar plot showing first stage of reforming the planar shear layer (r=0.7, α=22°)
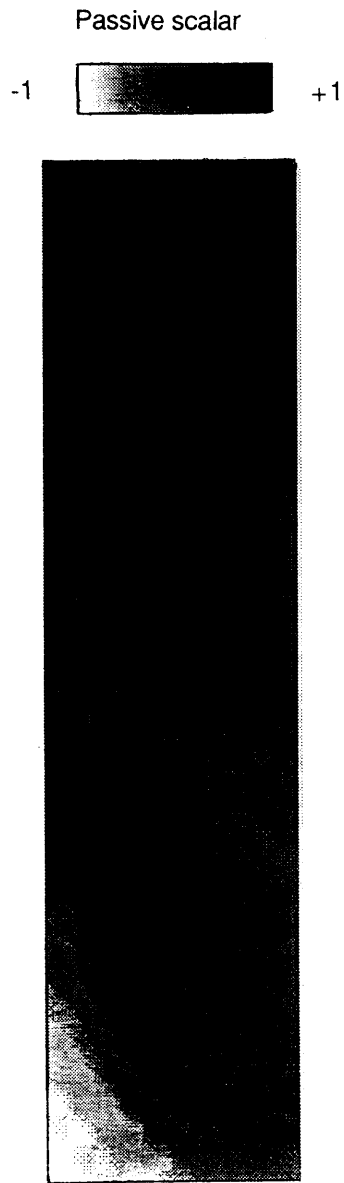
Passive scalar

-1 +1

Figure 3-9

Passive scalar plot showing the reforming of a planar shear layer (r=0.7, α=22°)
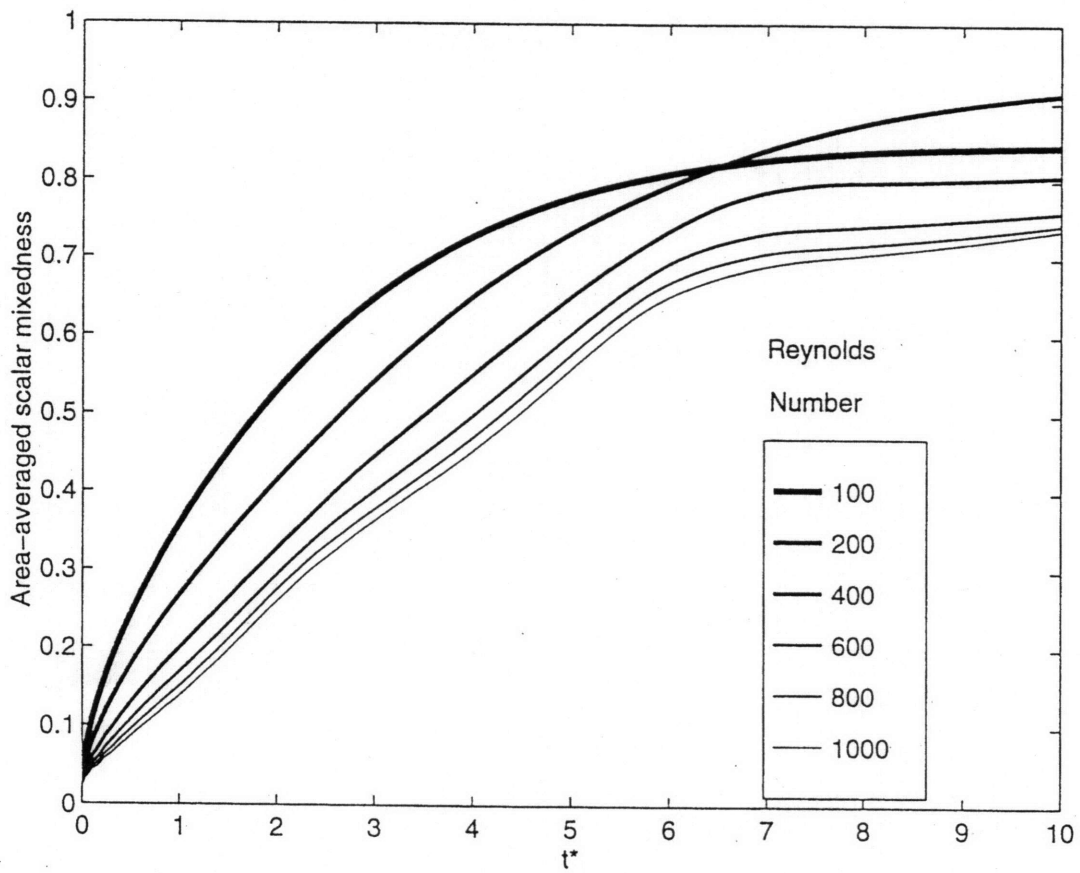
Figure 3-10   Effect of Re_Γ on the area-averaged scalar mixedness (r=1.0)

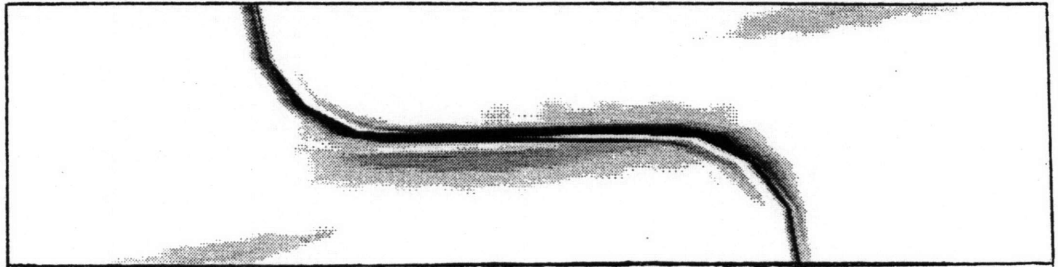Streamwise vorticity / $\overline{U}\lambda$

0 ▓▓▓▓▓▓ 25

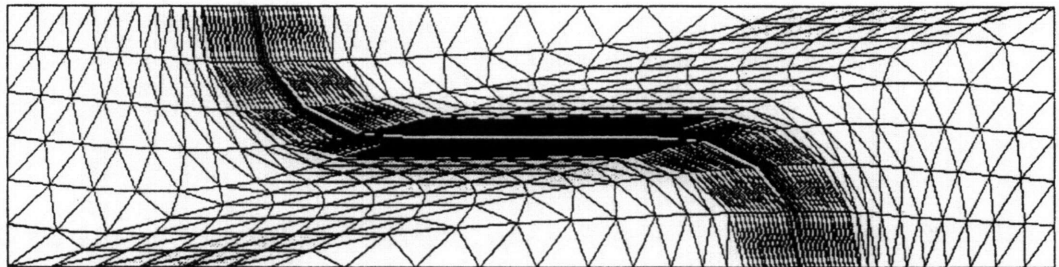Figure 3-11   Axial plane showing spurious corner vorticity in structured-based grids

Figure 3-12   Axial plane showing structured-based grid

62
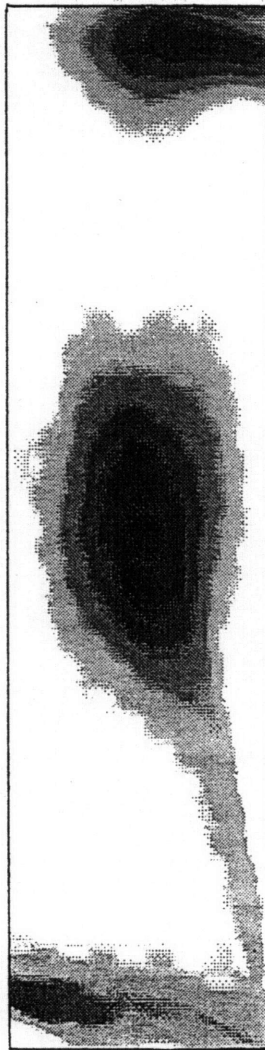
Streamwise vorticity / $\overline{U}\lambda$

0 [ ] 25

Figure 3-13   Spurious vorticity growth from boundaries of structured-based grid in downstream region (x*=5.5; r=0.6, α=22°)

63
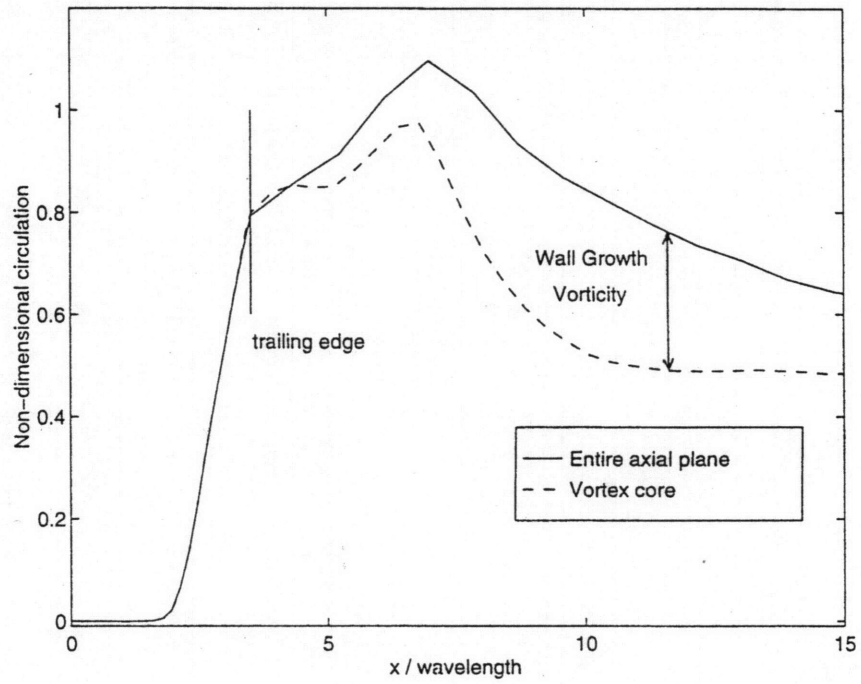
Figure 3-14   Downstream streamwise circulation showing the effect of spurious wall growth vorticity   (r=0.6, α=22°)
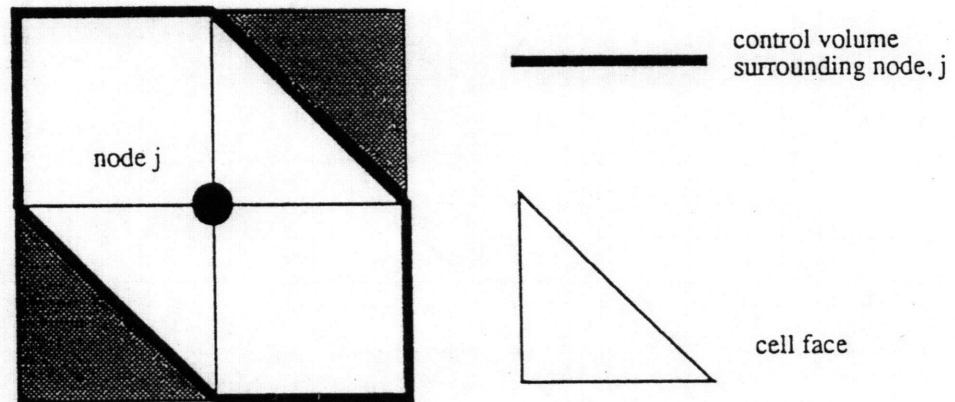
Figure 3-15   Typical control volume about a node in the structured-based grid   [20]

Streamwise vorticity / $\overline{U}\lambda$

0   25
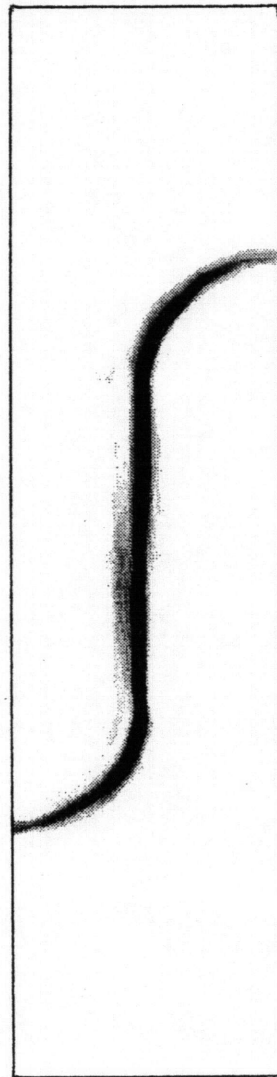
Figure 3-16   Vorticity distribution at the trailing edge of an unstructured grid ($\alpha=22°$, r=0.6)

Streamwise vorticity / $\overline{U}\lambda$

0 — 25
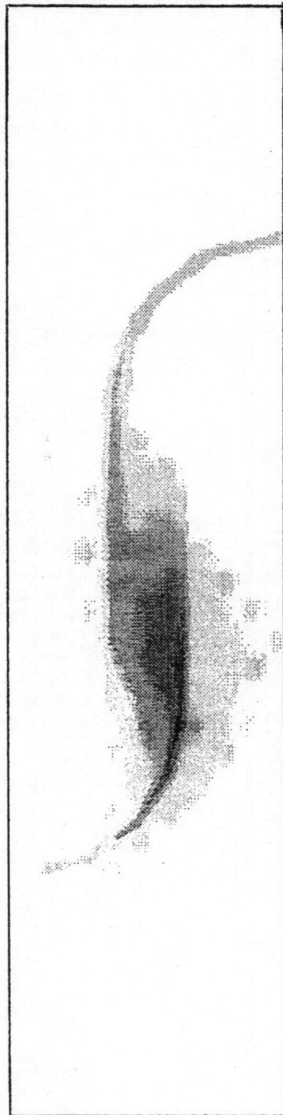
Figure 3-17   Spurious vorticity in downstream region from
unstructured-mesh boundary layer elements
(x*=1.25; r=0.6, α=22°)

Figure 3-18   Effect of grid generation on downstream streamwise circulation evolution (ADM; α=22°, r=1.0)
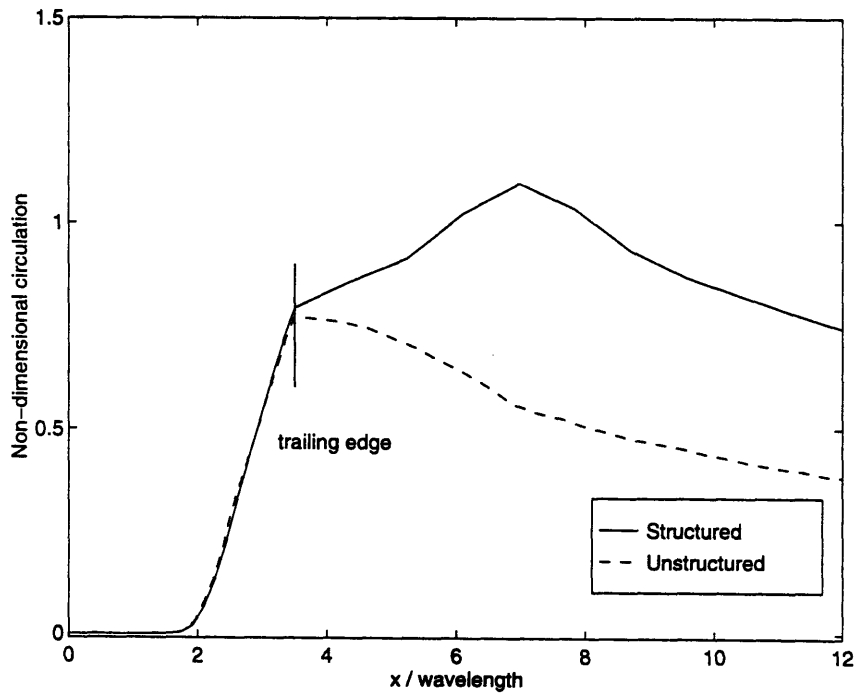
Figure 3-19   Effect of grid generation on downstream streamwise circulation evolution (ADM; α=22°, r=0.5, 0.6)
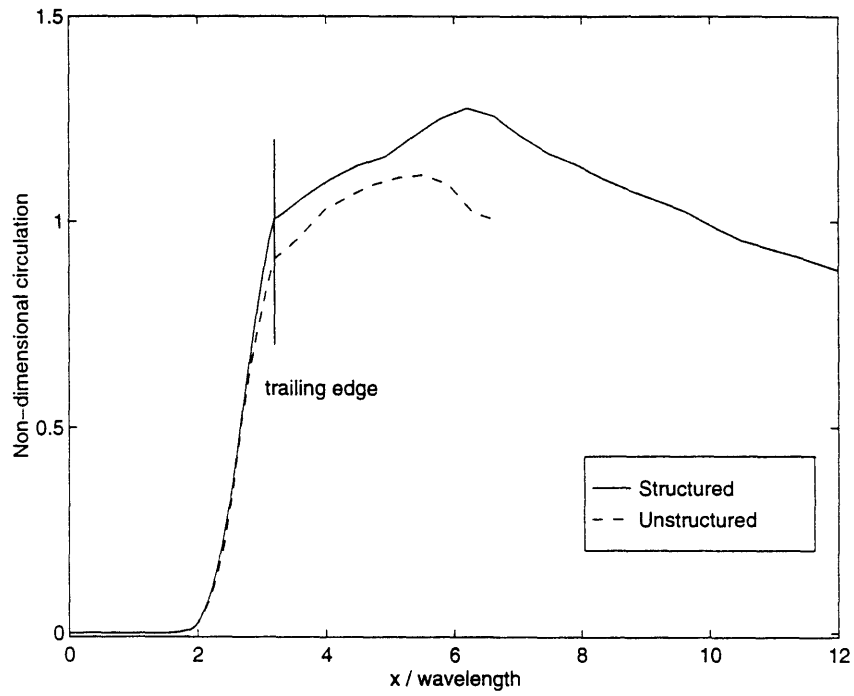
Figure 3-20   **Effect of grid generation on downstream streamwise circulation evolution (ADM; $\alpha=30°$, r=0.5, 0.6)**
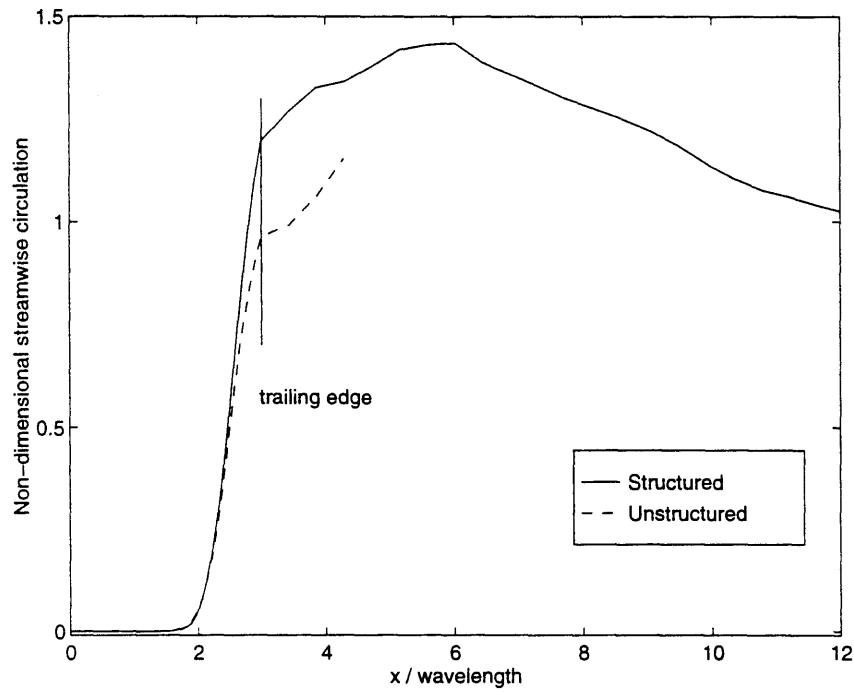
Figure 3-21   **Effect of grid generation on downstream streamwise circulation evolution   (ADM; $\alpha=35°$, r=0.5, 0.6)**
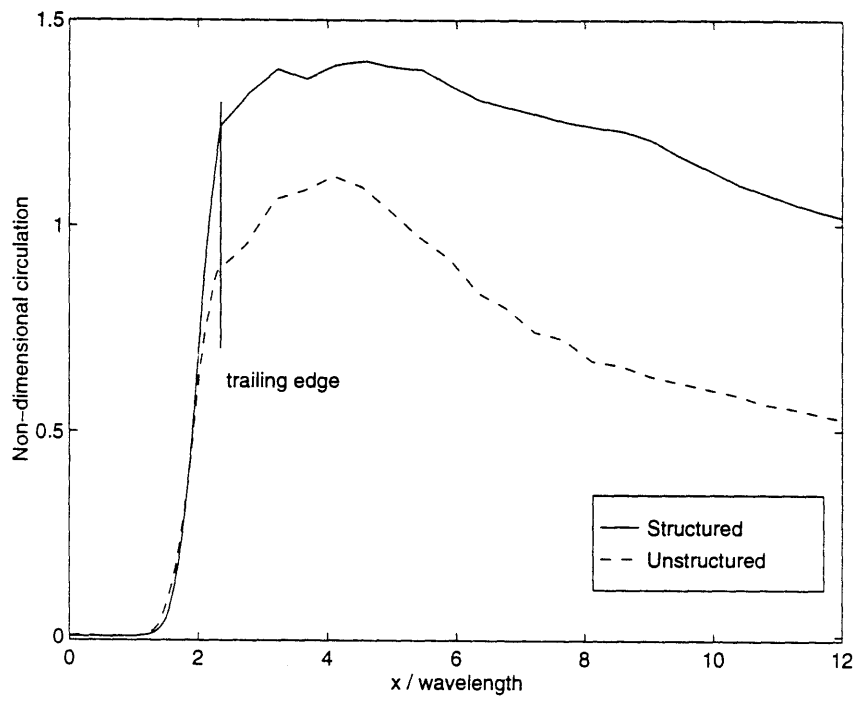
Figure 3-22   **Effect of grid generation on downstream streamwise circulation evolution (ADM; α=45°, r=0.6)**
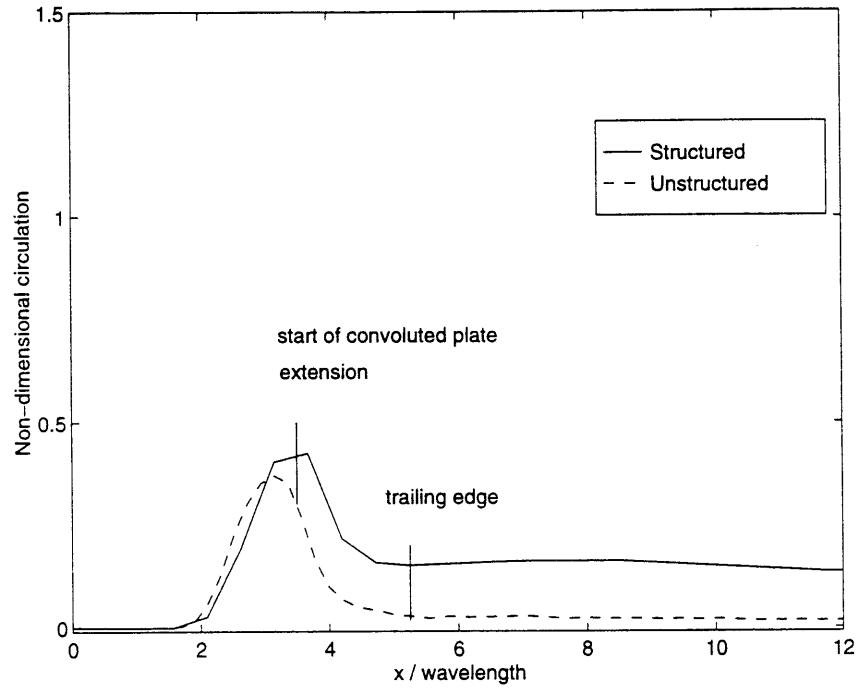
Figure 3-23   Effect of grid generation on downstream streamwise
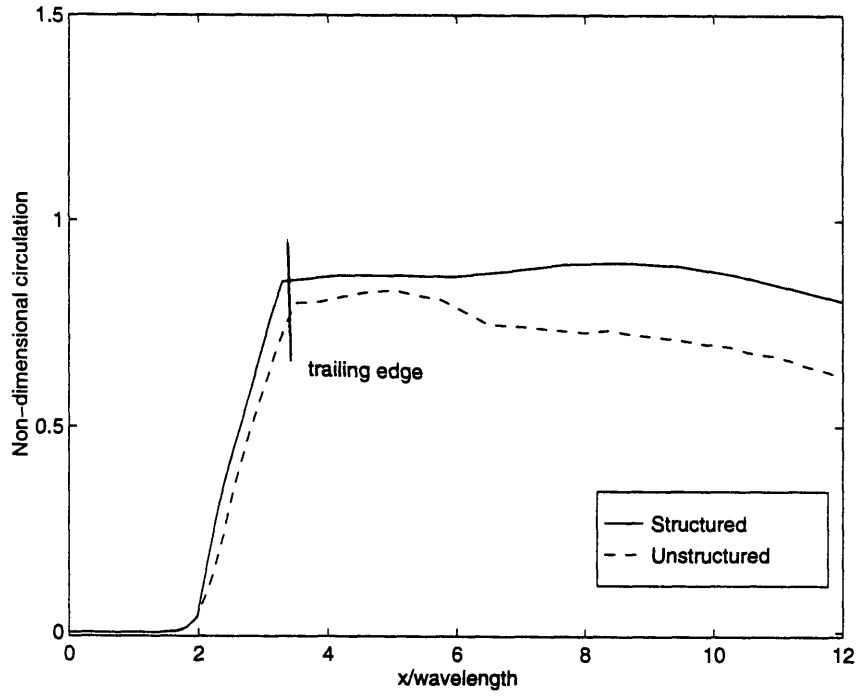circulation evolution (CP; α=22°, r=0.4, 0.5)
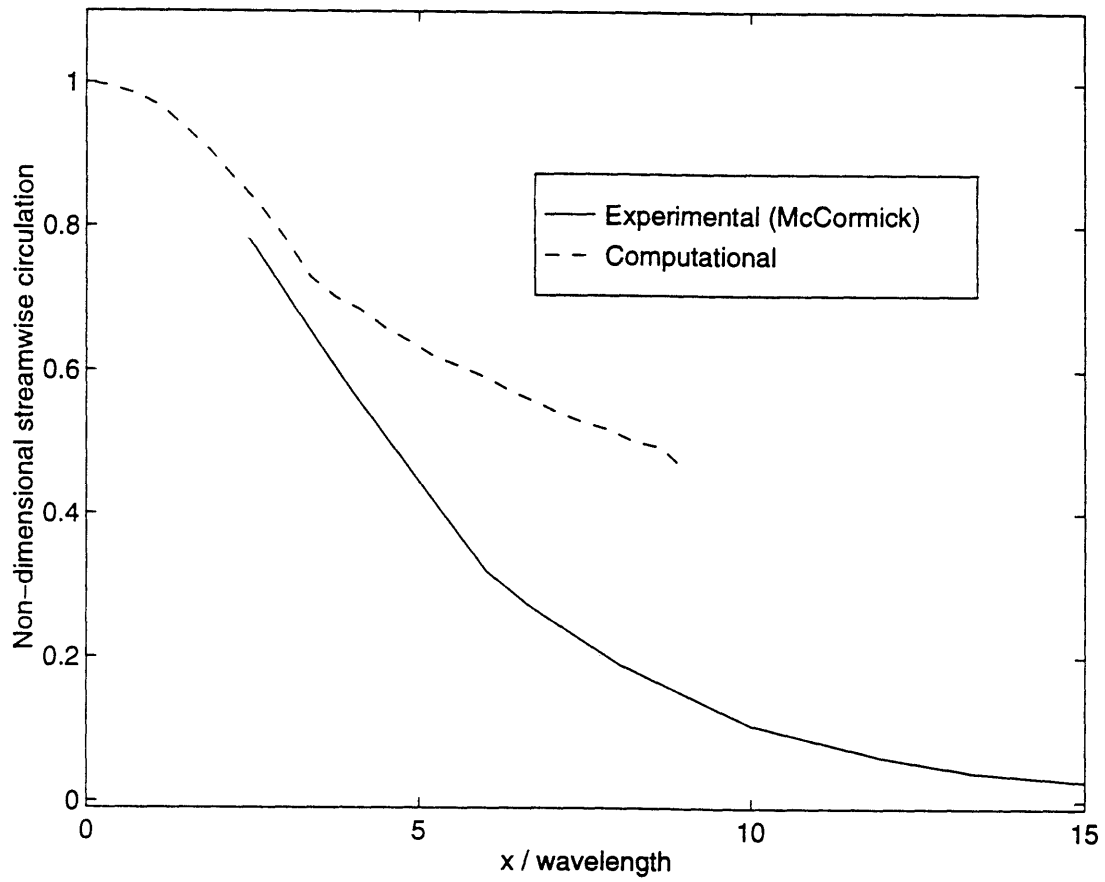
Figure 3-24   **Comparison of computed and experimental (McCormick) circulation evolutions [18]**
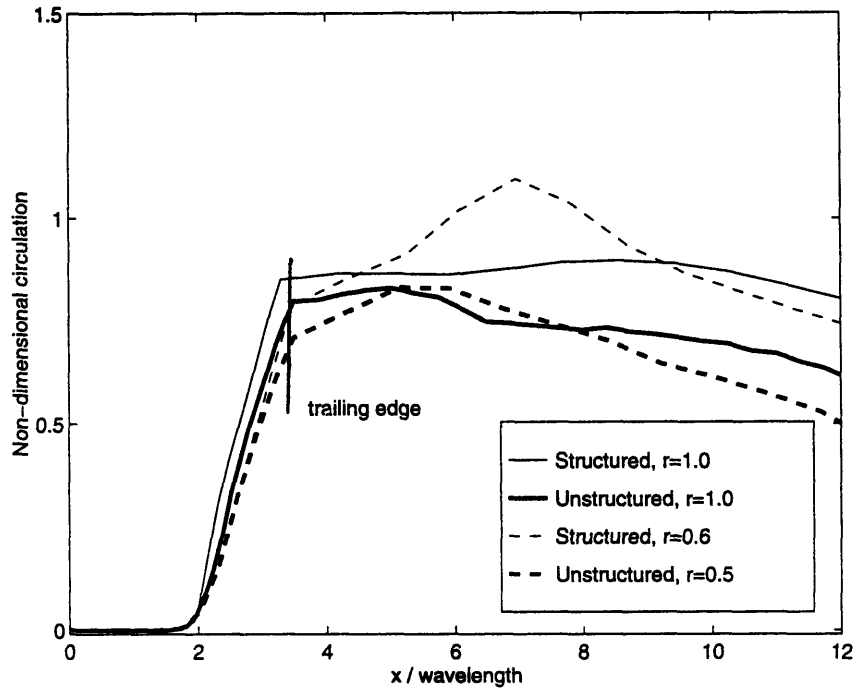
Figure 3-25 Effect of velocity ratio on streamwise circulation decay ($\alpha=22°$)
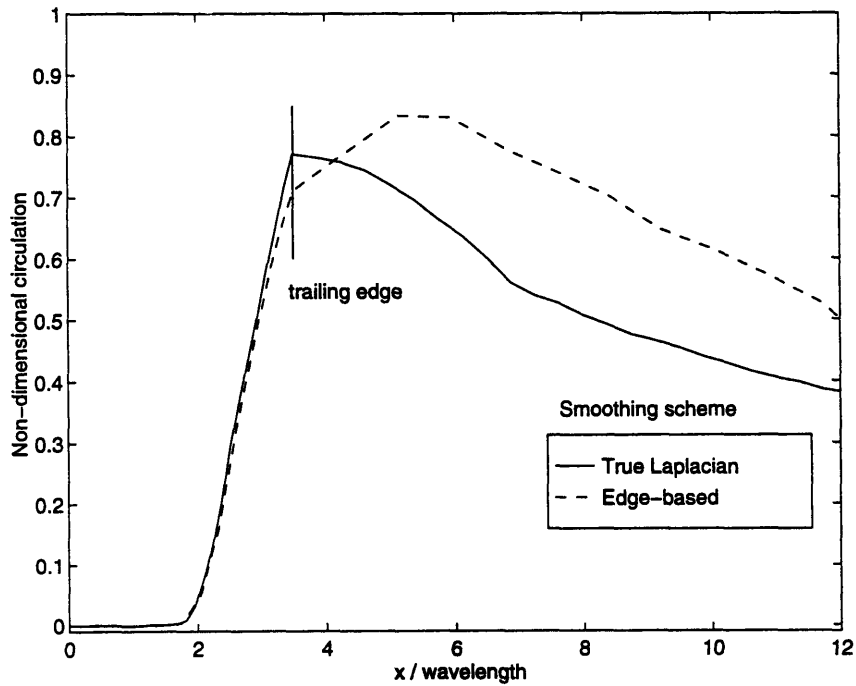
Figure 3-26 Effect of smoothing scheme on streamwise circulation decay ($\alpha=22°$, r=0.5, 0.6)
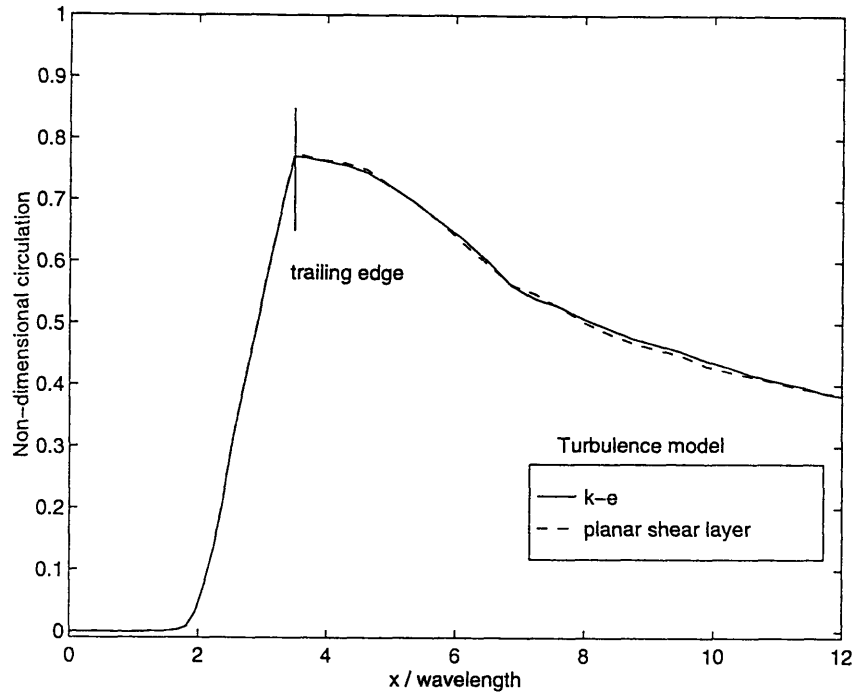
Figure 3-27   **Effect of turbulence model on streamwise circulation decay (α=22°, r=0.6)**
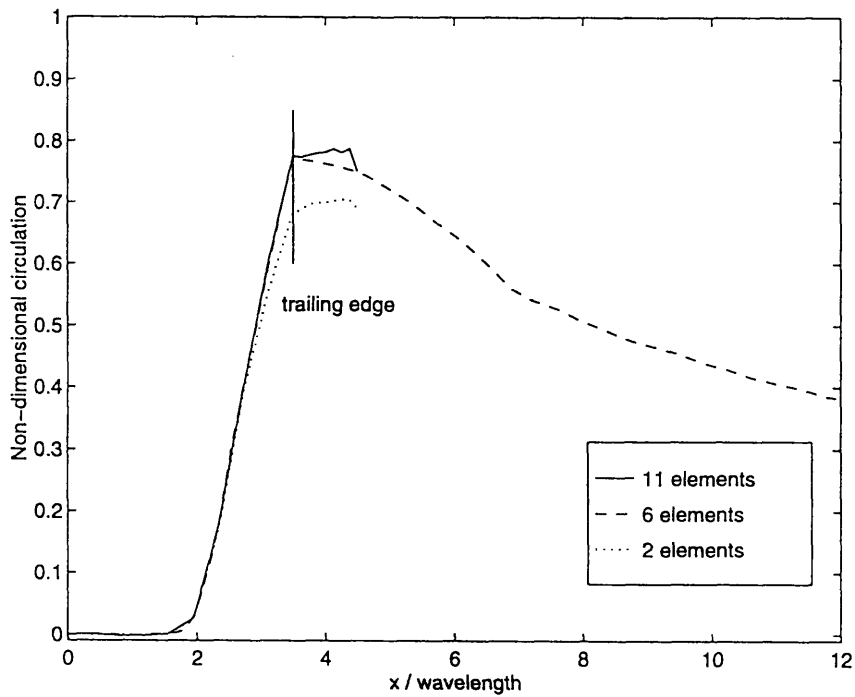
Figure 3-28   **Effect of boundary layer grid density on streamwise circulation decay (α=22°, r=0.6)**
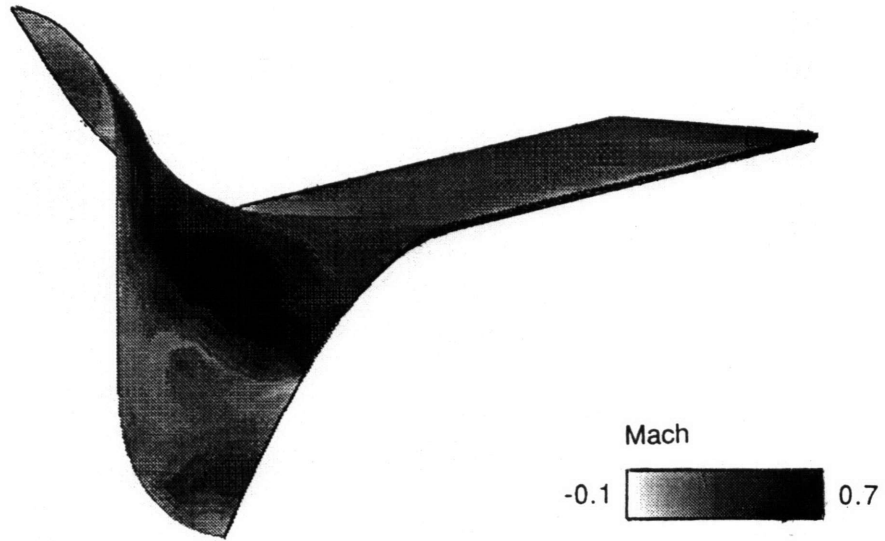
Figure 3-29a Mach number on high velocity lobed mixer surface (α=45˚) - 7 elements
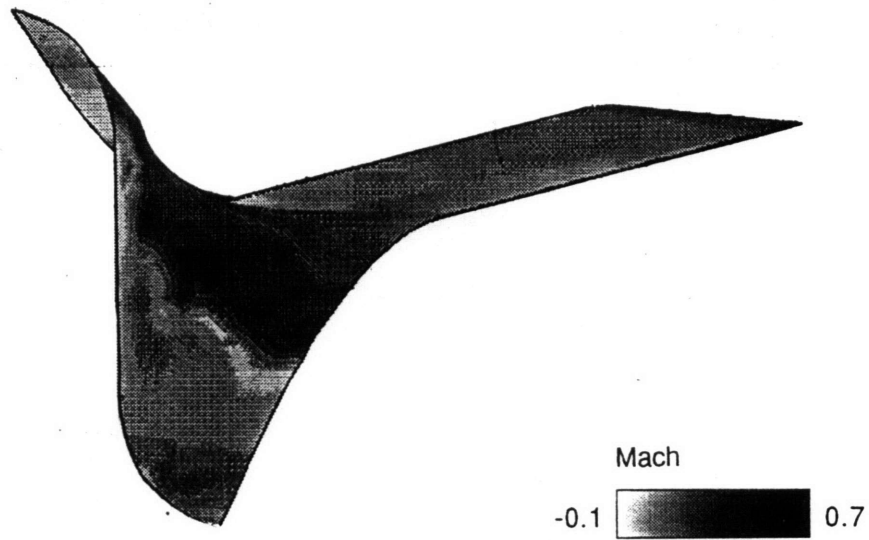
Figure 3-29b Mach number on high velocity lobed mixer surface (α=45˚) - 11 elements

Mach

-0.1 0.7
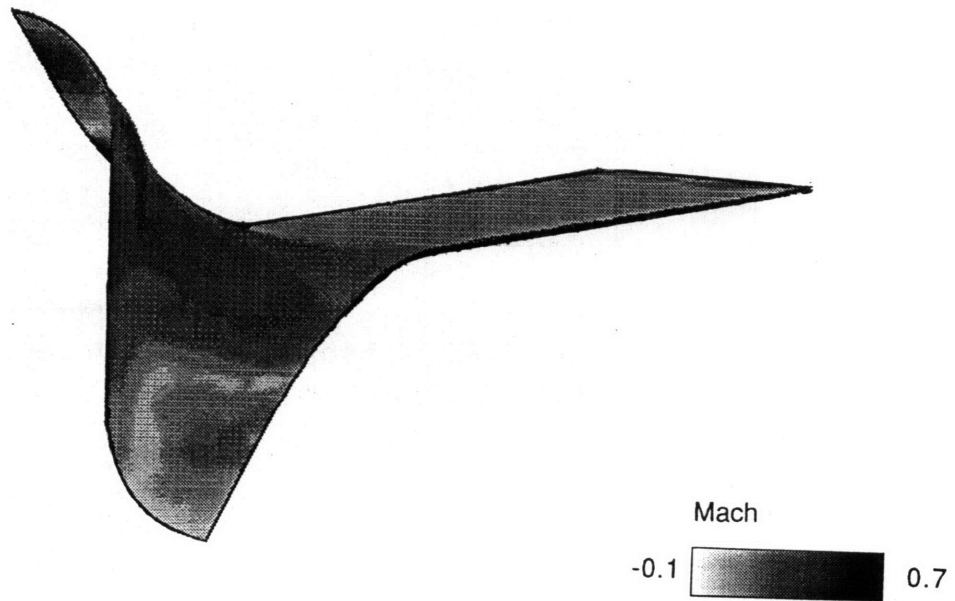
**Figure 3-30a   Mach number on low velocity lobed mixer surface
(α=45˚) - 7 elements**

Mach

-0.1 0.7
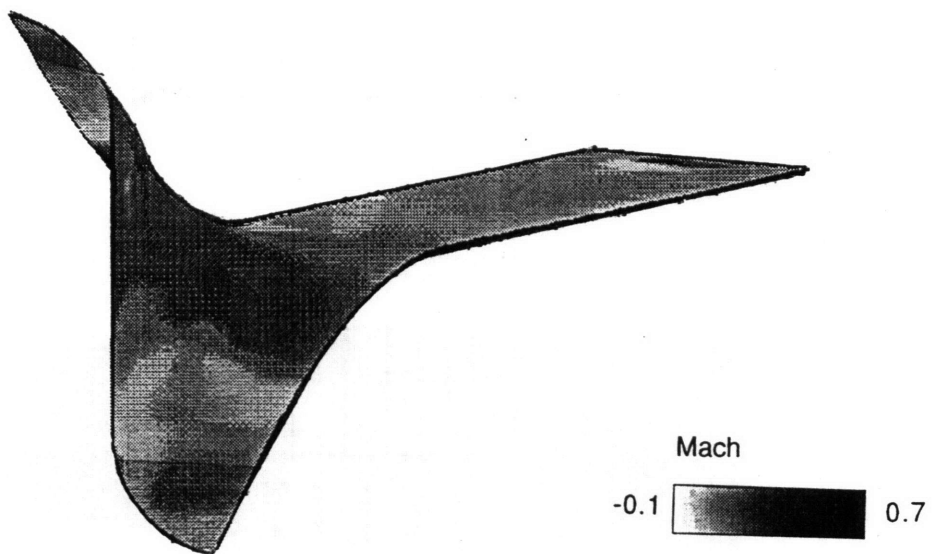
**Figure 3-30b   Mach number on low velocity lobed mixer surface
(α=45˚) - 11 elements**

Static pressure/

Inlet dynamic head

-8

-12
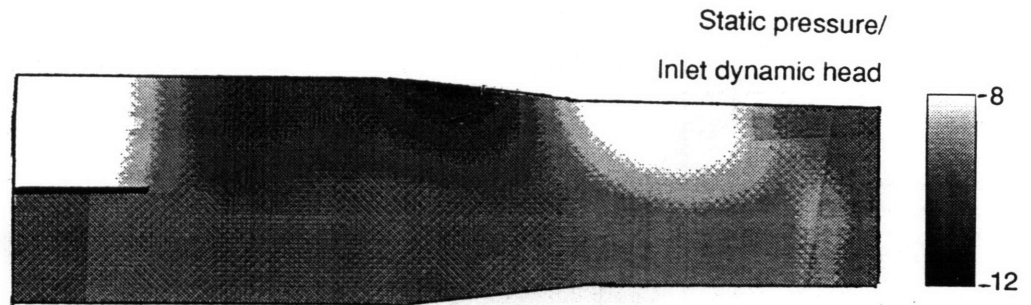
Figure 3-31   **Static pressure profile of flat plate with combined supersonic/subsonic boundary conditions (Inlet Mach number 0.26, 1.2)**

Mach

-0

-2
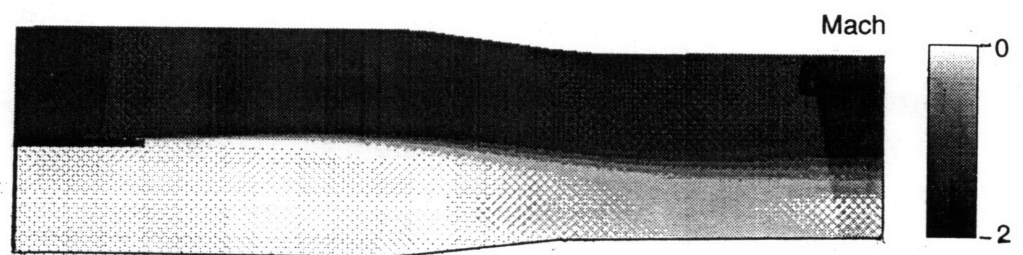
Figure 3-32   **Mach number profile of flat plate with combined supersonic/subsonic boundary conditions (Inlet Mach number of 0.26, 1.2)**

Entropy/

Inflow entropy

-0.9

-1.1

Figure 3-33   **Entropy profile of flat plate with combined supersonic/subsonic boundary conditions (Inlet Mach number of 0.26, 1.2)**

Chapter 4
Investigation of Viscous Effects in Lobed Mixers

In the previous chapter the ability of NEWT to capture the flow physics over lobed mixers was established. In doing so, it was used to investigate the viscous effects in lobed mixers. Computations and measurements of [29] have shown that under certain conditions significant boundary layer growth occurs in the lobe, so that it is filled with low momentum fluid. The aim of this study was to examine the impact of the boundary layer at the inlet and in the lobe on the flow and mixer performance. Specifically, the following were determined:

(i)   How the boundary layer in the lobe varied with the penetration angle.

(ii) The effect of the boundary layer in the lobe on the magnitude of the streamwise circulation shed from the trailing edge.

(iii) The effect of the inlet boundary layer profile on the performance of a lobed mixer.

(iv) The principal lobed mixer loss sources and how the losses varied with the penetration angle and velocity ratio.

4.1 Matrix of Numerical Computations

To assess the effect of attempting to increase the *streamwise* circulation, computations were carried out for mixers with half-angle (or penetration angle), α, of 22°, 30°, 35° and 45° and a convoluted plate.

To assess the effect of the inflow boundary layer two profiles were employed. The majority of the computations were carried out with a uniform total pressure profile at the inflow to the computational domain, such that the displacement thickness, δ_d/λ, at the mixer inlet was on the order of 0.01 ("mixer inlet" refers to the beginning of the lobe and not the computational inflow plane). One calculation was carried out with a profile which gave $\delta_d/\lambda \approx 0.25$ at the mixer inlet. Table 4-1 details the computations that were carried out. Unstructured grids were employed with edge-based smoothing[†].

Table 4-1
Computational matrix for investigation into viscous effects in lobed mixers

Mixer	Penetration Angle (α)	Velocity Ratio (r)	δ_d/λ at inlet
(CP) C1	(22°)	0.4	0.01
(ADM) C2	22°	1.0	0.01
(ADM) C3	22°	0.5	0.01
(ADM) C4	30°	0.5	0.01
(ADM) C5	35°	0.5	0.01
(ADM) C6	45°	0.63	0.01
(ADM) C7	22°	1.0	0.25

As discussed in Chapter 3, the shed streamwise circulation at the trailing edge was evaluated with greater confidence than downstream in the mixing region. As a result, the primary focus in the investigation was on the value of the circulation at the trailing edge.

[†] In Chapter 4, true Laplacian smoothing was recommended in preference of edge-based smoothing. However, true Laplacian smoothing was not available for the calculations at the time they were performed. Since the shed circulations for the two smoothing schemes were within 10%, the choice of the scheme will not affect the conclusions.

4.2 Effect of Viscosity on the Lobed Mixer Flow Field and Shed Streamwise Circulation

4.2.1 Flow field Behavior with Increasing Lobe Penetration Angle

As the lobe penetration angle was increased the behavior of the flow in the lobe was altered as boundary layer blockage and separation become progressively more important. For a penetration angle of 22°, the computations showed no flow separation. For a 35° lobe angle, separation was observed close to the trailing edge and along the vertical wall of the lobe in the low velocity stream. For a 45° lobe, extensive separation was seen from halfway through the lobe to the trailing edge.

For lobed mixer flow fields with no flow separation and little boundary layer blockage, Skebe *et al.* [29] have shown that the trailing streamwise circulation can be estimated by assuming all the fluid leaves the mixer at the lobe penetration angle, α. If so, the shed streamwise circulation, Γ_{sw}, is given by,

$$\Gamma_{sw} \approx 2\ \bar{u}\ h \tan \alpha. \tag{4-1}$$

For $h/\lambda = 1$, Eq. (4-1) is written non-dimensionally as,

$$\Gamma_{sw}^{*} \approx 2 \tan \alpha. \tag{4-2}$$

As the lobe penetration angle was increased, or if the inflow boundary layer was significant compared to the lobe height, the assumptions that underlie Eq. (4-2) are less valid. The computations allowed assessment of the degree to which Eq. (4-2) was applicable as the penetration angle was increased.

Fig. 4-1 shows the computed circulation for the lobed mixer configurations compared to that given by Eq. (4-2). As the lobe penetration angle was increased, Eq. (4-2) over-

predicted the circulation by progressively larger amounts. For the largest angle (45°,

denoted C6 in Fig. 4-1) Eq. (4-2) and the computations differed by approximately a factor

of two. This difference was from the increased thickness of low velocity fluid (due to the

boundary layer and separated flow) in the lobe, which reduced the effective lobe angle and

height.

To examine this assertion, the boundary layer displacement thickness, δ_d, defined as,

$$\delta_d = \int_0^\delta \left(1 - \frac{\rho u}{(\rho u)_{max}} \right) dz,$$ (4-3)

was calculated at the lobe trough and peak for the lobe inlet and trailing edge planes (Fig. 4-

2). The displacement thicknesses in these regions were used to estimate an effective

penetration angle, α_{eff}, and height, h_{eff}, for each stream on either side of the lobed mixer,

as illustrated schematically in Fig. 4-2. Using these values, Equation (4-2) was modified

to,

$$\Gamma^*_{sw} \approx (h_{eff,1} / \lambda) \tan(\alpha_{eff,1}) + (h_{eff,2} / \lambda) \tan(\alpha_{eff,2}).$$ (4-4)

The computed circulations and those predicted by Eq. (4-4) are shown in Fig. 4-3. The

computed and predicted values were all within 5%, supporting the hypothesis that the

decrease in non-dimensional circulation was due to boundary layer blockage. For the 45°

lobe, in which significant flow separation occurred, the prediction based on the effective

angles and heights was within 1% of the computed circulation (C6 in Fig. 4-3)[†]. An

important conclusion drawn from these studies was that for the tested lobe geometry there

---

[†] It was shown in Section 3.2.3 that the shed trailing edge circulation varied by up to 40% (cases D1-D2; $\alpha=45°$) between structured-based and unstructured grids. This was due to differences in the calculated boundary layer displacement thickness - for the structured-based grid, the computations and Eq. 4-4 were still within 5%. This was also true in Section 3.2.6 for varying the boundary layer grid density. The validity of the hypothesis is independent of the accuracy of the calculated boundary layer thickness.

was no benefit in increasing the lobe penetration angle above 30° because the shed streamwise circulation was limited by the increased boundary layer blockage.

4.2.2 Effect of the Inlet Boundary Layer

The computations described in the previous section were carried out with a thin displacement thickness, δ_d/λ, at the lobe inlet of approximately 0.01. The effect of a greatly increased δ_d/λ of approximately 0.25 at the lobe inlet was also examined. Fig. 4-4 shows the Mach number field at the lobe trailing edge for the two different inlet displacement thicknesses with the velocity ratio, r, equal to 1.0. With $\delta_d/\lambda \approx 0.25$ a considerable portion of the lobe was filled with low momentum fluid. The trailing circulation was reduced by approximately 35% compared to the case with $\delta_d/\lambda \approx 0.01$, (C2 and C7 in Fig. 4-3). The circulation for this case, based on Eq.(4-4) and using the effective penetration angles and heights, was included in Fig. 4-3 (C7). Again, the simple estimate based on these effective values was in good agreement with the computed circulation, differing by less than 2%.

The computations showed the influence of viscous effects in the lobe. In particular, the magnitude of the shed streamwise circulation, which was directly linked to the mixing augmentation associated with the device [17, 18, 27], was significantly altered. These influences could be understood within the framework of the effective lobe penetration angle and height.

4.3 Losses in Lobed Mixers

An important question associated with the mixing enhancement from the streamwise vorticity was the penalty of obtaining it. It was thus of interest to characterize the total pressure loss incurred due to the trailing circulation compared to other losses in the overall process.

The losses examined were divided into two categories:

1) *Boundary layer losses*, including losses on (i) the lobe surface and (ii) the shrouds that corresponded to the lower and upper walls of the computational domain (Fig. 4-5).

2) *Mixing losses*, containing contributions from the mixing out of non-uniformities associated with (i) the boundary layer (ii) the trailing edge thickness and (iii) the velocity field at the trailing edge (Fig. 4-6).

Assessments of these losses were made as the velocity ratio was varied, keeping the trailing circulation constant (fixed penetration angle and lobe trailing edge geometry), and as the lobe penetration angle was varied, keeping the velocity ratio fixed. An examination of the relation between total pressure loss and thrust decrease was also carried out. In the discussion that follows the total pressure losses were expressed in the form of a loss coefficient, denoted C_{Pt}, in which the loss was non-dimensionalized by the difference between the mass-averaged inflow total and static pressures, *i.e.*,

$$C_{Pt} \equiv \frac{\Delta P_T}{(\overline{P}_T^m - \overline{P}^m)_{inflow}} \,.$$

(4-5)

The boundary layer losses were estimated using an empirical relationship described by Cumpsty [2], which related entropy production in the boundary layer to the integral of the cube of the local freestream velocity, *i.e.*,

$$\text{mass flow-weighted total pressure loss} = C_D \int U^3 dA \,.$$

(4-6)

For turbulent boundary layers the dissipation coefficient, C_D, is not a strong function of Reynolds number and a value of 0.002 was taken as representative [2].

The shroud boundary layer loss was taken as the loss associated with the boundary layers on the upper and lower walls of the computational domain. In practice, this will differ from the actual loss as the shroud geometry will vary from the computational one. Further, the flow field near the shroud was dependent on the distance between the shroud and mixer. For this study, the upper and lower walls were one-half lobe wavelength from the peak of the mixer. Although the flow was not fully mixed out at the end of the computational domain, the loss coefficients for the ADM were over 90% of the fully mixed out values. As such, the estimates were representative of the actual losses. A constant area mixing process was employed to calculate the *fully mixed* out loss because, as noted above, those conditions were not attained at the computational outflow. The flow field at the lobe trailing edge was used as inflow conditions to a control volume and then mixed out to uniform flow.

4.3.1 Effect of Varying Velocity Ratio

The change in loss as the velocity ratio was varied was examined by carrying out computations on the ADM with a penetration angle of 22° and velocity ratios of 1.0 and 0.5 (cases C2 and C3). The trailing circulation was the same for both of these configurations. Referring to Figs. 4-5 and 4-6 the lobe and shroud boundary layer losses for the two cases were comparable (< 10% difference), but there was approximately three times more loss associated with mixing of the non-uniform velocity field for the ADM with r = 0.5. Referring to Fig. 4-5, the high velocity shroud boundary layer losses for the CP were approximately twenty times the low velocity shroud values (C1). For the CP the low and high velocity streams remained close to the shroud along the complete axial extent of the computational domain (see Fig. 3-2). For the ADM, in contrast, the mixing which occurred downstream of the trailing edge caused a redistribution of the flow field. This resulted in the velocities near the shrouds being more closely matched (see Fig. 3-3), so the low and high velocity shroud boundary layer losses were comparable (< 10% difference).

83

With a velocity ratio of unity, the computations showed that the contribution of the boundary layer and mixing losses to the total loss were within 20% of each other. The shroud boundary layer loss was approximately four times the lobe boundary layer loss, primarily reflecting the difference in surface area between the lobe and shroud. For a velocity ratio of 0.5 however, mixing losses accounted for more than 80% of the total loss. Since lobed mixers are frequently used to mix fluids having velocity ratios in the range of 0.5 to 0.3, mixing losses downstream of the lobe trailing edge will typically be the largest contribution to the total loss.

4.3.2 Effect of Varying Penetration Angle

Fig. 4-5 shows the results for lobe penetration angles of 22°, 30°, 35° and 45°. Increasing the lobe penetration angle caused an increase in the boundary layer losses because of the higher local velocities due to increased streamline curvature; as Equation (4-6) shows, the boundary layer losses scaled with the *cube* of the freestream velocity.

The mixing loss increased with the penetration angle at over twice the rate of the boundary layer loss (Fig. 4-7). For $\alpha = 22°$ (C3) the mixing loss coefficient, denoted $[C_{Pt}]_m$, was approximately 0.43, increasing to 0.74 for $\alpha = 45°$ (C6). As the penetration angle was initially increased, a larger portion of the fluid kinetic energy at the lobe trailing edge was associated with transverse velocities, and most of this was lost in the mixing process. This accounted for most of the mixing loss for the ADM with r = 1.0 and thin boundary layers ($\alpha_{eff} \approx \alpha = 22°$). This swirl component of kinetic energy can be shown to scale with $\sin^2\alpha_{eff}$, and this was reflected in the loss coefficient for this case where 80% of the mixing loss was from the swirl. For the ADM with r = 0.5, a large contribution to the mixing loss came from the mixing out of the non-uniform streamwise velocities. As the penetration angle was increased past 30°, boundary layer blockage and separation were responsible for the increase in mixing loss as the effective lobe penetration angles (26°, 26.5°, 25°) varied

little for penetration angles of 30°, 35° and 45°. This trend showed that there was no benefit in increasing the penetration angle past 30° as the loss increased but the effective angle (and therefore the shed streamwise circulation) did not.

4.3.3 Relationship between Total Pressure Loss and Thrust Loss

The thrust coefficient, C_T, was defined in Chapter 3 as the momentum flux of the co-flowing streams if mixed out to a static pressure equal to the inflow static pressure, normalized by the momentum flux of the unmixed streams at the inflow (Eq. 3-5). Fig. 4-8 shows the thrust coefficient and total loss coefficient, denoted $[C_{P_t}]_T$ (boundary layer + mixing losses), vs. mixer configuration. The figure illustrated the following points:

1) Over the range of mixers tested the thrust coefficient dropped 8%, from 0.888 to 0.818. For the ADM configurations, a trend of reduced thrust coefficient with increasing penetration angle was evident. This occurred because of the larger non-streamwise component of momentum at the trailing edge and boundary layer blockage as the penetration angle was increased.

2) The thrust coefficients were the highest for the CP and ADM with $\alpha = 22°$. The CP, despite having parallel flow at its trailing edge, had the same thrust coefficient as the ADM with $\alpha = 22°$ because of the additional drag over its extension, which quadrupled the mixer's wetted area. As such, the convoluted plate presented no advantage over lobed mixers. It required an increased mixing length (as evident from comparing Figs. 3-2 and 3-3) but did not provide more thrust.

85

4.4 Summary

NEWT was used to give insight into the impact of viscous effects on mixer performance. Lobe geometries were examined with different penetration angles ranging from 22° to 45°. Flow separation first occurred at a penetration angle of 35°. There was no benefit, in terms of trailing streamwise circulation, of increasing the penetration angle above 30° because of increased boundary layer blockage and separation. As the lobe penetration angle was increased the trailing circulation deviated from a simple one-dimensional description [29] because of increased boundary layer blockage and eventually separation. These effects reduced the effective lobe penetration angle and height. Extending the one-dimensional model using an effective penetration angle and height gave values that agreed with the computed ones to within 5%. As such, the shed trailing edge circulation was a function of only the lobe geometry and boundary layer displacement thickness.

The performance of the lobed mixer, in terms of the magnitude of the shed circulation, was dependent on the characteristics of the inlet boundary layer. A thick inlet boundary layer lead to filling of the lobe trough with low momentum fluid, resulting in a reduced lobe effective angle and hence reduced streamwise circulation, compared to a configuration with a thin inlet boundary layer. Again, the behavior was quantified using an effective lobe angle and height.

For a velocity ratio of unity, boundary layer and mixing losses were comparable, but for realistic velocity ratios (0.5 or less) the mixing losses were the dominant loss source, accounting for approximately 80% of the total loss. For fixed velocity ratio, as the lobe penetration angle was increased the loss increased, resulting in a reduction of thrust. Given that the streamwise circulation did not increase for penetration angles above 30°, there was no advantage in exceeding this angle.
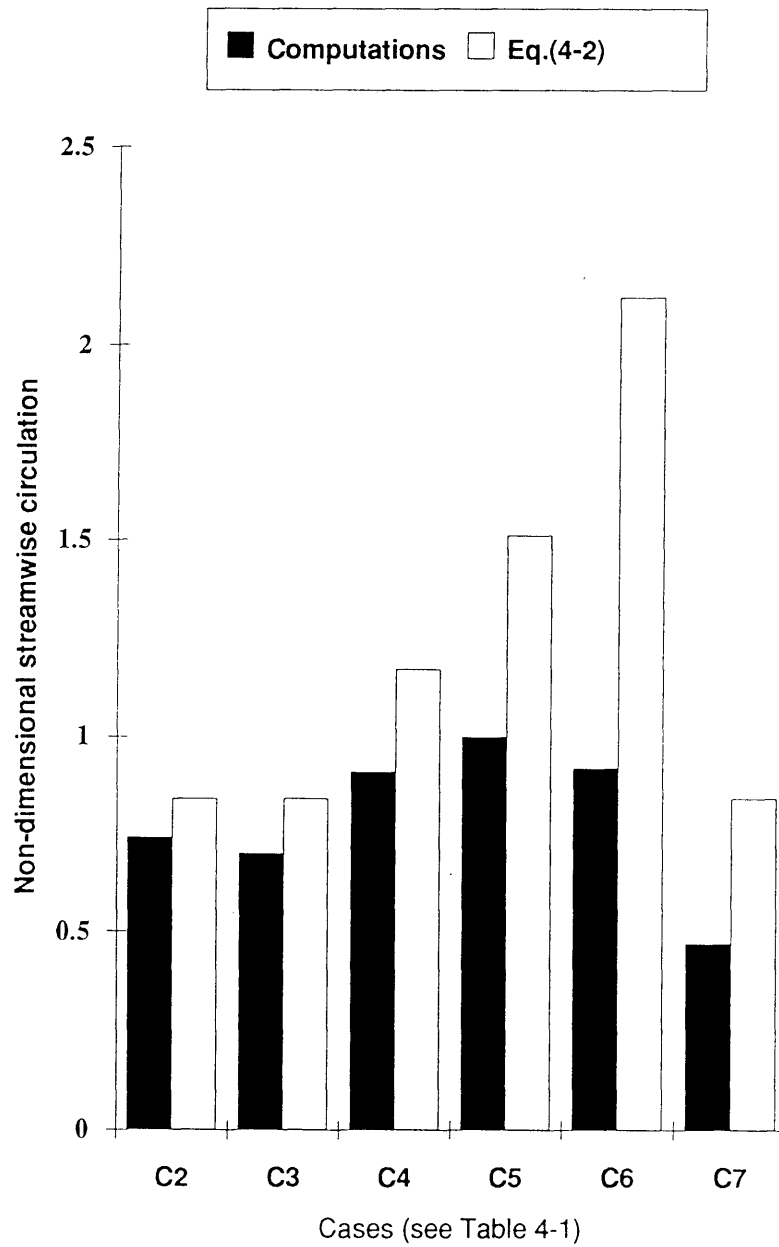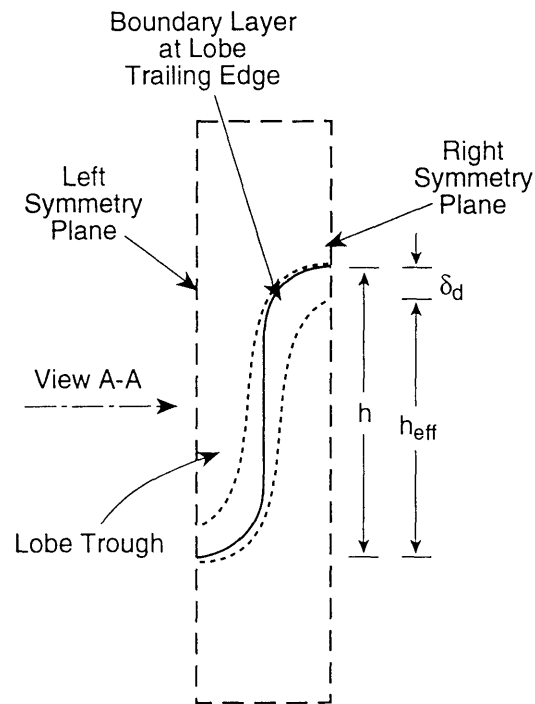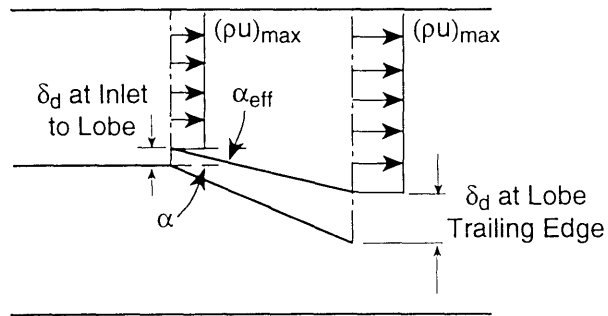
Figure 4-1   Streamwise circulation, Γ_{sw}^{*}, based on penetration angle, α

Boundary Layer
at Lobe
Trailing Edge

Left
Symmetry
Plane

Right
Symmetry
Plane

δ_d

View A-A

h

h_{eff}

Lobe Trough

**(a) Schematic of Boundary Layer Profile
at the Lobe Trailing Edge**

$(\rho u)_{max}$ $(\rho u)_{max}$

δ_d at Inlet
to Lobe

α_{eff}

α

δ_d at Lobe
Trailing Edge

(b) View A-A

Figure 4-2   **Boundary layer blockage and definition of lobe
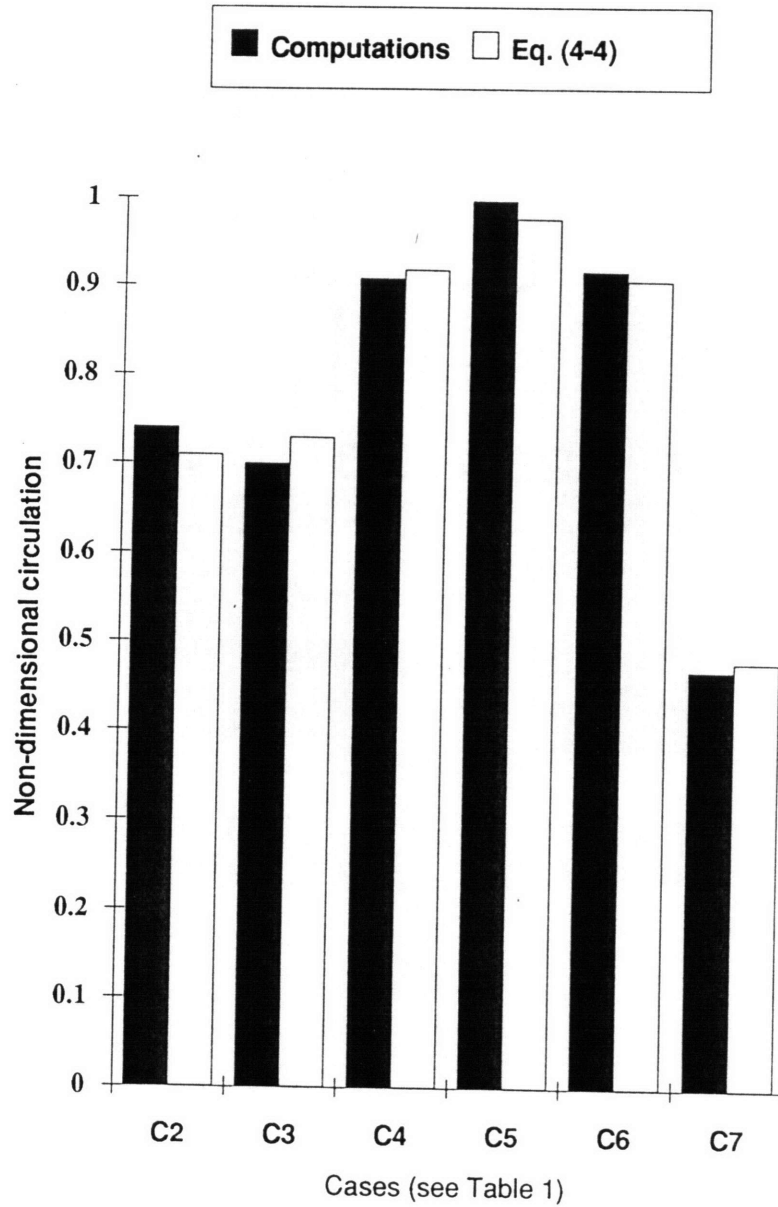effective angle and height, α_{eff}, h_{eff}**

88

Figure 4-3   Streamwise circulation, Γ^*_{sw}, based on effective angle and height, α_{eff}, h_{eff}

$\delta_d/\lambda = 0.01$
at the lobe inlet

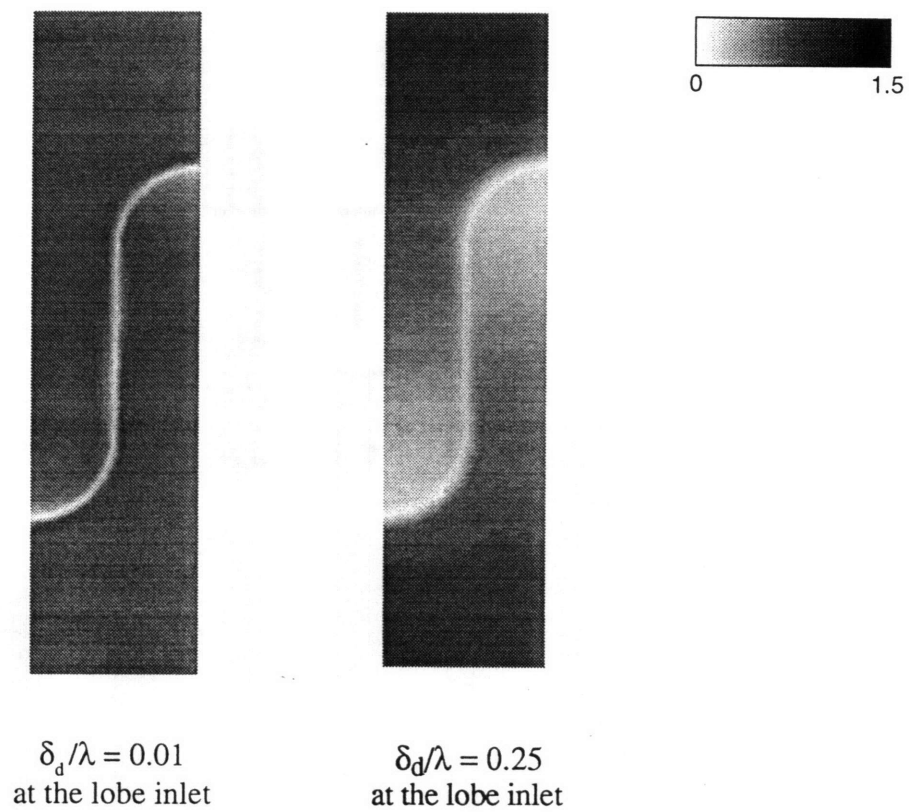$\delta_d/\lambda = 0.25$
at the lobe inlet

Figure 4-4   **Mach number at the lobe trailing edge for**
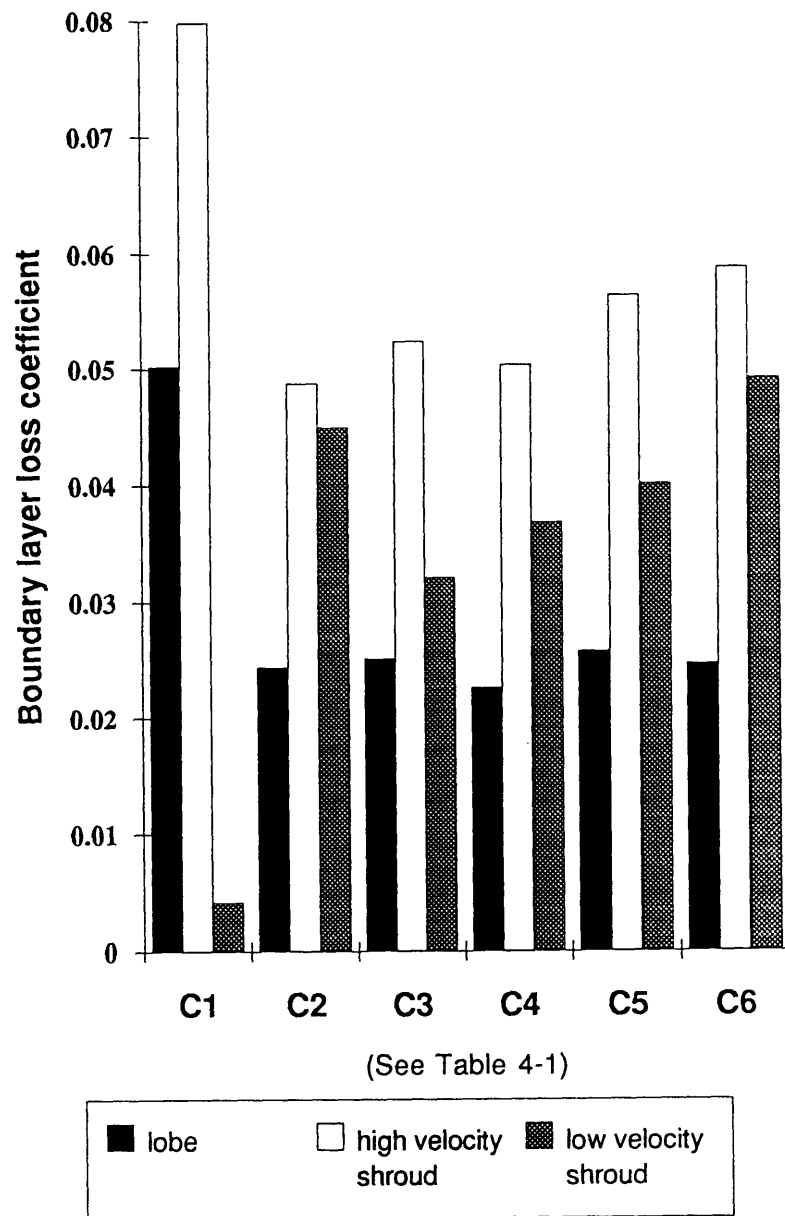**$\delta_d/\lambda = 0.01$ and $\delta_d/\lambda = 0.25$ at the inlet ($r = 1.0$)**

Figure 4-5   Boundary layer loss coefficient, $[C_{Pt}]_{bl}$

Figure 4-6   **Mixing loss coefficient, $[C_{Pt}]_m$**

0.9

0.8

0.7

0.6

Loss Coefficient

0.5

0.4

0.3

0.2

0.1

0

C1   C2   C3   C4   C5   C6

(See Table 4-1)

■ mixing loss coeff. [CPt]m   □ boundary layer loss coeff. [CPt]bl
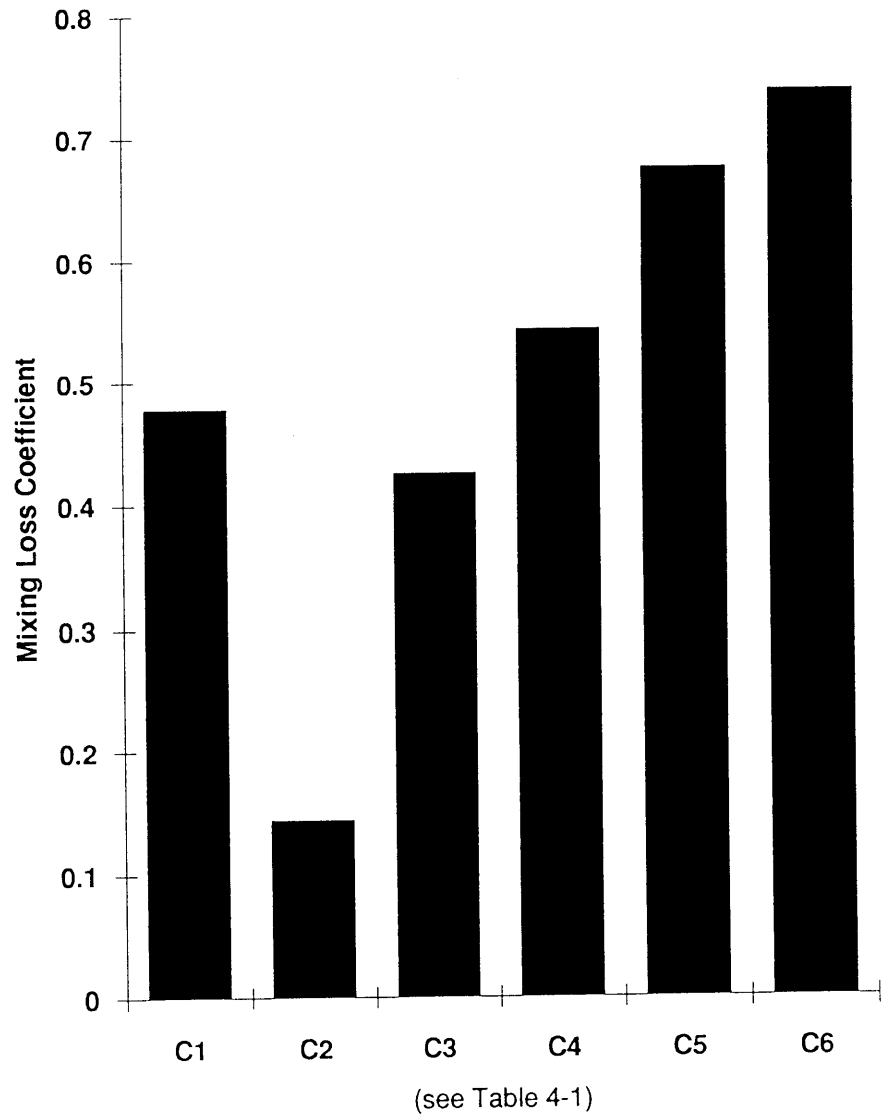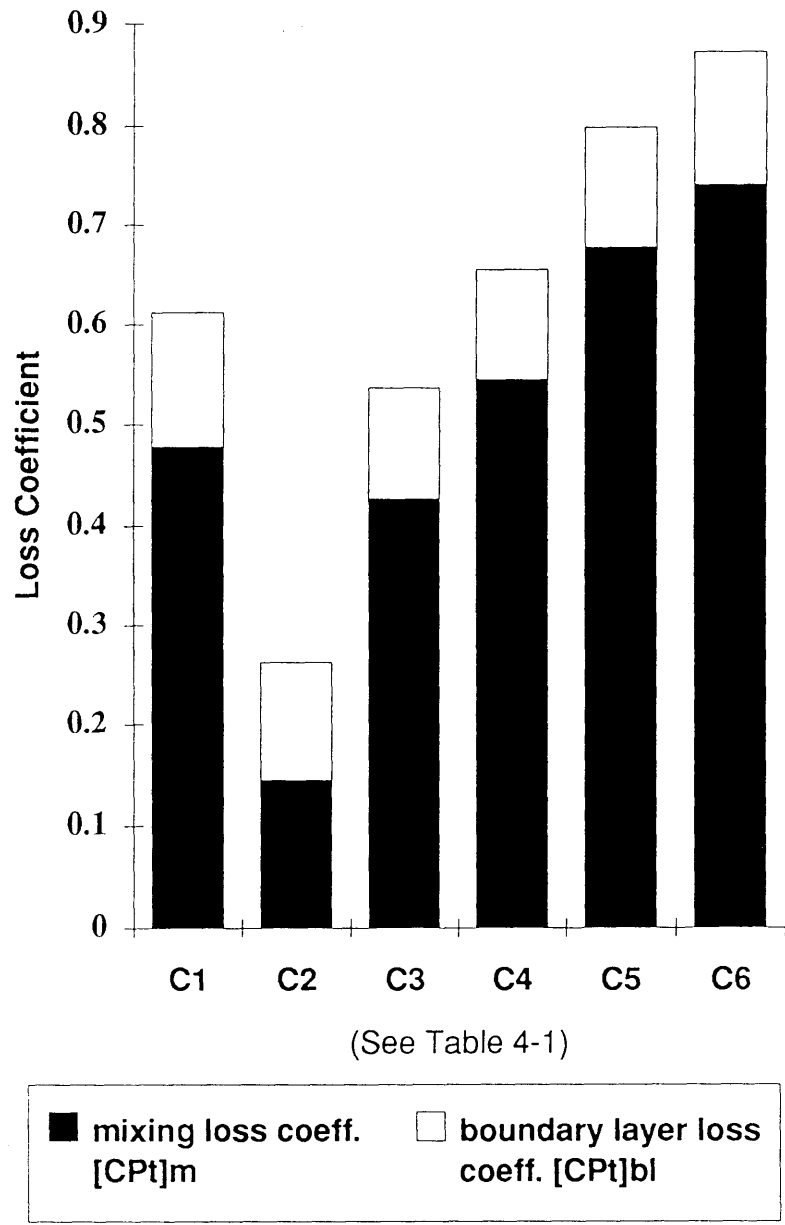
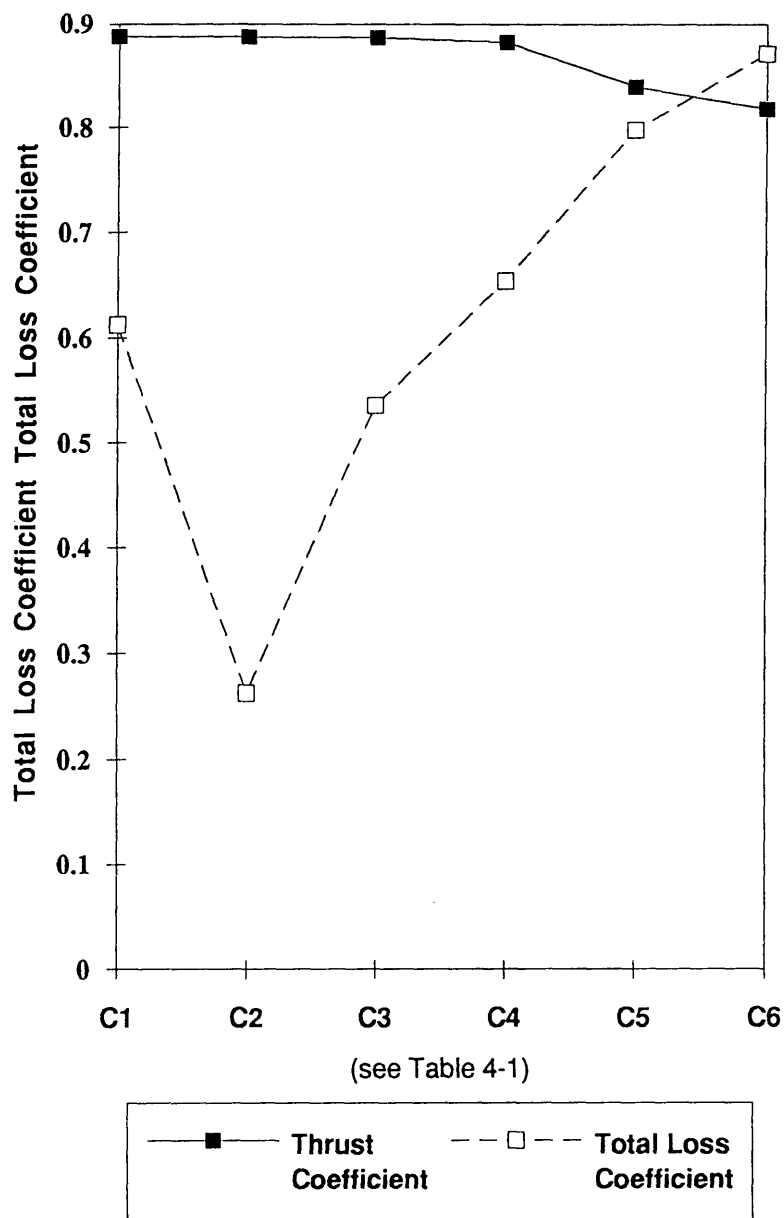Figure 4-7   Contributions to the total loss coefficient, $[C_{Pt}]_T$

Figure 4-8 Total loss coefficient, $[C_{Pt}]_T$, and thrust coefficient, C_T

Chapter 5

The Two Dimensional Slender-Body Approximation and Comparison to Three Dimensional Results

The spatial development of the three-dimensional steady flow field downstream of a lobed

mixer can be modeled as an unsteady two-dimensional flow as illustrated in Fig. 5-1. The

cross-flow plane was considered to convect downstream at the mean axial velocity U with

the axial distance being given by U·t. By decoupling the axial and cross-flow in this

manner the analysis of the flow is significantly simplified.

5.1 The Slender-body Approximation

The general argument for using this analogy is based on the mixing length scales [34].

Mixing by diffusion occurred over the thickness of the shear layer, which was initially very

thin. In contrast, the streamwise circulations were on the order of the lobe height. Thus,

for the region in which the streamwise vorticity was the dominant mixing mechanism, the

gradients in the cross-flow plane were larger than those axially, and the approximation

held.

Fung quantified the conditions for the validity of the slender-body approach through non-

dimensional analysis of the governing Reynolds-averaged Navier-Stokes equations [11].

They were,

$$(i) \qquad \frac{\Delta U}{\overline{U}} << 1$$

$$\text{(ii)} \quad \frac{\Delta U}{\overline{U}} \ll \Gamma^{*2}$$

$$\text{(iii)} \quad \Gamma^{*2} \ll 1 \qquad\qquad\qquad\qquad\qquad (5\text{-}1)$$

These conditions ensured that the cross-flow planes were decoupled with respect to convection, pressure forces and diffusion, respectively. Flows of practical interest, however, are outside these limits with $\Delta U / \overline{U}$ of 0 to 0.7 and Γ^{*} from 0.5 to 1.5. However, results from Qiu's slender-body code have compared well with experiments for these conditions. Specifically, the pressure recovery is shown in Fig. 5-2 for $\Delta U / \overline{U} \approx$ 1.5 [27]. The slender-body code has also compared well for cases where the non-dimensional circulation was on the order of unity [34]. It was evident from these results that the above restrictions did not accurately represent the limits of the slender-body approximation. As such, a numerical investigation was performed to determine the conditions for which the model was still valid, thereby extending its use for practical flows.

5.2 Implementation of the Slender-body Code

The slender-body code was a two-dimensional unsteady spectral-method Navier-Stokes solver. The inputs into the code were non-dimensionalized by the lobe wavelength and trailing edge streamwise circulation. In the initial vorticity distribution, the vorticity was constant along a specified trailing edge and had an error-function profile across the input thickness. Alternatively, this distribution could be read in from an external file.

The downstream distance was represented by the non-dimensional time, t*, defined as,

$$t^{*} = \frac{\Gamma}{\overline{U}\lambda} \cdot \frac{x}{\lambda}. \qquad\qquad\qquad\qquad (5\text{-}2)$$

The turbulence model was based on Prandtl's second hypothesis for planar shear layers as outlined in Section 3.2.5. A primary advantage of using this model was that it did not

require information from other cross-flow planes. The planes were therefore computationally decoupled, thereby simplifying the code considerably.

The slender-body code was relatively fast compared to full viscous Navier-Stokes simulations: it required approximately 4-8 hours for a solution compared to 40-80 hours on an IBM RS6000 workstation.

5.3 Comparisons of Two-Dimensional Slender-body and Three-Dimensional Computations

The slender-body code started with an initial specified streamwise vorticity distribution and simulated the downstream evolution of the flow field. The objective of the comparisons was to determine the conditions for which the three-dimensional terms neglected by the slender-body approximation became significant. Therefore, all the other terms in the equations being solved by the two codes had to be matched, particularly the

(i)   initial conditions
(ii)   turbulent viscosity.

The first was accomplished by interpolating the vorticity distribution from the three-dimensional solution at 0.05 wavelengths past the trailing edge to the slender-body grid. As Fig. 5-3 shows for the case of S1 (see Table 5-1 below) this interpolation was performed accurately.

To match the turbulent viscosity, the shear layer turbulence model from the slender-body code was applied in NEWT past the trailing edge. As shown in Section 3.2.5, this had negligible effect on the calculated circulation. NEWT also had numerical smoothing that effectively changed the viscosity, while the slender-body code only included a constant to supplement the planar shear layer viscosity (the Reynolds number, Re_Γ, discussed in Section 3.2.5). As such, the viscosities could not be matched directly. However, the

circulation decay was a result of the vorticity diffusing out (to the symmetry boundaries) and canceling with adjacent vortices. Matching the decay rate therefore matched the diffusivities, since the streamwise vorticity was of a similar form spatially for the two computations. The decays were matched by varying the Reynolds number in the slender-body code accordingly. For cases with a velocity difference between the streams (S2, S3), the relative contribution of the constant Re_Γ viscosity (see Eq. 3-11) dropped rapidly from $t^* = 0$: for $r=0.7$, the turbulent viscosity from the shear-layer model was an order of magnitude larger than the Re_Γ term by $t^*=0.5$. However, for matched velocity ratios ($r \rightarrow 1$ in Eq. 3-10, Eq. 3-11) it was the dominant term, providing numerical stability.

The height of the lobes was one wavelength, which is typical of ADM designs. The penetration angle was $22°$ and the trailing edge profile is shown in Fig. 5-4. This geometry provided a test of the slender-body analogy as Γ^* was on the order of one (according to Eq. 4-4). It was also amenable to the slender-body solver. In the investigations the effect of the velocity and density ratios was examined, with the latter being obtained by varying the static temperature of the streams. The test matrix is given below.

Table 5-1
Test matrix for the two-dimensional slender-body -
three-dimensional comparisons

CASE	$\overline{U}$ (m/s)	Velocity Ratio (r)	Density Ratio (s)	Γ^*	$\dfrac{\Delta U}{\overline{U}}$
S1	186	0.99	0.99	0.94	0
S2	163	0.73	0.97	0.93	0.31
S3	178	0.62	0.94	0.89	0.47
S4	146	0.99	0.5	0.95	0

The integrated parameters that were compared included the mass-averaged and area-averaged scalar mixedness and the interface length between the two streams. These variables were indicative of mixing augmentation. The normalized mass-averaged scalar mixedness indicated the degree to which the flow reached the fully mixed-out state. The area-averaged mixedness was an integrated scalar measure of the visual passive scalar comparison. It was representative of the mixing that occurred up to the point where it was evaluated, without regard of the fully mixed-out state. As such, it was not normalized to 1 in order to preserve different mixed-out states. The interface length could not be evaluated past $t^* \approx 3$ because of insufficient numerical resolution in the three-dimensional solution. Visual plots of the passive scalar and streamwise vorticity were also examined, with the visual scalar plots being indicative of the area-averaged scalar mixedness. In general, the vorticity plots were of marginal utility because of numerical errors in both solutions. The NEWT plots had imprints of the grid and the slender-body code had poor resolution once the circulation decayed significantly.

5.3.1 Effect of the Stream-to-Stream Velocity Ratio

Figs. 5-5, 5-10, 5-16 show the streamwise circulation decay for the three velocity ratios with a density ratio of approximately one. The downstream streamwise circulation of the slender-body and three-dimensional codes varied less than 9% for $t^* < 6$. However, as the velocity ratio was decreased, the slender-body circulation decayed faster than the three-dimensional circulation in the far downstream region. This was not expected to influence the results because most of the mixing had occurred before this larger deviation (no less than 80% of the final scalar mixedness).

For the case of r=1.0, the area and mass-averaged scalar mixednesses were the same and closely matched between the two calculations: the largest differences were 12% at $t^* \approx 4$ and 7% at the end of the computational domain. In addition, the differences in the scalar

mixedness were mirrored almost exactly by those in the streamwise circulation. The interface lengths (Fig. 5-7) differed by less than 10%. Visual plots of the passive scalar at t* = 0, 0.8, 1.4 and 3.0 are shown in Fig. 5-8. The plots for the two solutions matched very closely, with most of the difference being from the resolution of the different grids. The vorticity plots, Fig. 5-9, were not as useful because of deficiencies in the downstream three-dimensional grid. However, it was still evident that the two solutions had the same amount of turning and the formed an elliptical vortex core at approximately t*=3.0. The slender-body approximation was thus valid for $\Gamma^* \approx 1$.

The case of r=0.7 is shown in Figs. 5-10 to 5-15. The comparison was essentially similar to the one for matched velocities. The cusp in the interface length was not evident in the three-dimensional solution because the spacing between sampling planes was larger than the cusp's width. The three-dimensional mass-averaged scalar mixedness was approximately 20% greater than the slender-body scalar mixedness (Fig. 5-12). The area-averaged scalar mixedness corresponded to within 10% (Fig. 5-11), showing that the amount of mixing at the downstream planes was similar. The slender-body code was seen to apply for $\Delta U / \overline{U} \leq 0.3$.

The circulation decay was not as well matched for the case of r=0.6, particularly in the far region where the slender-body circulation decayed more rapidly. Fig. 5-19 shows the interface lengths matched very closely for the two cases. The area-averaged scalar mixednesses showed more deviation, having differences of up to 20%. The mass-averaged mixedness showed that the three-dimensional solution approached the fully mixed out state approximately 40% faster. This is consistent with the slender-body code neglecting the mixing from the spanwise vorticity. In addition, the normalized mass-averaged mixedness was expected to reach the mixed-out state faster for unequal mass flow rates. Given the same interface length and diffusion rates, the flow will mix out faster the

more one stream dominates the other. The passive scalar plots of the slender-body and three-dimensional solutions, Fig. 5-20, showed marginal agreement and there were noticeable differences. The vorticity plots (Fig. 5-21) showed more differences than with r=0.7, although the general trends of the rotation rate and vortex core formation still matched. It was seen that the slender-body approximation began to break down for r=0.6. The general behavior of the flow was still captured, but except for the interface length, the slender-body approximation was no longer quantitatively valid.

5.3.2 Effect of the Stream-to-Stream Density Ratio

Fig. 5-22 shows the slender-body and three-dimensional streamwise circulation decays for a density ratio of 0.5 and velocity ratio of one. Fig. 5-25 shows that the interface lengths matched very closely, except for the cusp which was not captured because of the sampling plane frequency. The mass-averaged mixedness (Fig. 5-24) showed that the three-dimensional solution mixed-out approximately 15-20% faster. The area-averaged scalar mixednesses (Fig. 5-23) matched for t*<4, after which the three-dimensional solution was almost fully mixed (see the mass-averaged mixedness), but the two-dimensional solution was not and therefore continued to mix. The visual plots of the passive scalar (Fig. 5-26) corresponded well, while the vorticity plots suffered from the same resolution problems (Fig. 5-27). The validity of the slender-body approximation was marginal for a density ratio of 0.5.

5.3.2 Overview of Comparisons

Fig. 5-29 shows the variation in the three-dimensional mass-averaged mixednesses for the examined cases, which was on the order of 30%. However, for the slender-body approximation, the mixednesses were all within 5%. As the velocity and density ratio were varied, the slender-body solution changed little. Therefore, further studies of the

applicability of the slender-body theory only need to focus on the three-dimensional solutions.

5.4 Summary

The interface lengths matched closely for all the cases, even if there were visible differences in the passive scalar fields. The slender-body captured qualitative aspects of the flow fields for all the examined cases. Quantitatively, the approximation was valid for $\Gamma^* \leq 1$ and $\Delta U / \overline{U} \leq 0.3$. It was inaccurate for larger $\Delta U / \overline{U}$ and marginal for a density ratio of 0.5. Further investigations should be performed to find the maximum Γ^* and density ratio for which the approximation is valid.
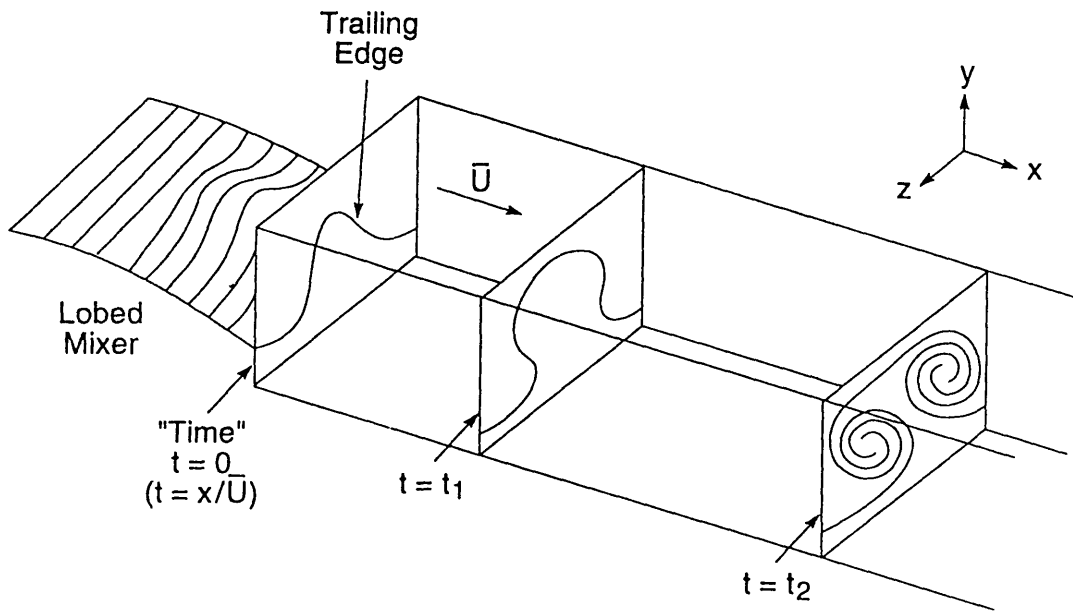
Figure 5-1   Two-dimensional slender-body analogy of a three-
dimensional spatially developing flow   [27]
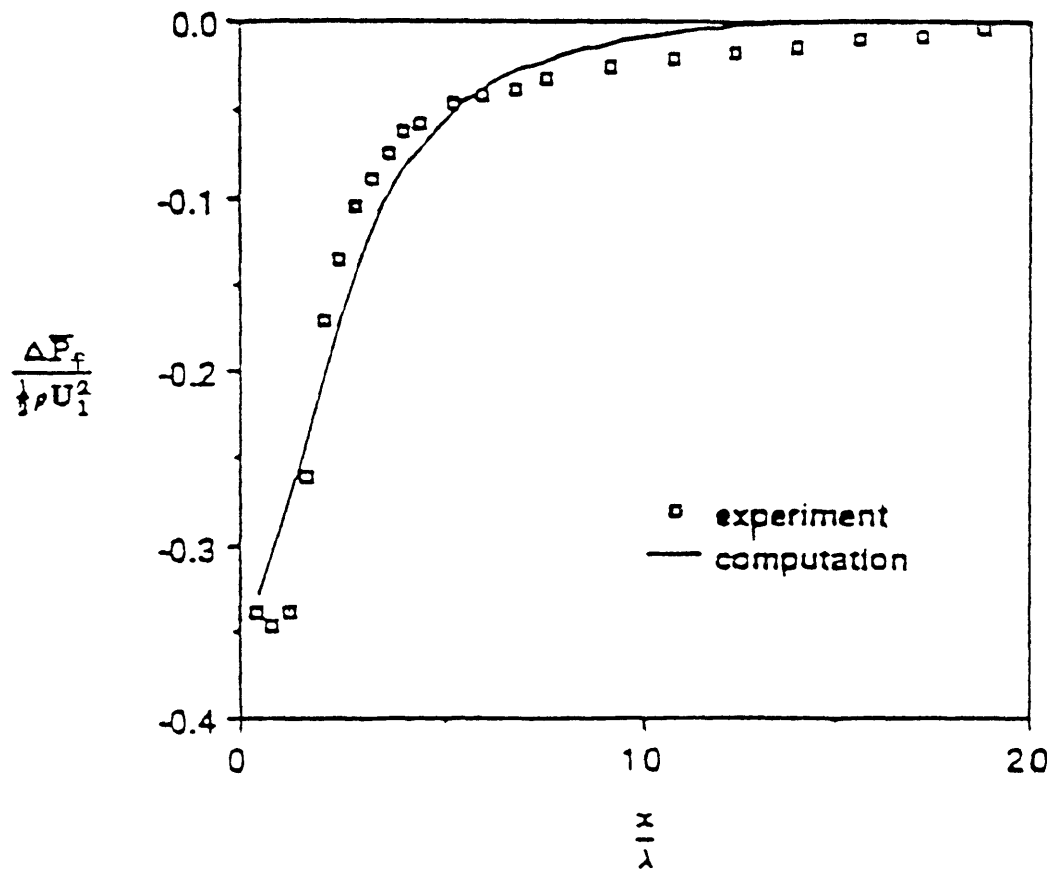
Figure 5-2   Comparison of ideal static pressure recovery
downstream of a lobed mixer -slender-body theory
versus experiments, $\Delta U / \overline{U} \approx 1.5$ [27]

Streamwise vorticity / $\overline{U}\lambda$

0 ▓▓▓▓▓ 25
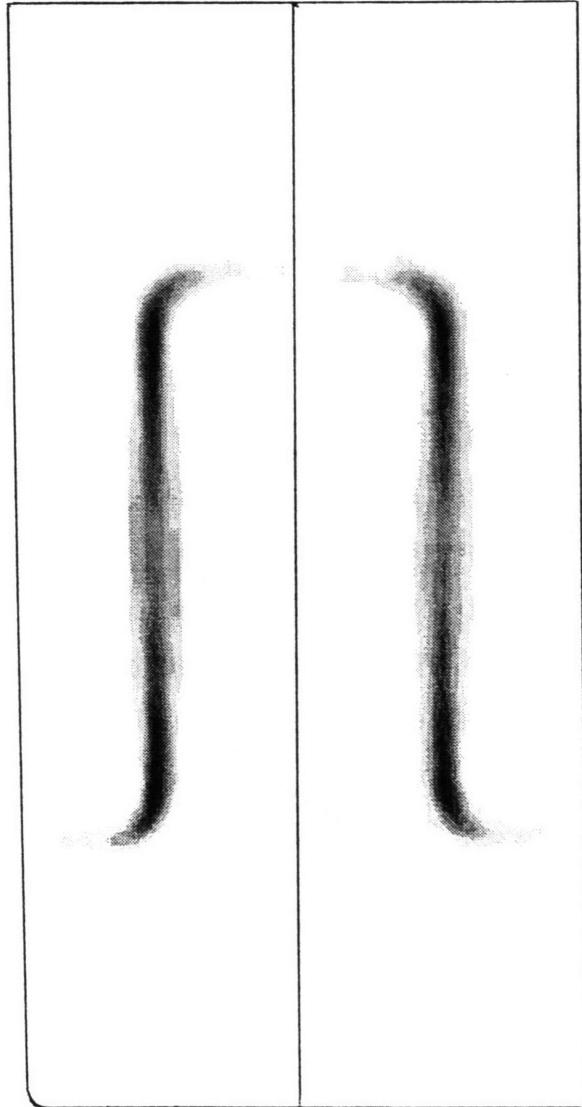
Figure 5-3   Interpolation of trailing edge vorticity from 3D unstructured grid to spectral solver

105
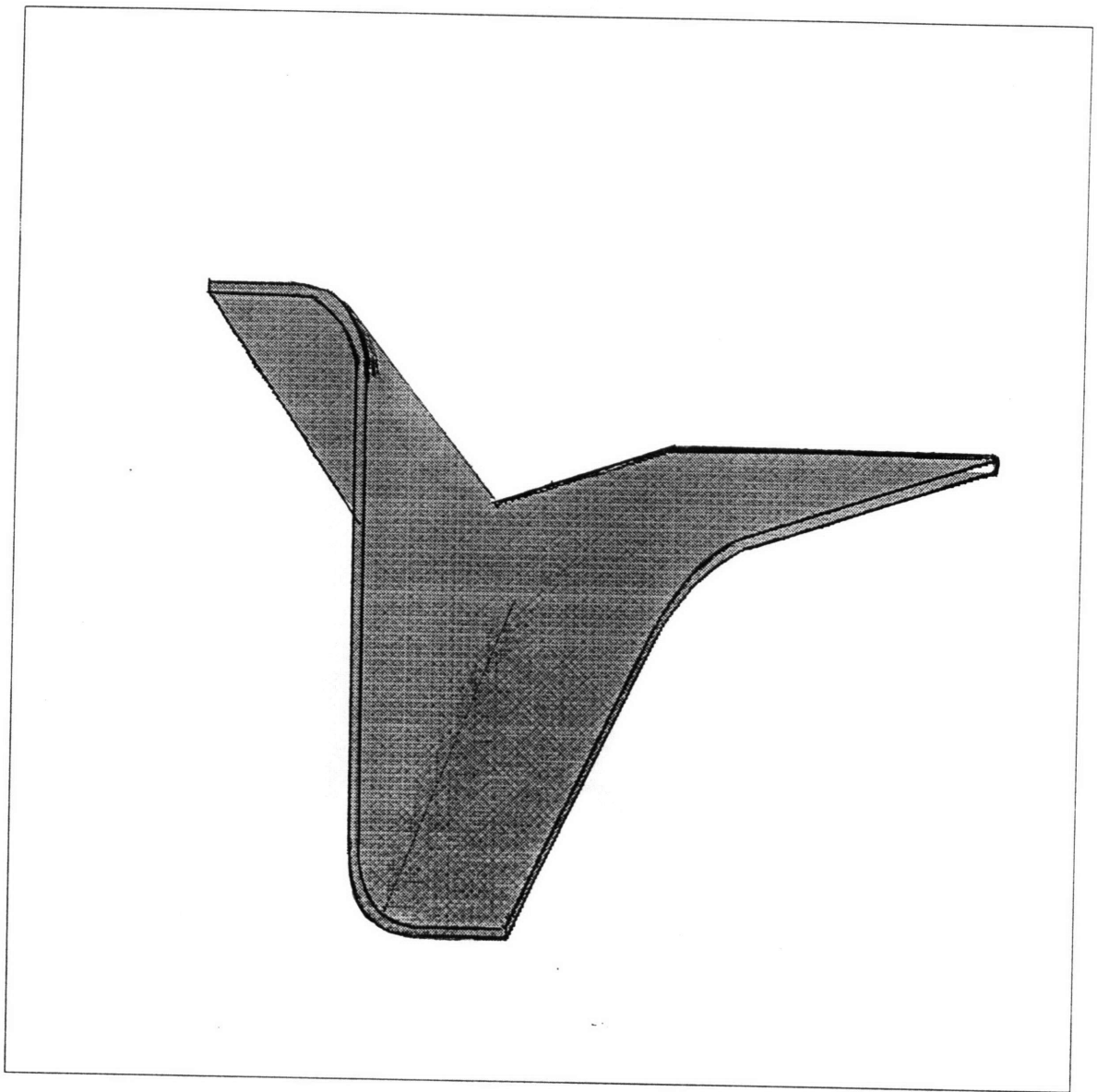
Figure 5-4

Trailing edge geometry of mixer for slender-body - three-dimensional comparisons
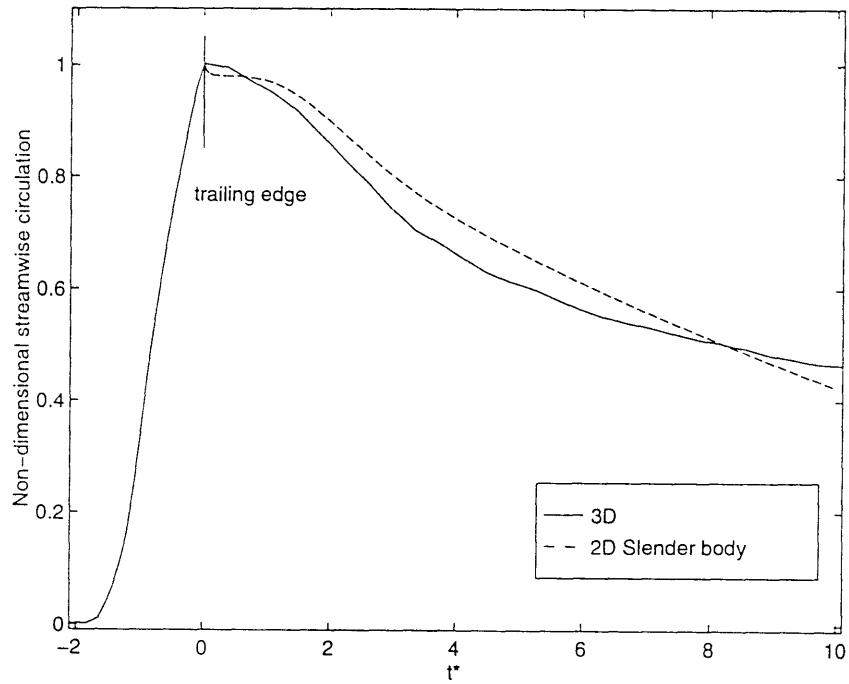
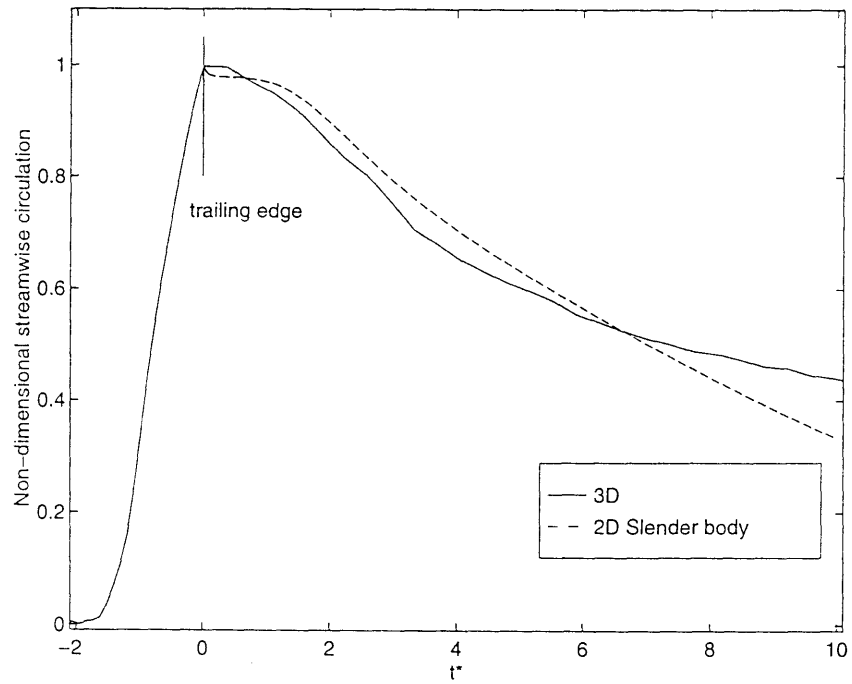**Figure 5-5**   Comparison of 3D and slender-body streamwise circulation decay   (r=1.0, s=1.0)
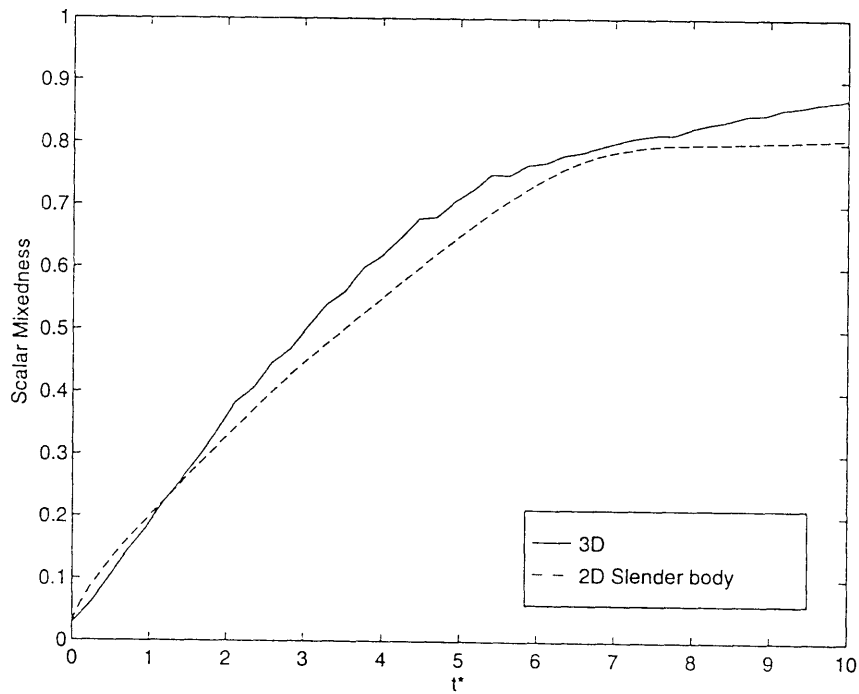
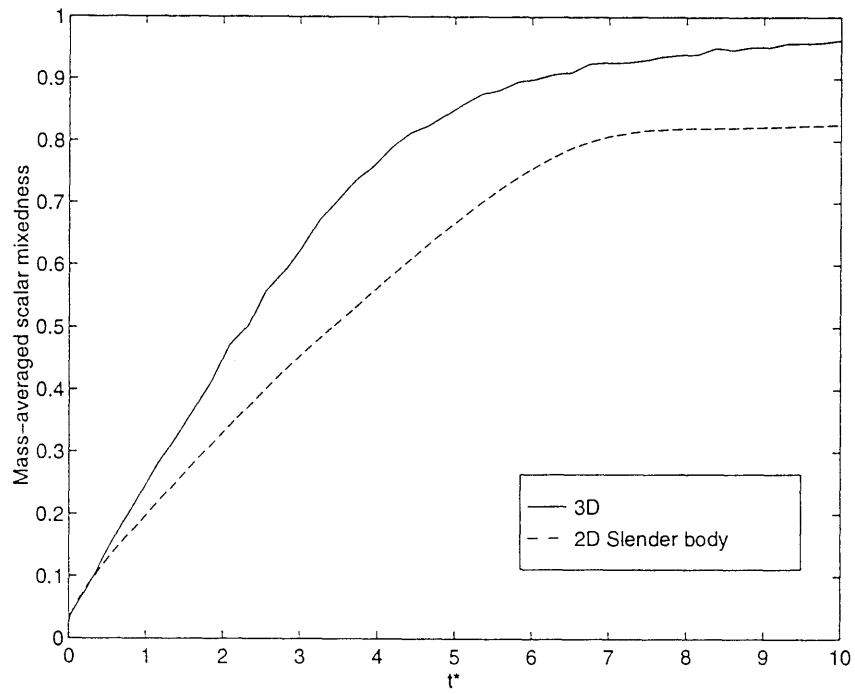**Figure 5-6**   Comparison of 3D and slender-body scalar mixedness (r=1.0, s=1.0)
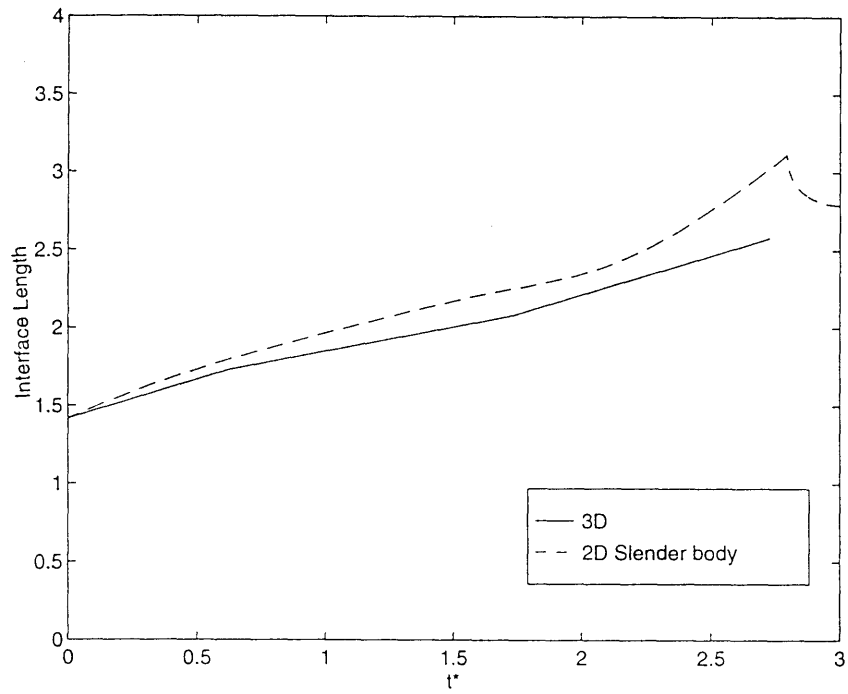
Figure 5-7   Comparison of 3D and slender-body interface length
(r=1.0, s=1.0)

3D   Slender
            body

t*=0   t*=0.8

t*=1.4   t*=3.0
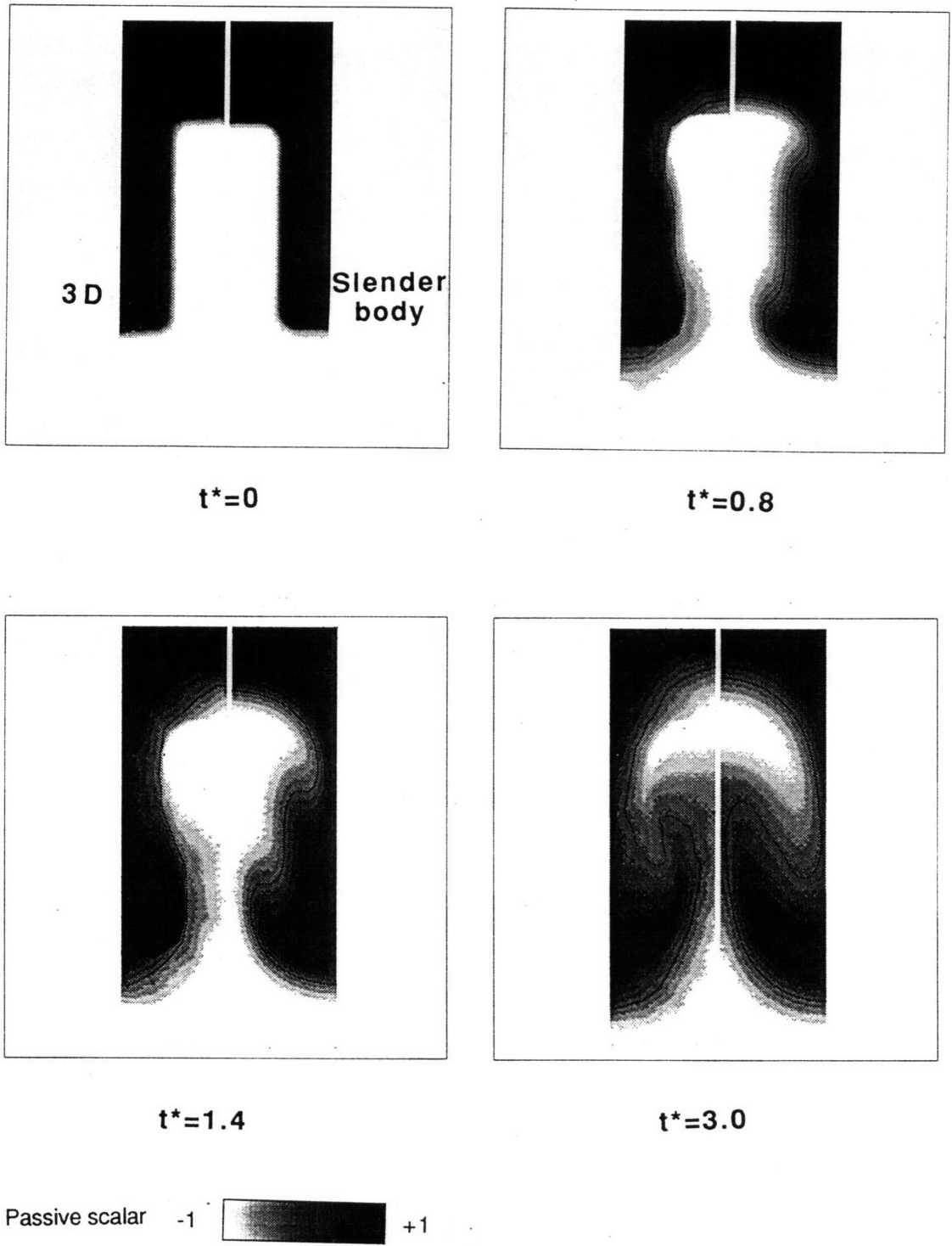
Passive scalar   -1 [ ] +1

Figure 5-8   Comparison of 3D **and slender** body passive scalar
                   distribution at t*= 0, 0.8, 1.4, 3.0   (r=1.0, s=1.0)

109

3 D   Slender
                        body

t*=0   t*=0.8

t*=1.4   t*=3.0

Streamwise vorticity / $\overline{U}\lambda$ 0 ▭ 25
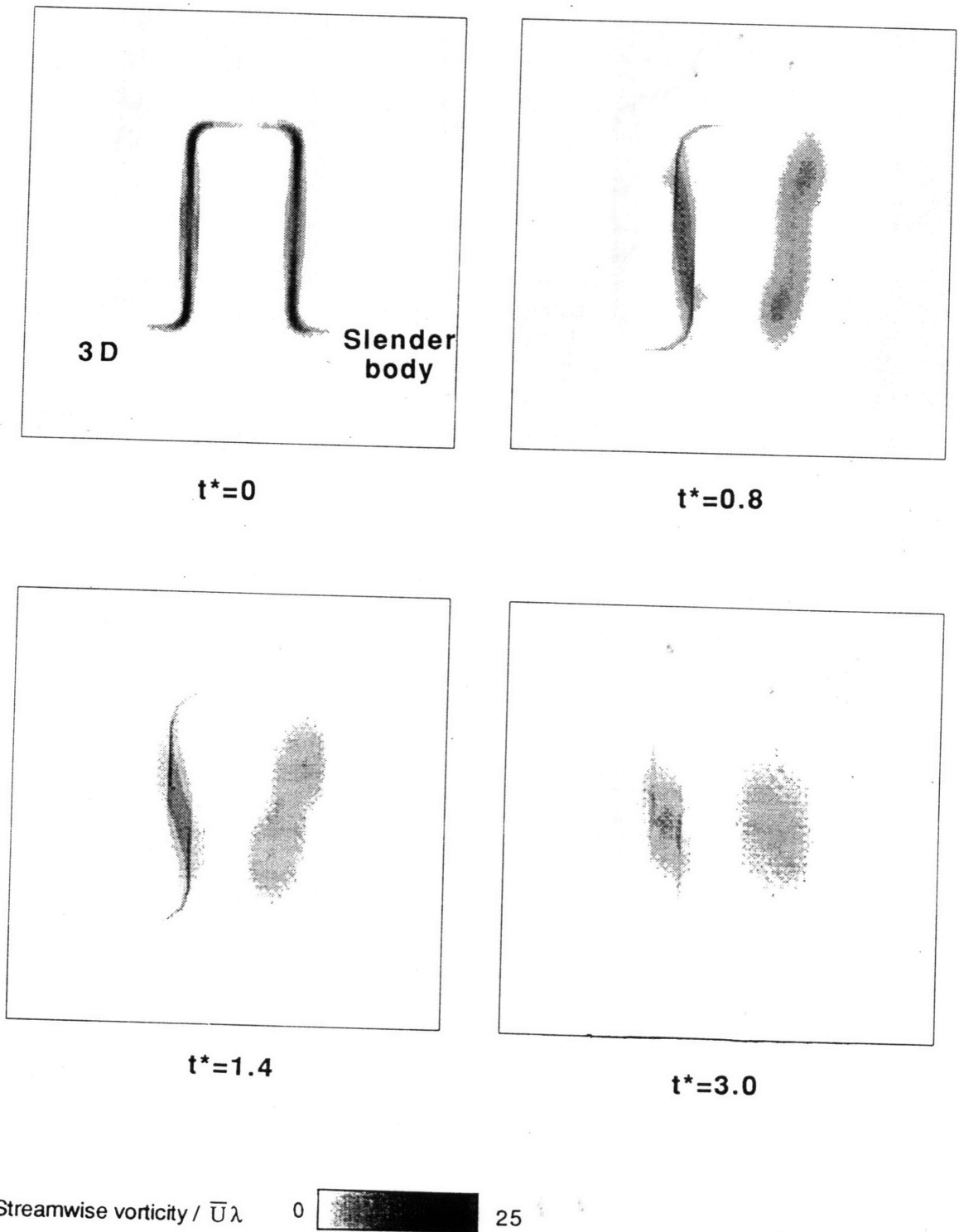
Figure 5-9   Comparison of 3D and slender body streamwise
                    vorticity distribution at t*= 0, 0.8, 1.4, 3.0
                    (r=1.0, s=1.0)

Figure 5-10   Comparison of 3D and slender-body streamwise circulation decay (r=0.7, s=1.0)
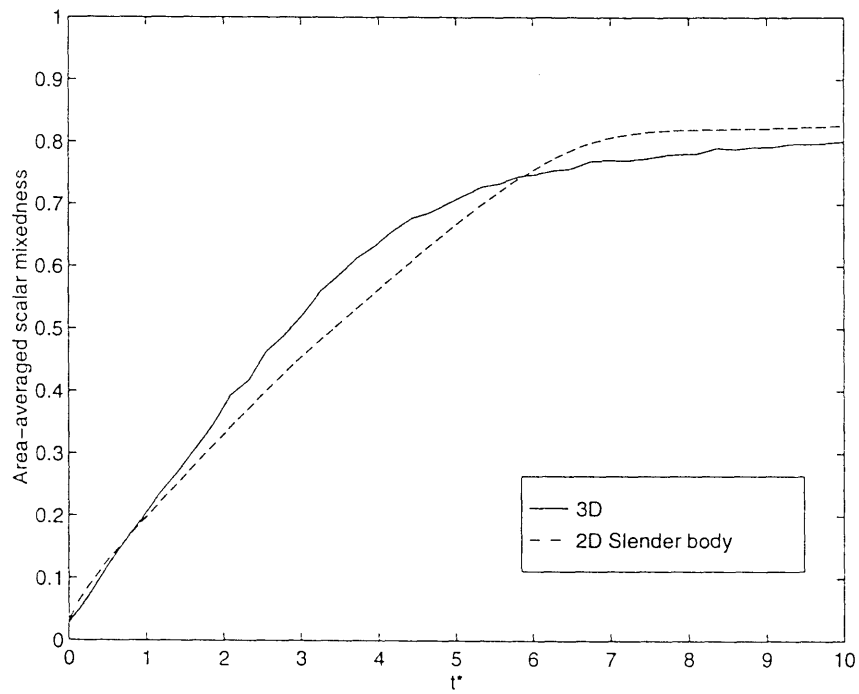
Figure 5-11   Comparison of 3D and slender-body area-averaged scalar mixedness (r=0.7, s=1.0)

111

Figure 5-12   Comparison of 3D and slender-body mass-averaged scalar mixedness (r=0.7, s=1.0)
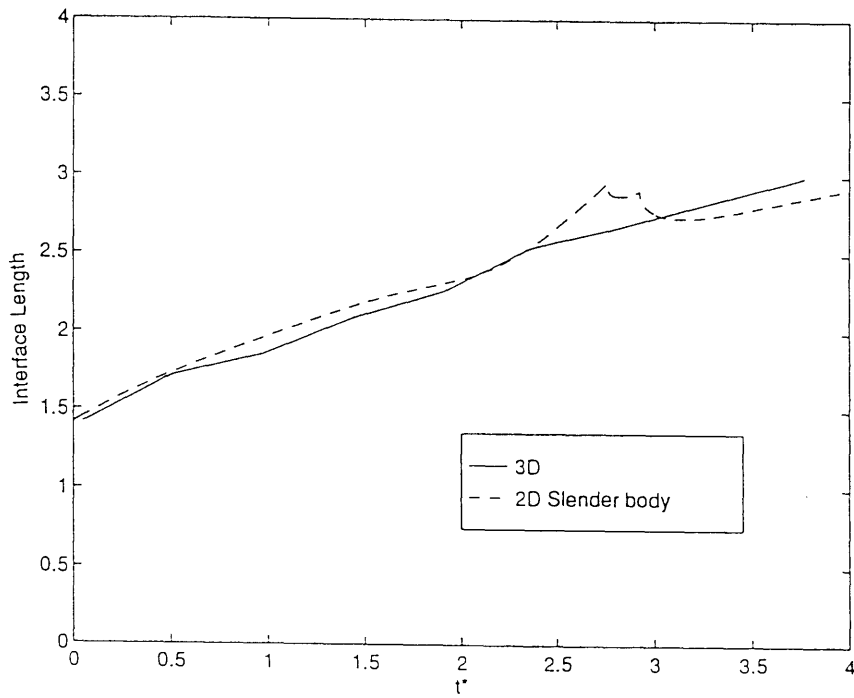
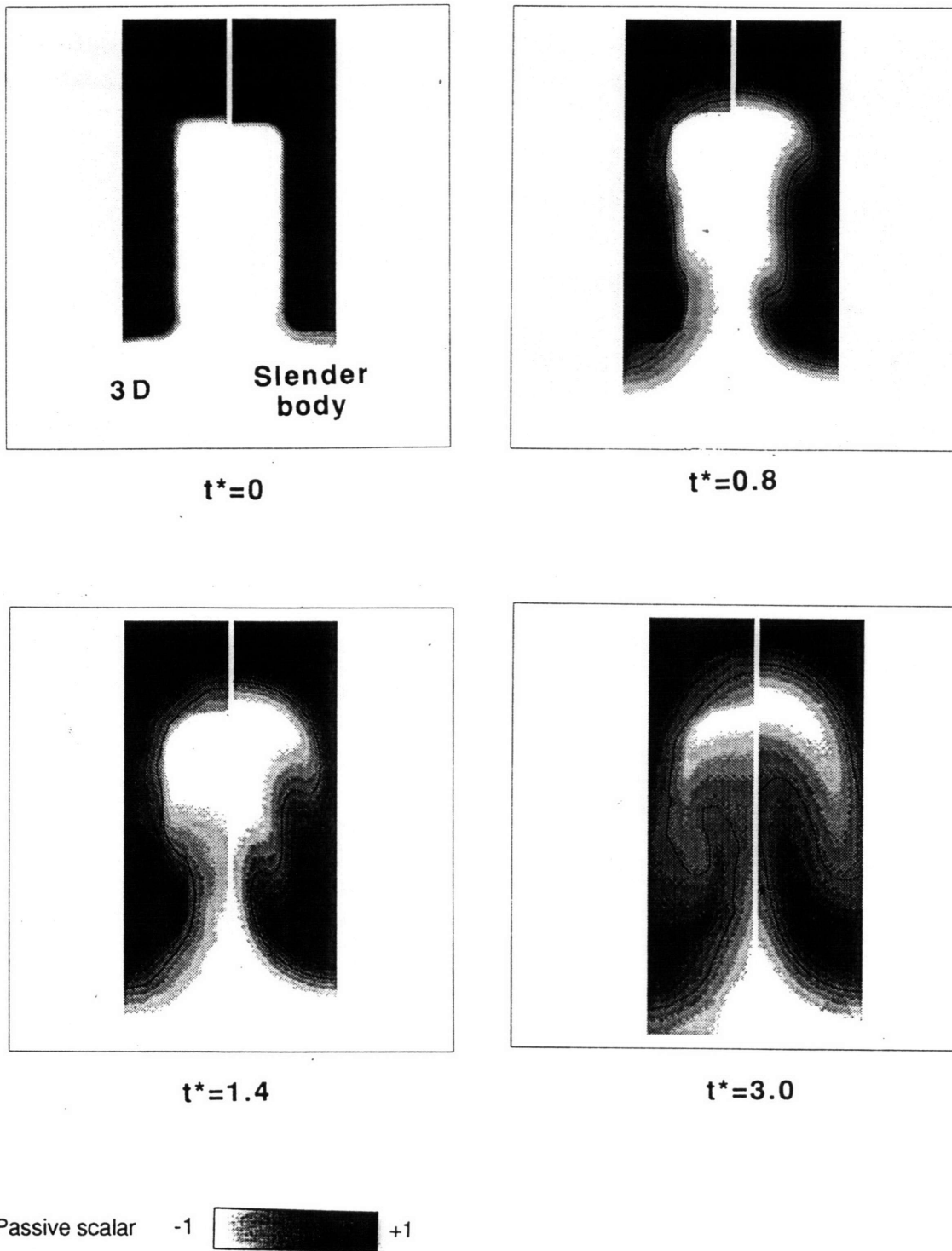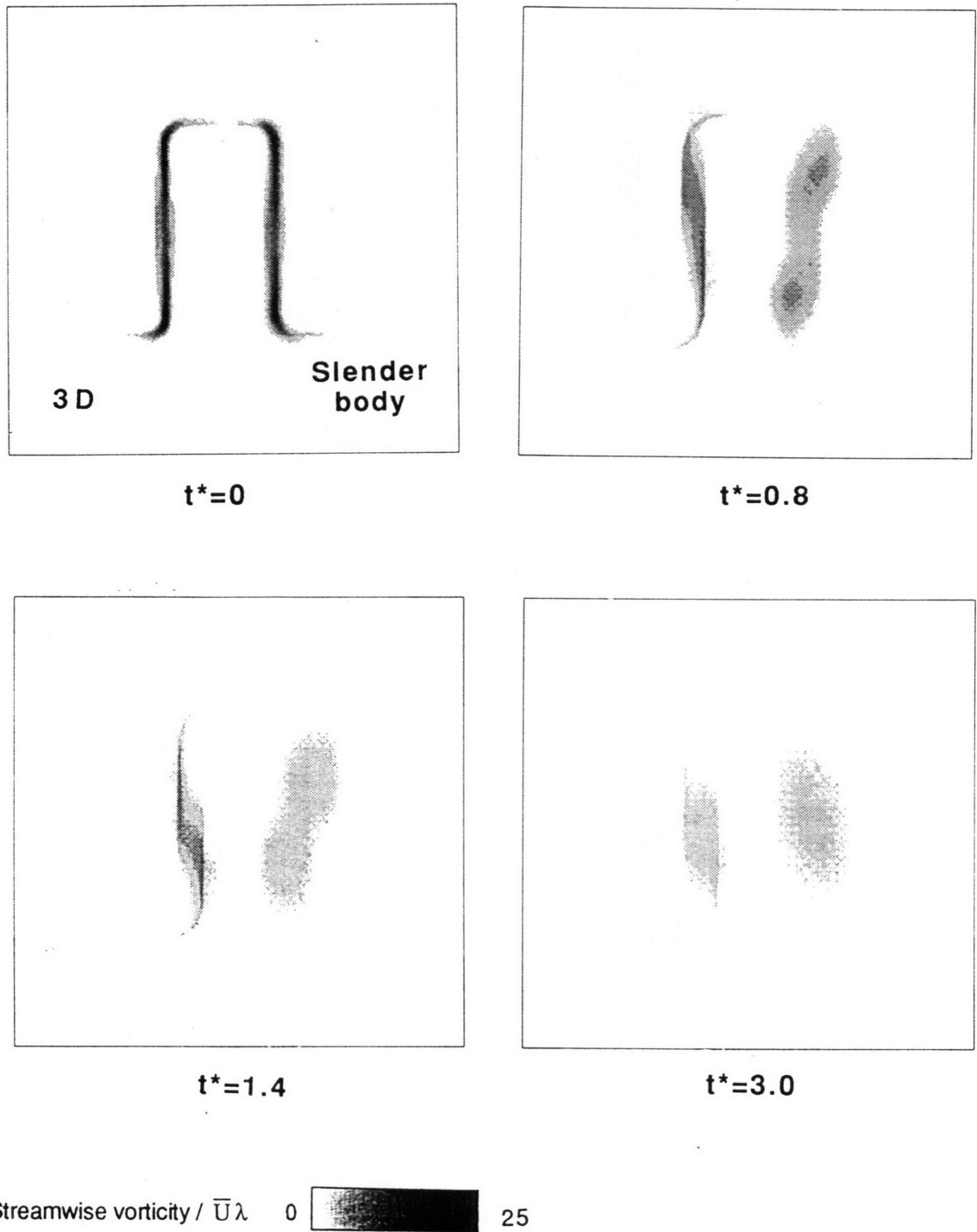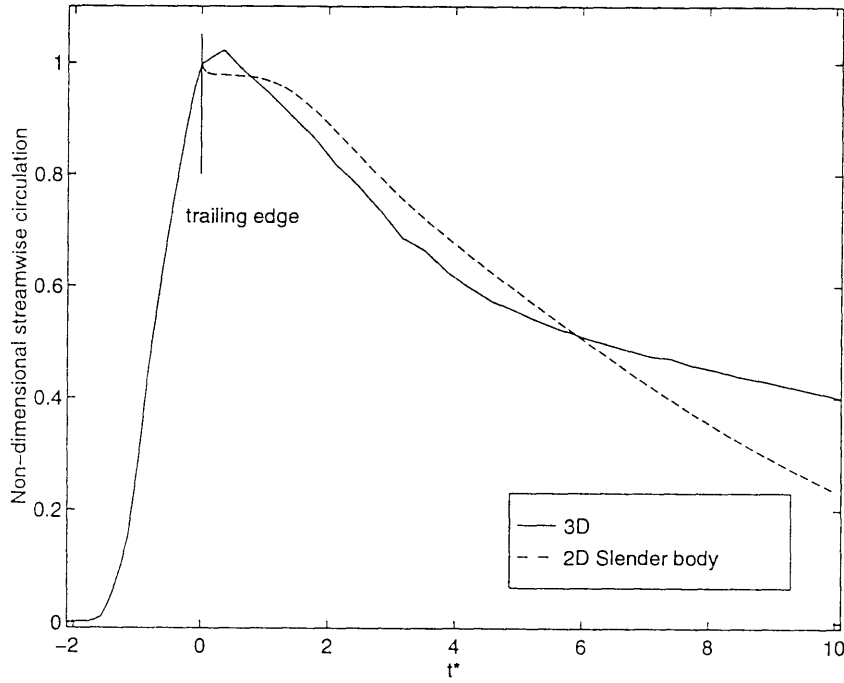**Figure 5-13   Comparison of 3D and slender-body interface length (r=0.7, s=1.0)**

3D Slender body

t*=0

t*=0.8

t*=1.4

t*=3.0

Passive scalar   -1 [____] +1

Figure 5-14   Comparison of 3D and slender body passive scalar distribution at t*= 0, 0.8, 1.4, 3.0 (r=0.7, s=1.0)

3 D

Slender body

t*=0

t*=0.8

t*=1.4

t*=3.0

Streamwise vorticity / $\overline{U}\lambda$ 0 ▮▮▮▮ 25

Figure 5-15   Comparison of 3D and slender body streamwise vorticity distribution at t*= 0, 0.8, 1.4, 3.0 (r=0.7, s=1.0)

114

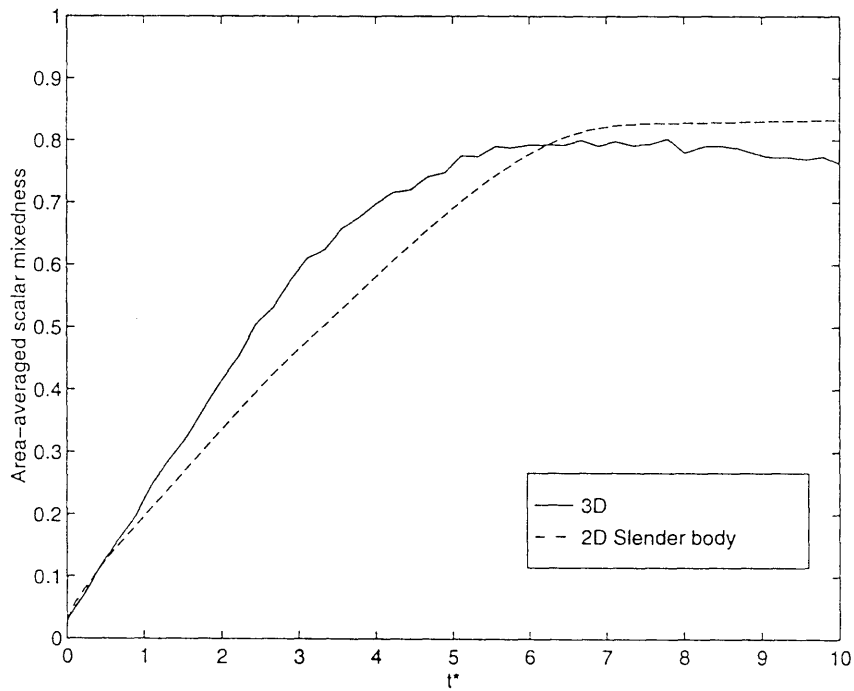**Figure 5-16**   Comparison of 3D and slender-body streamwise circulation decay (r=0.6, s=1.0)

Figure 5-17   Comparison of 3D and slender-body area-averaged scalar mixedness (r=0.6, s=1.0)
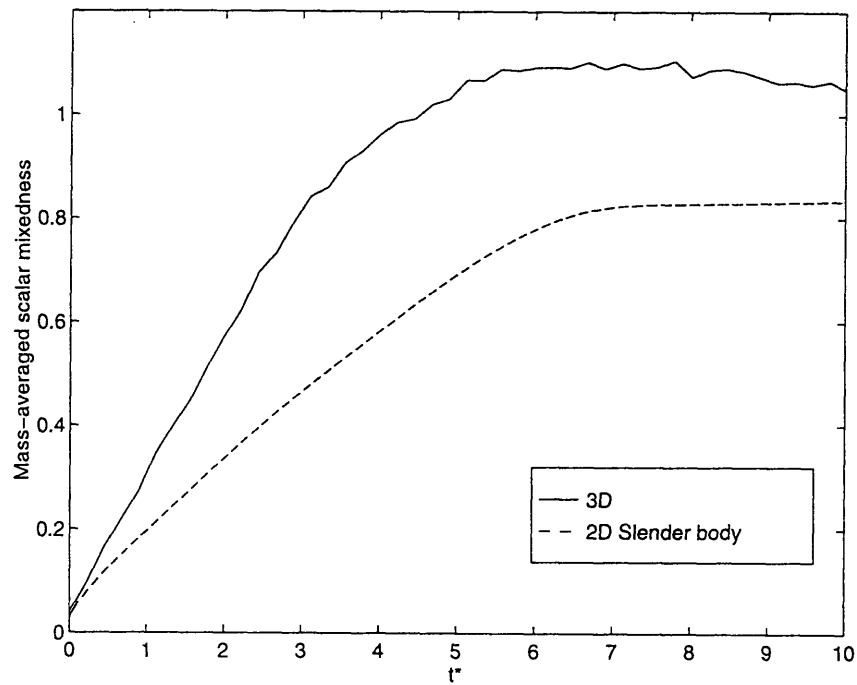
115

Figure 5-18 Comparison of 3D and slender-body mass-averaged scalar mixedness (r=0.6, s=1.0)
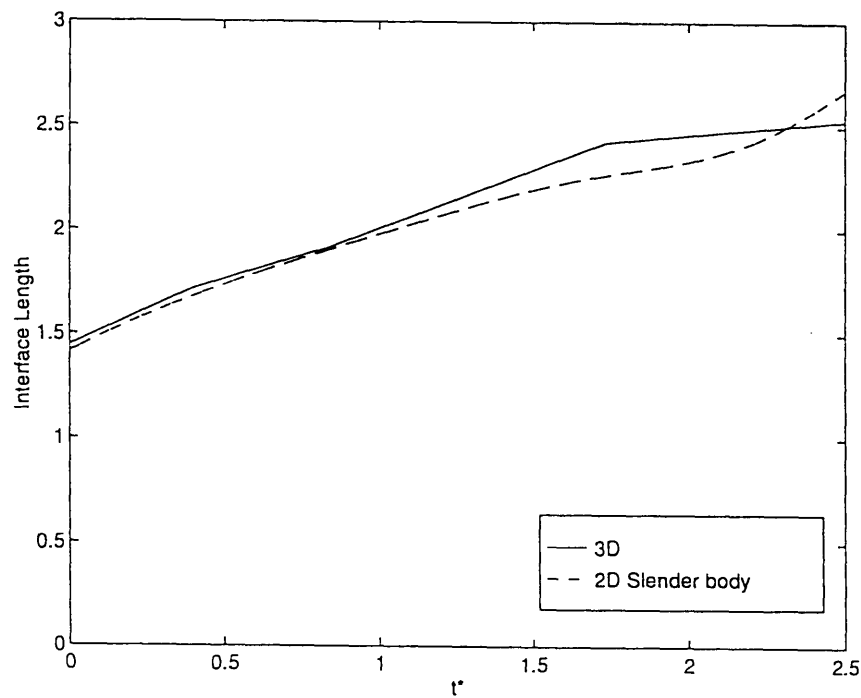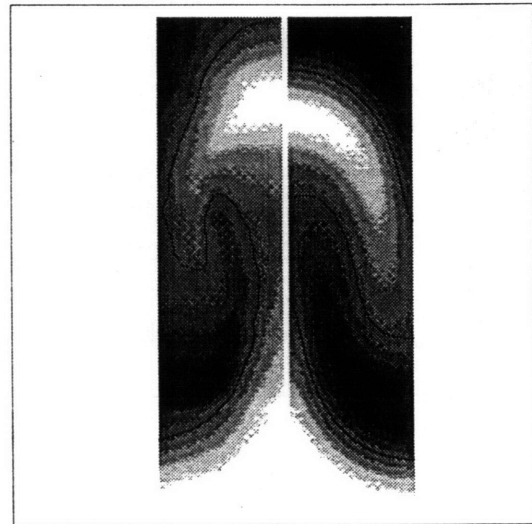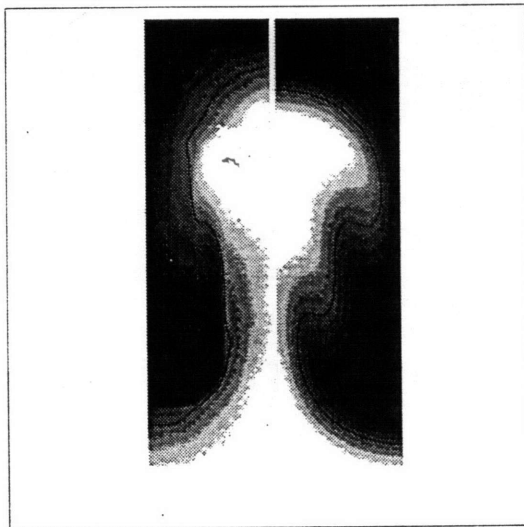

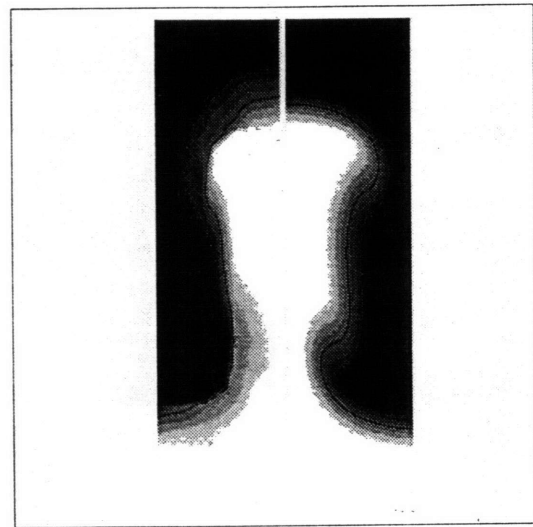
Figure 5-19 Comparison of 3D and slender-body interface length (r=0.6, s=1.0)

116

3 D   **Slender body**

t*=0

t*=0.8

t*=1.4

t*=3.0
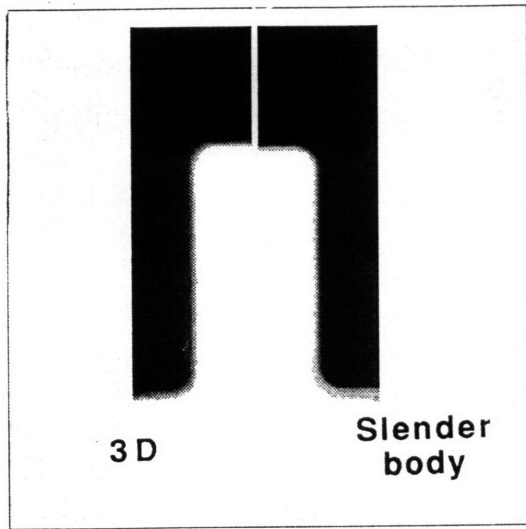
Passive scalar   -1 [ ] +1

Figure 5-20   **Comparison of 3D and slender body passive scalar distribution at t*= 0, 0.8, 1.4, 3.0 (r=0.6, s=1.0)**

3 D Slender body

t*=0

t*=0.8

t*=1.4

t*=3.0
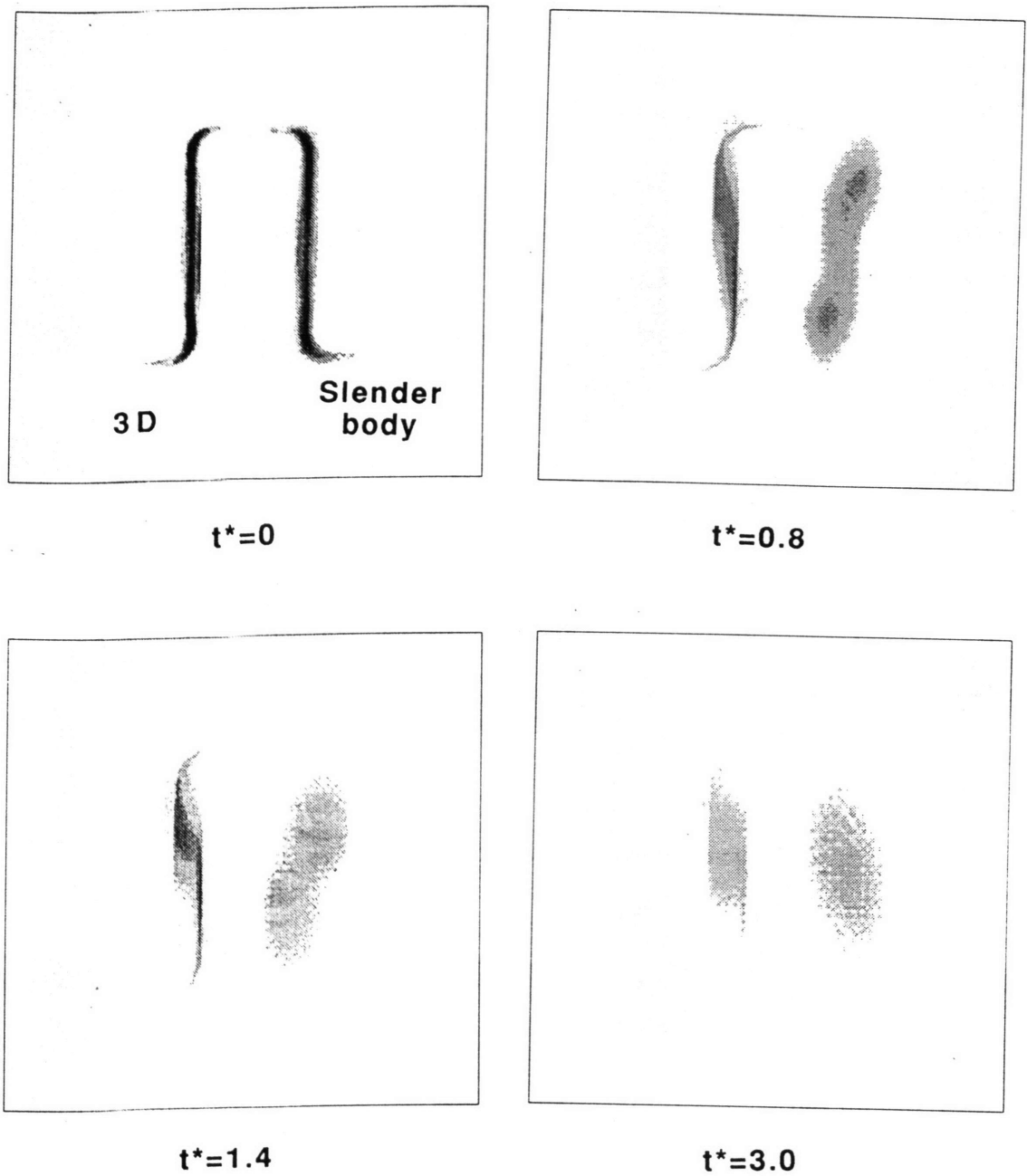
Streamwise vorticity / $\overline{U}\lambda$ 0 [   ] 25

Figure 5-21   Comparison of 3D and slender body streamwise vorticity distribution at t*=0, 0.8, 1.4, 3.0 (r=0.6, s=1.0)

118
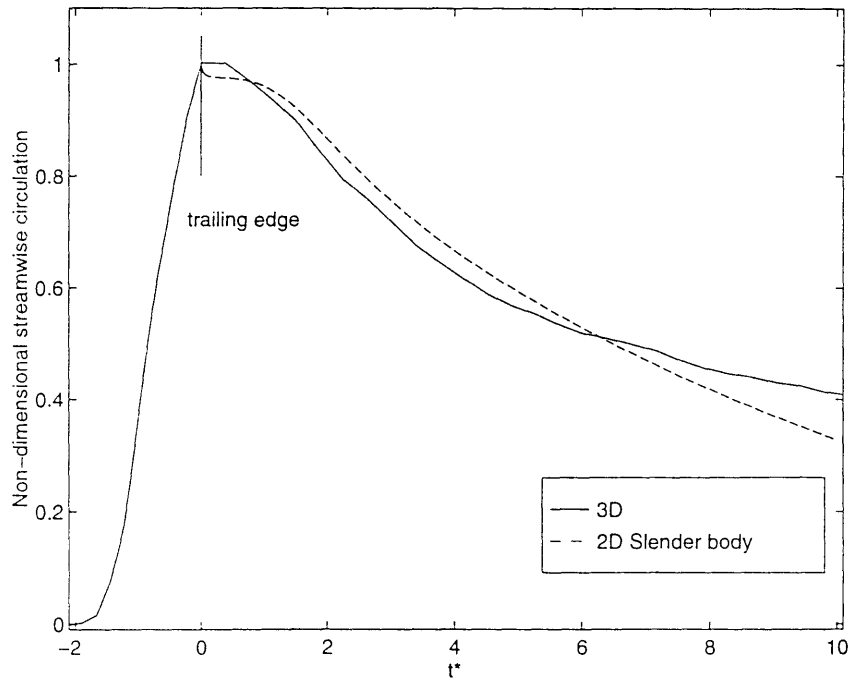
Figure 5-22   Comparison of 3D and slender-body streamwise circulation decay   (r=1.0, s=0.5)
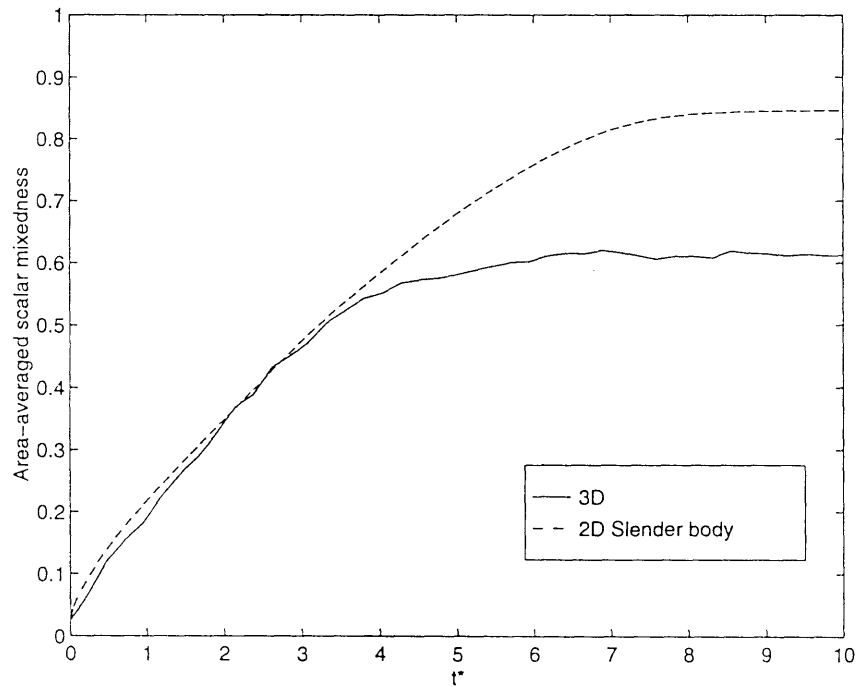
Figure 5-23   Comparison of 3D and slender-body area-averaged scalar mixedness   (r=1.0, s=0.5)

119
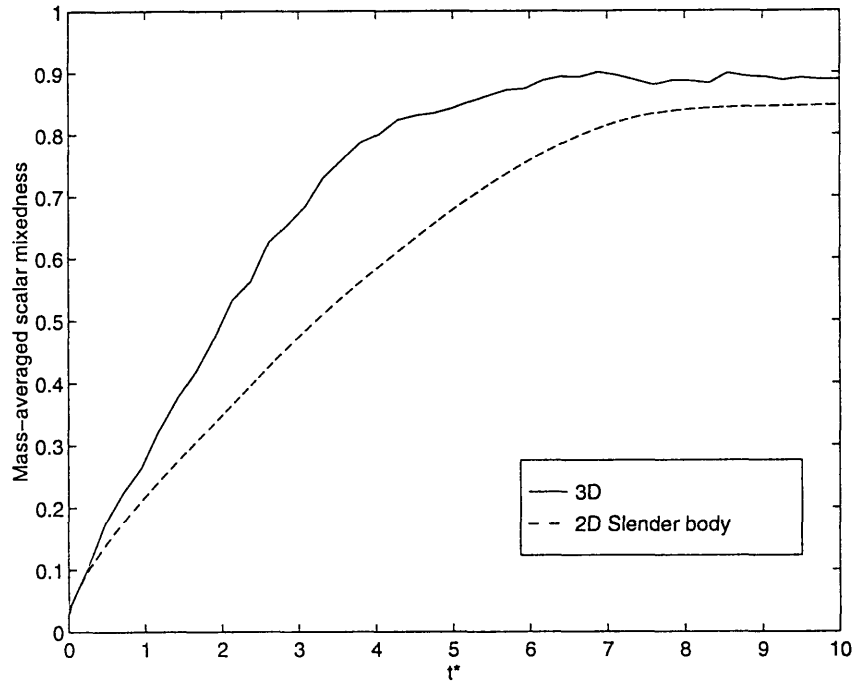
Figure 5-24   **Comparison of 3D and slender-body mass-averaged scalar mixedness (r=1.0, s=0.5)**
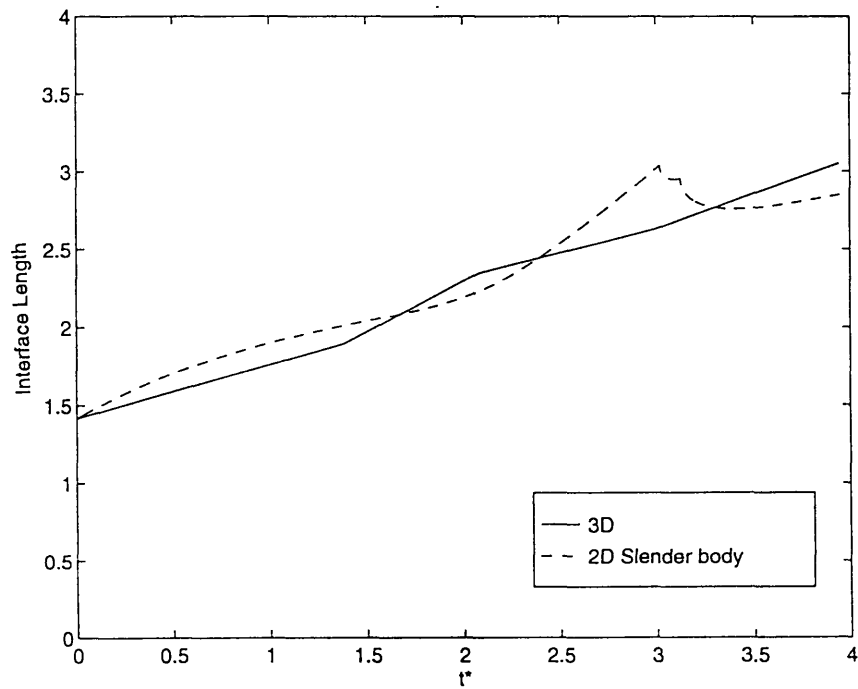
Figure 5-25   **Comparison of 3D and slender-body interface length (r=1.0, s=0.5)**
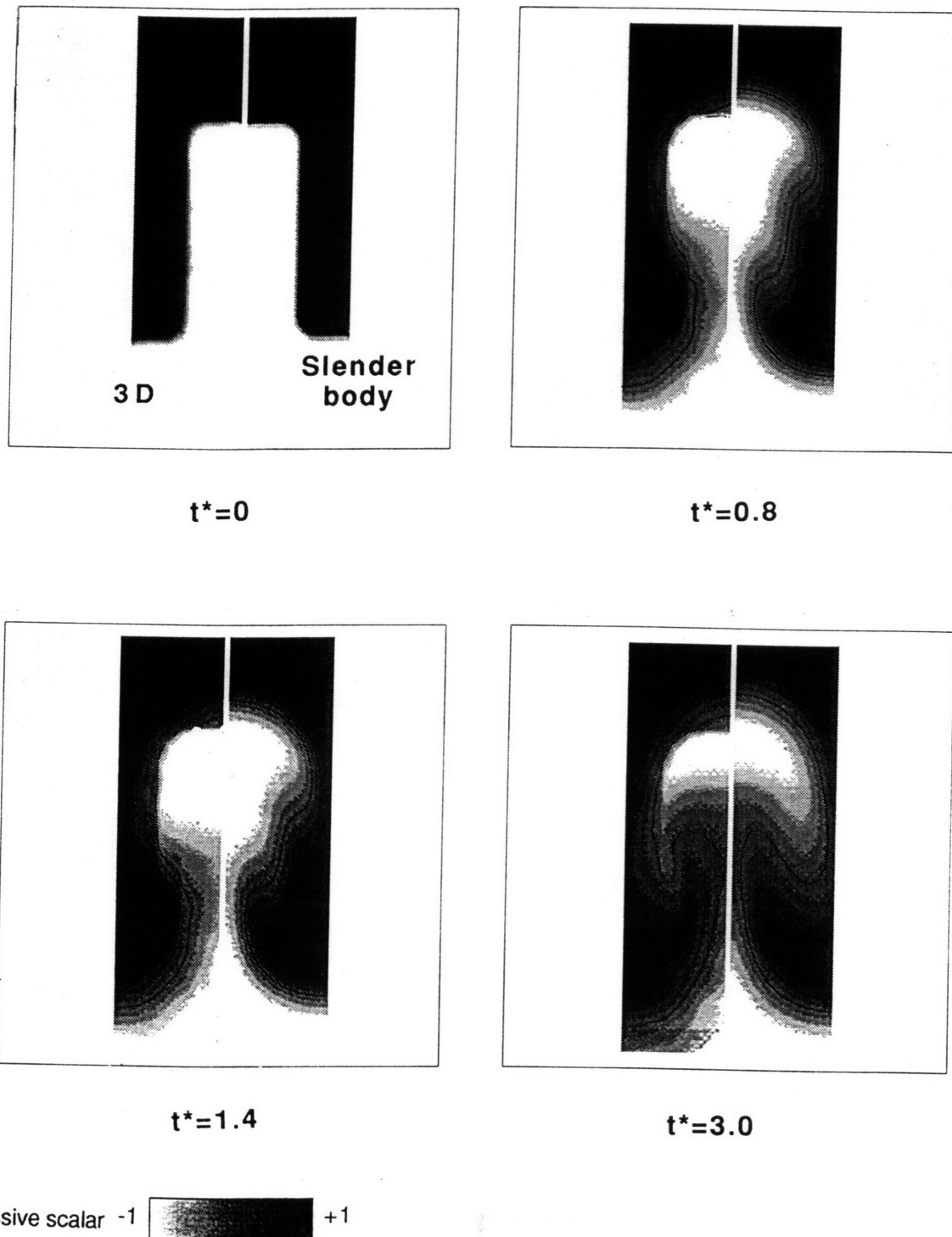
Figure 5-26   Comparison of 3D and slender body passive scalar distribution at t*= 0, 0.8, 1.4, 3.0   (r=1.0, s=0.5)

3 D   Slender body

t*=0   t*=0.8

t*=1.4   t*=3.0
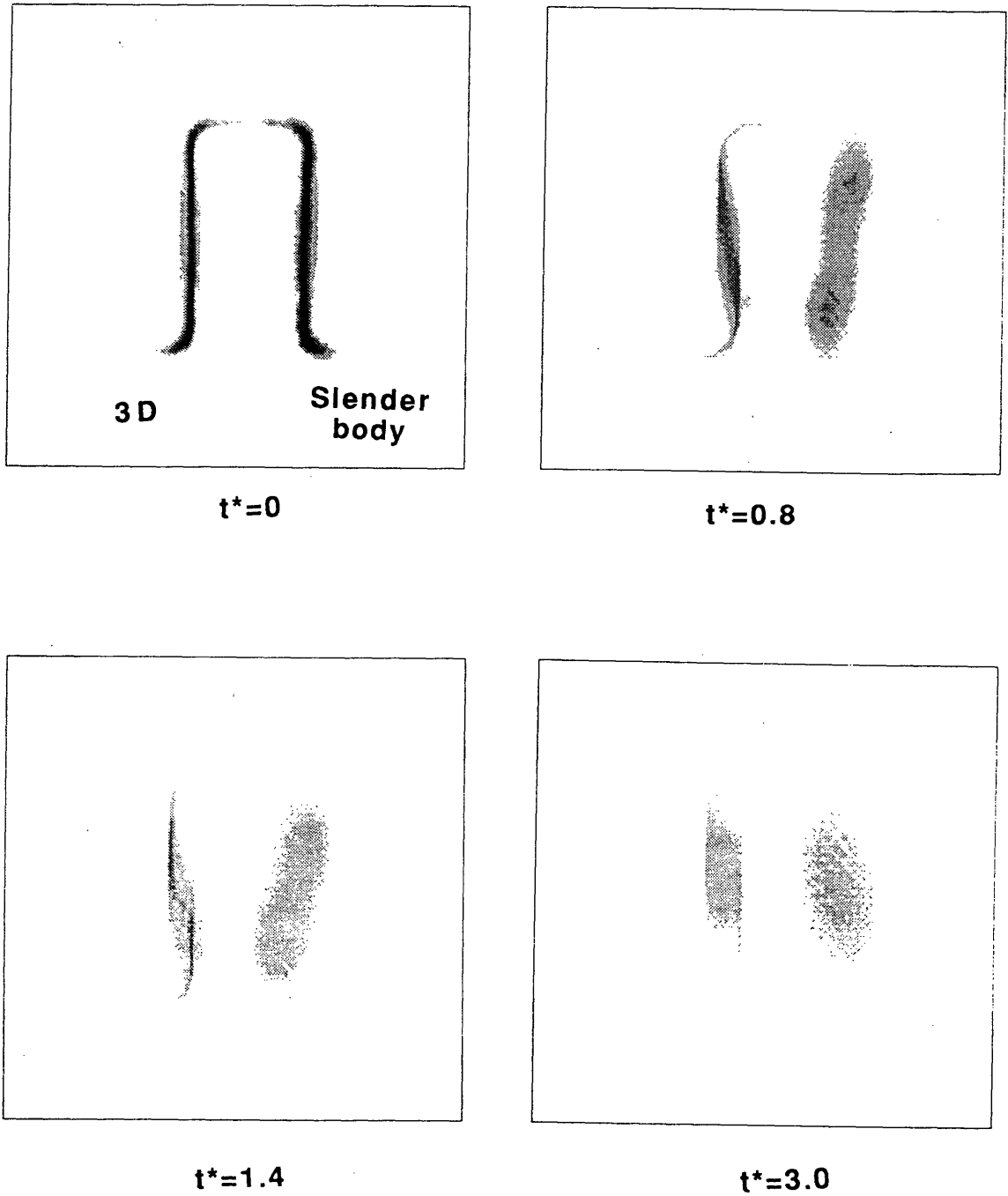
Streamwise vorticity / $\overline{U}\lambda$ 0 [   ] 25

Figure 5-27   **Comparison of 3D and slender body streamwise vorticity distribution at t*= 0, 0.8, 1.4, 3.0 (r=1.0, s=0.5)**
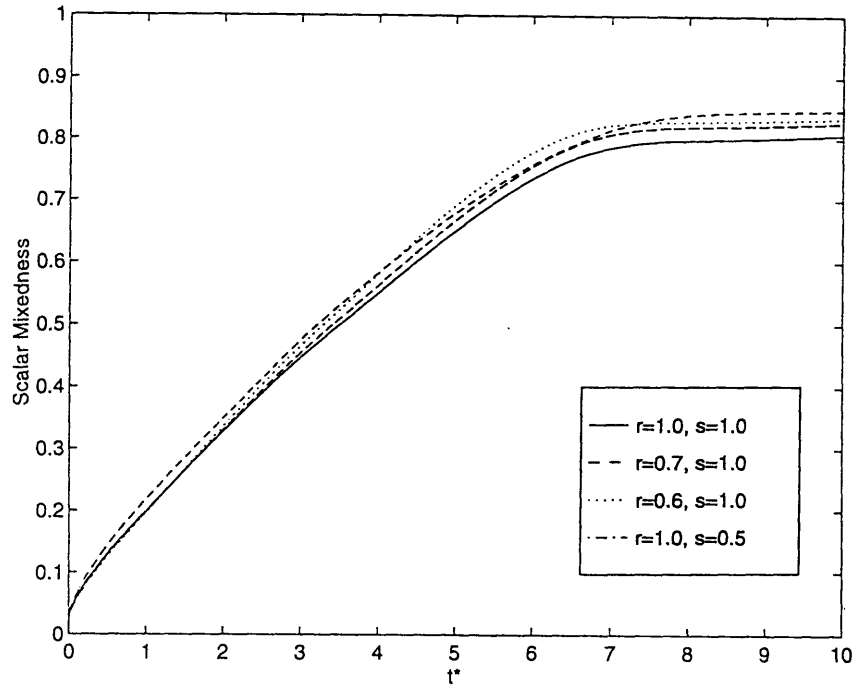
Figure 5-28 Scalar mixednesses for the slender-body solutions (r=1.0, r=0.7, r=0.6, s=0.5)
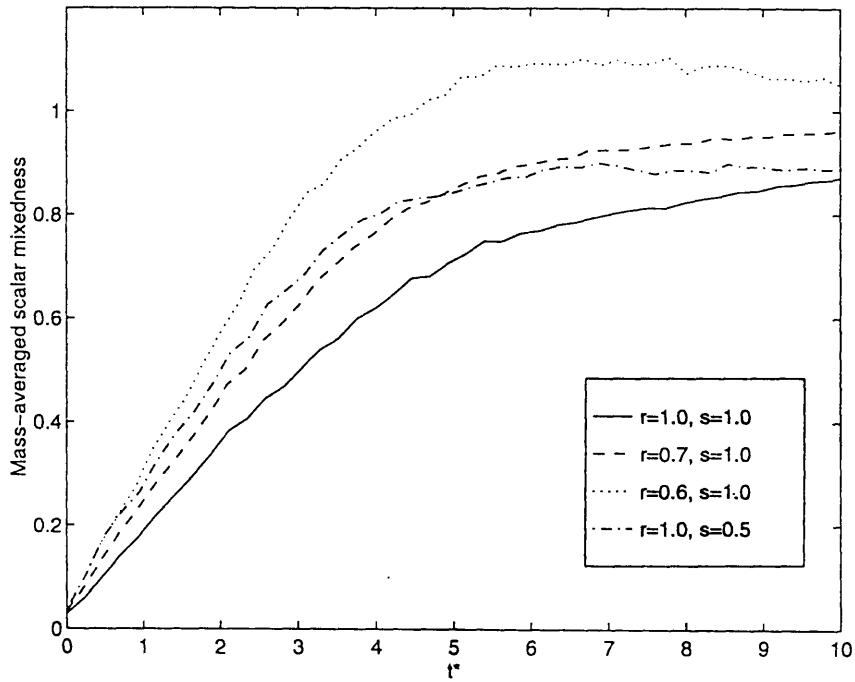
Figure 5-29 Normalized mass-averaged scalar mixednesses for the three-dimensional solutions (r=1.0, r=0.7, r=0.6, s=0.5)

Chapter 6

Conclusions and Recommendations

6.1 Conclusions

The suitability of using a three-dimensional, steady, compressible, unstructured-mesh, viscous, Navier-Stokes solver and a two-dimensional, unsteady, slender-body approximation for investigating lobed mixer flow fields was studied. The three-dimensional Navier-Stokes solver was evaluated for its ability to calculate the shed streamwise circulation, its subsequent downstream evolution and the thrust. The effects of the type of grid generation, boundary layer grid density, turbulence model and smoothing scheme were examined.

The three-dimensional Navier-Stokes solver was used to study the viscous effects in lobed mixers. The effect of varying the penetration angle, inlet boundary layer displacement thickness and velocity ratio on the shed streamwise circulation and total pressure losses was investigated.

The results of the slender-body approximation were compared to a three-dimensional solution to determine the former's range of applicability.

For the Navier-Stokes solver, the following was concluded:

1) Structured-based meshes for lobed mixer geometries had severely skewed elements that resulted in spurious vorticity in the flow domain. This can be overcome in good measure by using fully unstructured grids.

2) Approximately 6 boundary layer elements were required to capture the boundary layer over the lobes for attached flows; more elements were necessary if separation occurred.

3) Replacing the standard k-ε turbulence model in the Navier-Stokes solver with a planar shear-layer model had no discernible impact on the parameters of interest. This suggests that the pressure gradients in lobed mixer flows do not affect the turbulent diffusivity.

4) The viscous Navier-Stokes solver was best suited for examining the flow over the lobes. Downstream of the trailing edge, the values of circulation decay were not within 100% of the (sparse) existing data. A sensitivity analysis showed that in spite of this discrepancy, the scalar mixedness could still be evaluated to within 20%.

From the investigation into the viscous effects in lobed mixers the following was concluded:

5) As the lobe penetration angle was increased from 22° to 45°, the trailing edge circulation deviated from a simple one-dimensional model [29] because of increased boundary layer blockage and separation. Extension of this model using an effective penetration angle and height gave predictions of the shed streamwise circulation that corresponded to the computed ones to within 5%.

6) For the type of mixers examined, there was no benefit, in terms of the trailing streamwise circulation, of increasing the penetration angle above 30° because of increased boundary layer blockage and separation.

7) The losses associated with the lobed mixer increased with the penetration angle. For typical stream to stream velocity ratios mixing losses dominate.

The comparisons of the slender-body approximation to the three-dimensional solutions resulted in the following conclusions:

8) The slender-body approximation was found to be valid for a less restrictive range of conditions than would be suggested by only dimensional analysis. Slender-body theory held for flows with non-dimensional shed streamwise circulations of up to ≈ 1 and $\Delta U / \overline{U} \leq 0.3$. It was marginal for a stream-to-stream density ratio of 0.5.

9) The interface lengths matched closely between the two solutions for all the velocity ratios down to 0.6 and density ratios to 0.5.

6.2 Recommendations for Future Work

To further ensure and extend the validity of the Navier-Stokes solver, NEWT, the following studies should be performed:

1) A simulation of the baseline case ($\alpha=22°$, r=0.6) should be performed utilizing another three-dimensional viscous Navier-Stokes solver and then compared to the solution of NEWT. This will ascertain which limitations are specific to NEWT (and how they may be addressed), and which are general failings of this type of computation.

2) The current fully unstructured grids were optimized for the flow over the lobes at the expense of the downstream region. The current grid generator can be used to optimize the grids further by expanding the boundary layer region faster, improving the local refinement and reducing the change in aspect ratio between adjacent elements.

3) An adaptive-meshing routine should be implemented. This can be accomplished by either modifying the routine included in NEWT for fully unstructured grids or

incorporating the one from the FELISA unstructured-mesh system into NEWT. In this way grids with sparse boundary layers can be generated, thereby avoiding skewed elements and large changes in their size. The grids can then be adaptively refined to accurately resolve the boundary layer over the lobes and the swirling flow downstream of the trailing edge.

4) A multi-block grid generator may be tested in order to overcome competing requirements of the grid over the lobes and downstream of the trailing edge. There is also the future potential of new fully automatic viscous grid generators [25].

5) A full wavelength of a lobed mixer should be simulated in order to ascertain the accuracy of the inviscid wall boundary conditions, particularly with respect to the calculation of the streamwise circulation.

6) In order to employ NEWT for mixed supersonic/subsonic inlets flows for lobed mixer geometries, the true Laplacian smoother should be tested. Also, the method of characteristics may be incorporated into NEWT to properly specify the outflow boundary conditions.

In order to fully understand the limits of the slender-body approximation, the following should be investigated:

7) The slender-body - three-dimensional comparisons should be performed for stream-to-stream density ratios between 0.5 and 1.0 to determine the limiting case. Also, cases with non-dimensional shed circulations greater than one should be examined to find the upper limit of this parameter.

8) The terms neglected in the slender-body approximation should be examined using the three-dimensional solutions in order to determine why the approximation is valid past the analytically derived limits.

Bibliography

[1] Browand, F. K., Latigo, B. O., "Growth of the Two-Dimensional Mixing Layer From a Turbulent and Nonturbulent Boundary Layer". *Phys. Fluids*, Vol. 22, No. 6, June 1979.

[2] Cumpsty, N. A., Compressor Aerodynamics, Longman Group, 1989.

[3] Dawes, W. N., "The Development of a Solution-Adaptive 3-D Navier-Stokes Solver for Turbomachinery". AIAA-91-2469.

[4] Dawes, W. N., "The Practical Application of Solution-Adaptation to the Numerical Simulation of Complex Turbomachinery Problems". *Prog. in Aerospace Sci.*, Vol. 29, 1992, pp. 221-269.

[5] Dawes, W. N., "The Simulation of Three-dimensional Viscous Flow in Turbomachinery Geometries Using a Solution-Adaptive Unstructured Mesh Methodology", *J. of Turbomachinery*, ASME 91-GT-124, Orlando FL, 1991.

[6] Dawes, W. N. Personal communication. 1995.

[7] Dawes, W. N. Personal communication. 1994.

[8] Dimotakis, P., "Turbulent Free Shear Layer Mixing". AIAA-89-0262, 1989.

[9] Dimotakis, P., "Two-Dimensional Shear-Layer Entrainment". AIAA-84-0368, 1986.

[10] Elliot, J. K., "A Computational Investigation of the Fluid Dynamics of a Three-Dimensional, Compressible, Mixing Layer with Strong Streamwise Vorticity". S.M. Thesis, Massachusetts Institute of Technology, Cambridge MA, 1990.

[11] Fung, A. K. S., "Modeling of Mixer-Ejector Nozzle Flows", S.M. Thesis, Massachusetts Institute of Technology, Cambridge MA, 1995.

[12] Koutmos, P., McGuirk, J. J., Priddin, C. H., Sodha, M. N., "Numerical Investigation of the Flow Within a Turbofan Lobed Mixer". *Journal of Propulsion*, Vol. 7, No. 3 May-June 1981, pp. 389-394.

[13] Koutmos, P., McGuirk, J. J., "Turbofan Forced Mixer/Nozzle Temperature and Flow Field Modeling". *Int. J. Heat Mass Transfer*, Vol. 32, No. 6, 1989, pp. 1141-1159.

[14] Lam, C. K. G., Bremhorst, K. A., "Modified Form of the k-ε Model for Predicting Wall Turbulence". *Journal of Fluids Engineering*, Vol. 103, 1981.

[15] Little, D. R., "Fuel-Efficient-5C Long Duct Mixed Flow Nacelle". *The Leading Edge*, GE Aircraft Engines, Cincinnati Ohio, Spring 1993.

[16] Lord, W. K., Jones, C. W., Stern, A.M., Head, V. L., Krejsa, E. A., "Mixer Ejector Nozzle for Jet Noise Suppression". AIAA 90-1909, AIAA/SAE/ASME/ASEE 26th Joint Propulsion Conference, Orlando FL, July 16-18 1990.

[17] Manning T. A., "Experimental Study of Mixing Flows with Streamwise Vorticity". S.M. Thesis, Massachusetts Institute of Technology, Cambridge MA, 1991.

[18] McCormick, D. C., "Vortical and Turbulent Structure of Planar and Lobed Mixer Free Shear Layers". Ph.D. Thesis, U. of Connecticut, 1992.

[19] Murman, E. M., Becker, T. M., Darmofal, D., "Computation and Visualization of Leading Edge Vortex Flows". *Computing Systems in Engineering* Vol.1, Nos. 2-4, 1990, pp.341-348.

[20] O' Sullivan, M. N., "A Computational Study of the Effects of Viscosity on Lobed Mixer Flowfields", S.M. Thesis, Massachusetts Institute of Technology, Cambridge MA, 1993.

[21] Papamoschou, D., Roshko, A., "The Compressible Turbulent Shear layer: An Experimental Study". *J. Fluid Mech.*, Vol. 197, pp. 452-477, 1988.

[22] Patel, V. C., Rodi, W., Scheuerer, G., "Turbulence Models for Near-wall Flows and Low Reynolds Numbers: A Review". *AIAA Journal*, Vol. 23, No. 9, Sept. 1984.

[23] Paterson, R. W., "Turbofan Forced Mixer-Nozzle Internal Flowfield: Volume 1- A Benchmark Experimental Study". *ASME Journal of Engineering for Gas Turbines and Power*, Vol. 106, July 1984, pp. 692-698.

[24] Peiró, J., Peraire, J., Morgan, K., "Felisa System Reference Manual, Part 1 - Basic Theory", December 1993.

[25] Peraire, J. Personal communication. 1994.

[26] Povinelli, L., Anderson, B., Gerstenmaier, W., "Computation of Three Dimensional Flow in Turbofan Mixers and Comparison with Experimental Data". AIAA-80-1088, 1980.

[27] Qiu, Y. J., "A Study of Streamwise Vortex Enhanced Mixing in Lobed Mixer Devices". Ph.D. Thesis, Massachusetts Institute of Technology, Cambridge MA, 1992.

[28] Schetz, Joseph A., Boundary Layer Analysis, Prentice-Hall, 1993.

[29] Skebe, S. A., Paterson, R. W., Barber, T. J., "Experimental Investigation of Three-Dimensional Forced Mixer Lobe Flow Fields". AIAA-88-3785, AIAA/ASME/SIAM/APS 1st Nat. Fluid Dynamics Congress, 1988.

[30] Spencer, B. W., Jones, B. G., "Statistical Investigation of Pressure and Velocity Fields in the Turbulent Two-Stream Mixing Layer". AIAA-71-613, 1971.

[31]   Tillman, T. G., Paterson, R. W., Presz, W. M., "Supersonic Nozzle Mixer Ejector". *Journal of Propulsion and Power*, Vol. 8, No. 2, March-April 1992, pp. 512-519.

[32]   Underwood, D. S., "Effect of Heat Release on Streamwise Vorticity Enhanced Mixing". S.M. Thesis, Massachusetts Institute of Technology, Cambridge MA, 1995.

[33]   Waitz, I. A. Personal communication. 1995.

[34]   Waitz, I. A., Elliot, J. K., Fung, A. K. S., Kerwin, J. M., Krasnodebski, J. K., O'Sullivan, M. N., Qiu, Y. J., Tew, D. E., Greitzer, E. M., Marble, F. E., Tan,. C. S., and Tillman, T. G. "Streamwise-Vorticity-Enhanced Mixing". manuscript in preparation. 1995.

[35]   White, F. M., Viscous Fluid Flow, 2nd Ed., McGraw-Hill, 1991.

[36]   White, F. M., Fluid Mechanics, 2nd Ed., McGraw-Hill, 1986.